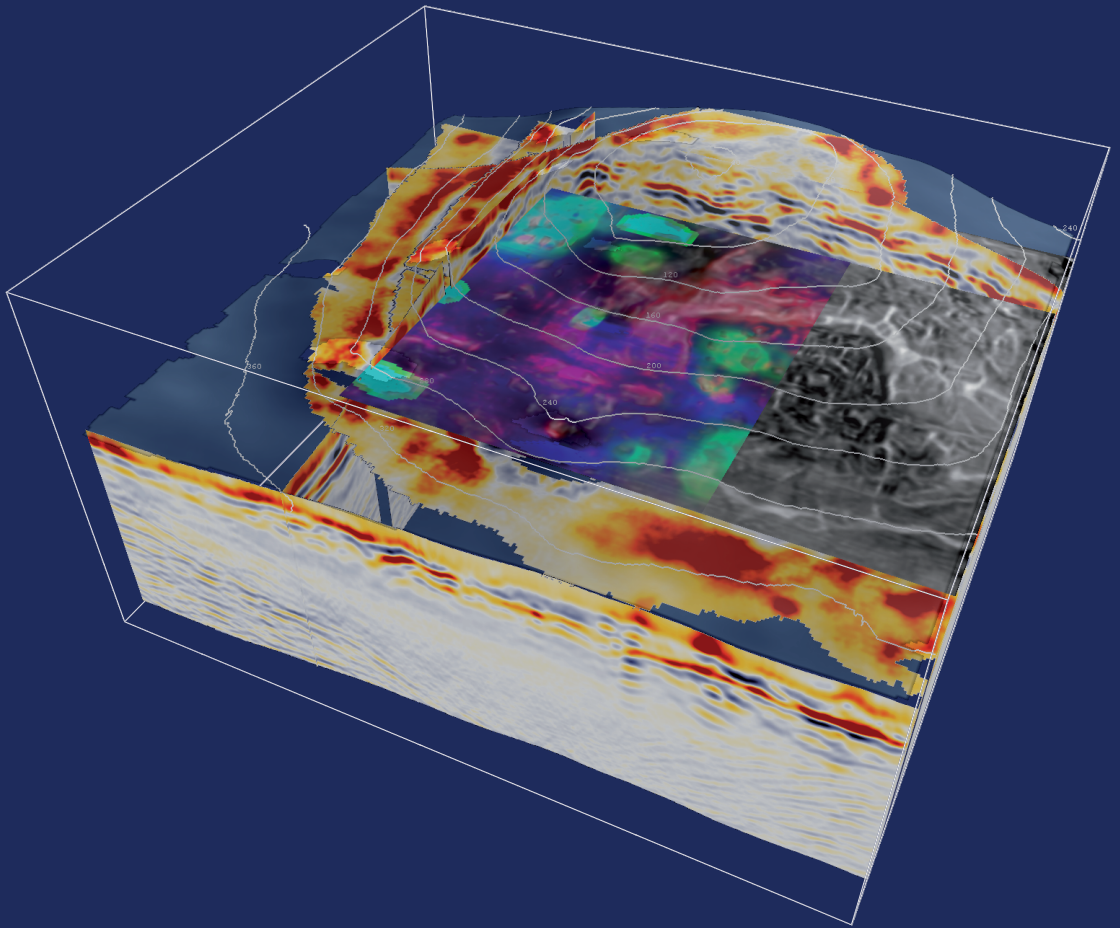


# Attributes and their potential to analyze and interpret 3D GPR data





# ATTRIBUTES AND THEIR POTENTIAL TO ANALYZE AND INTERPRET 3D GPR DATA

Dissertation  
zur Erlangung des akademischen Grades  
“doctor rerum naturalium”  
(Dr. rer. nat.)  
in der Wissenschaftsdisziplin “Geophysik”

eingereicht an der  
Mathematisch-Naturwissenschaftlichen Fakultät  
**UNIVERSITÄT POTSDAM**



von  
**Dipl. Natw. ETH Urs Böniger**

Berlin den 06.07.2010

Published online at the  
Institutional Repository of the University of Potsdam:  
URL <http://opus.kobv.de/ubp/volltexte/2011/5012/>  
URN <urn:nbn:de:kobv:517-opus-50124>  
<http://nbn-resolving.org/urn:nbn:de:kobv:517-opus-50124>

# ATTRIBUTES AND THEIR POTENTIAL TO ANALYZE AND INTERPRET 3D GPR DATA

Supervisor: Prof. Dr. Jens Tronicke



# CONTENTS

---

<b>TABLE OF CONTENTS</b>	<b>v</b>
<b>LIST OF FIGURES</b>	<b>ix</b>
<b>PREFACE</b>	<b>xiii</b>
<b>1 INTRODUCTION</b>	<b>1</b>
1.1 Positioning in kinematic GPR surveying . . . . .	2
1.1.1 RTK-GPS based surveying . . . . .	2
1.1.2 TTS based surveying . . . . .	4
1.1.3 Hybrid GPS-TTS based surveying . . . . .	5
1.1.4 RLPS based surveying . . . . .	6
1.2 Attribute based data analysis . . . . .	7
1.3 Objectives and outline of this thesis . . . . .	12
<b>2 KINEMATIC ACQUISITION USING A SELF-TRACKING TOTAL STATION</b>	<b>15</b>
2.1 Abstract . . . . .	15
2.2 Introduction . . . . .	16
2.3 TTS Based GPR Surveying . . . . .	18
2.4 Influence of cross-talk on data quality . . . . .	19
2.5 Latency Estimation and Correction . . . . .	22
2.6 Conclusions . . . . .	28
2.7 Acknowledgments . . . . .	28

<b>3</b>	<b>TARGET-SPECIFIC ATTRIBUTE ANALYSIS APPLIED TO TOMB DETECTION</b>	<b>29</b>
3.1	Abstract . . . . .	29
3.2	Introduction . . . . .	30
3.3	Data Acquisition and Standard Processing . . . . .	32
3.4	Attribute Analysis . . . . .	33
3.4.1	Energy . . . . .	33
3.4.2	Coherency . . . . .	34
3.4.3	Similarity . . . . .	35
3.5	Field Sites . . . . .	36
3.5.1	Survey site I: Old Chapel Golm . . . . .	36
3.5.2	Survey Site II: Chapel Bishops Residence Ziesar . . . . .	40
3.6	Conclusions . . . . .	42
3.7	Acknowledgments . . . . .	43
<b>4</b>	<b>INTEGRATED GEOPHYSICAL ANALYSIS AT AN ARCHAEOLOGICAL SITE</b>	<b>45</b>
4.1	Abstract . . . . .	45
4.2	Introduction . . . . .	46
4.3	Field Site . . . . .	47
4.4	Data Acquisition and Processing . . . . .	49
4.4.1	Acquisition . . . . .	49
4.4.2	Standard Processing . . . . .	50
4.4.3	Attribute Analysis . . . . .	53
4.4.4	Composite Imaging . . . . .	55
4.5	Results . . . . .	57
4.6	Interpretation . . . . .	58
4.7	Conclusions . . . . .	60
4.8	Acknowledgments . . . . .	60
<b>5</b>	<b>DUAL-COMPONENT ATTRIBUTE BASED DATA ANALYSIS</b>	<b>61</b>
5.1	Abstract . . . . .	61
5.2	Introduction . . . . .	62
5.3	Background . . . . .	63
5.3.1	Survey Site . . . . .	63
5.3.2	Data Acquisition and Standard Processing . . . . .	64



---

5.4	Geometrical Extraction using Phase Symmetry . . . . .	67
5.4.1	Phase Symmetry . . . . .	68
5.4.2	Synthetic Examples . . . . .	69
5.4.3	Application to Field Data . . . . .	71
5.5	PCA Derived Polarization Attributes . . . . .	72
5.5.1	Synthetic Studies . . . . .	73
5.5.2	Application to Field Data . . . . .	75
5.6	Depolarization Analysis . . . . .	76
5.7	Conclusions . . . . .	78
5.8	Acknowledgments . . . . .	79
<b>6</b>	<b>GPR DATA ANALYSIS USING EXTENDED TREE-BASED PURSUIT</b>	<b>81</b>
6.1	Abstract . . . . .	81
6.2	Introduction . . . . .	82
6.3	Spectral decomposition methods . . . . .	82
6.4	Modified tree-based pursuit . . . . .	83
6.5	Synthetic example . . . . .	85
6.6	Field example I: Thin-bed responses . . . . .	88
6.7	Field example II: Enhancing the resolution by atomic frequency modulation . . . . .	89
6.8	Conclusions . . . . .	93
6.9	Acknowledgments . . . . .	94
<b>7</b>	<b>GENERAL CONCLUSIONS AND PERSPECTIVES</b>	<b>95</b>
	<b>REFERENCES</b>	<b>99</b>
	<b>SUMMARY</b>	<b>109</b>
	<b>ALLGEMEINVERSTÄNDLICHE ZUSAMMENFASSUNG</b>	<b>113</b>
	<b>CURRICULUM VITAE</b>	<b>115</b>



# LIST OF FIGURES

---

1.1	RTK-GPS based surveying setup . . . . .	3
1.2	TTS based surveying setup after Lehmann and Green (1999) . . . . .	4
1.3	Hybrid GPS-TTS based surveying setup after Young and Lord (2002) . . . . .	5
1.4	RLPS based surveying setup after Grasmueck and Viggiano (2007) . . . . .	6
1.5	Overview of seismic attributes and their classification into geometrical, physical, and corporate attributes . . . . .	9
1.6	Example of attribute-based channel detection after Luo et al. (2003) . . . . .	9
1.7	Example of 3D GPR attribute processing applied to fault characterization after Young et al. (1997) . . . . .	11
2.1	Sketch of novel kinematic GPR surveying setup . . . . .	18
2.2	Influence of radio communication on selected GPR trace spectra . . . . .	20
2.3	Influence of radio communication on data quality . . . . .	21
2.4	Implication and correction of data latency . . . . .	23
2.5	Variation of different fidelity measure between between the forward ( $d^f$ ) and reverse ( $d^r$ ) direction for a selected profile pair . . . . .	25
2.6	Determining optimum latency with three different fidelity measures using 200 MHz GPR data . . . . .	26
2.7	Influence of latency correction on 2D GPR data . . . . .	27
2.8	Influence of latency correction on 3D GPR data . . . . .	27
3.1	Geological versus archaeological GPR 2D profile . . . . .	30
3.2	3D GPR surveying setup using 500 MHz antennae . . . . .	32
3.3	Trace neighborhood used for attribute calculation . . . . .	34
3.4	Survey site I: Medieval chapel of Golm, Germany . . . . .	37
3.5	Exemplary time slices from survey site I . . . . .	37
3.6	Comparison of a selected time slice from survey site I using dipmedian filtered data, energy, coherency, and similarity . . . . .	38

3.7	Detailed interpretation based on the similarity data cube . . . . .	39
3.8	Survey site II: Chapel of the medieval bishops residence Ziesar, Germany . . . . .	40
3.9	Exemplary time slices from survey site II . . . . .	41
3.10	Comparison of a selected time slice from survey site II using dip-median filtered data, energy, coherency, and similarity . . . . .	42
4.1	Overview sketch of the study site in the Palace Garden of Paretz, Germany . . . . .	48
4.2	Sketch of the used kinematic acquisition setup . . . . .	49
4.3	DTM acquired kinematically during magnetic data collection . . . . .	51
4.4	Gridded magnetic gradient map . . . . .	51
4.5	Typical inline, crossline, and time slice through our migrated GPR data cube . . . . .	52
4.6	Topographic attributes derived from the DTM shown in Figure 4.3 . . . . .	53
4.7	Attributes derived from the magnetic data set illustrated in Figure 4.4 as vertical gradient. . . . .	54
4.8	GPR attributes derived from the migrated data cube illustrated in Figure 4.5 . . . . .	55
4.9	Examples of composite images . . . . .	56
4.10	Interpretation of composite images . . . . .	59
5.1	Unmigrated and migrated time slices through the 3D GPR data cubes . . . . .	65
5.2	Geometry of the two radial GPR surveys consisting of 18 rotated 200 MHz GPR profiles centered across two subsurface pipes . . . . .	66
5.3	Gridded radial profiles from survey A (Figure 5.2) acquired at angles of 0°– 170° relative to the pipe orientation . . . . .	66
5.4	Gridded radial profiles from survey B (Figure 5.2) acquired at angles of 0°– 170° relative to the pipe orientation . . . . .	67
5.5	Suggested feature extraction approach . . . . .	70
5.6	Evaluation of the influence of the $X_u$ -to- $X_g$ ratio on the performance of phase symmetry based feature extraction . . . . .	71
5.7	Fused $X_{11}$ and $X_{22}$ data time slice, corresponding phase symmetry $\mathcal{S}_{dc}$ , and feature angle $\phi_f$ slices calculated using Equation 5.4 and 5.5, respectively . . . . .	72
5.8	Four potential scenarios to illustrate the proposed attributes $\phi_p$ and $\mathcal{R}$ . . . . .	74
5.9	Influence of waveform amplitude variations and phase-shifts on the proposed attributes . . . . .	74

---

5.10	$\phi_p$ and $\mathcal{R}$ calculated over a time window length of 12 ns using the unmigrated data cubes . . . . .	75
5.11	Final interpretation of the 3D GPR field data . . . . .	77
6.1	Decomposition results of a synthetic GPR trace composed of amplitude, frequency, and phase modified Ricker wavelets . . . . .	86
6.2	Influence of phase variation inclusion on the decomposition results . . . . .	86
6.3	Comparison of selected time-frequency representations . . . . .	87
6.4	Real GPR thin-bed tuning example . . . . .	89
6.5	Tree-based Pursuit decomposition of a 200 MHz GPR profile . . . . .	91
6.6	Enhancing the resolution by atomic frequency modulation . . . . .	92



# PREFACE

---

This thesis represents the results of my work in the group of Applied Geophysics at the Institute of Earth and Environmental Sciences, University of Potsdam within the past years. This work was financially supported by the Deutsche Forschungsgemeinschaft (DFG) through the project TR512/1-2 entitled “Möglichkeiten der Attributanalyse beim Georadarverfahren: Detaillierte strukturelle und parameterbezogene Charakterisierung des oberflächennahen Untergrundes durch gezielte Extraktion und Kombination verschiedener Datenattribute aus 2-D und 3-D Georadardaten”. The work presented in this thesis represents the collection of several manuscripts, which have been published, are under review, or in preparation for publication in international peer-reviewed journals. Additionally to the material presented here, my research resulted in numerous expanded abstracts presented at national and international conferences. Also, an extensive software package has been developed to process two- and three-dimensional GPR data. Parts of this package are freely available and the full package is available upon request. Within the course of this work, I made substantial use of the free open-source seismic interpretation software OpendTect. I would therefore like to thank dGB Earth Sciences for making their software suite freely available for academic purposes, allowing me for using their excellent framework for 2D and 3D GPR data processing and visualization. I am also thankful to the whole Madagascar (RSF) community, particularly Sergey Fomel for developing and maintaining such a great processing environment promoting the idea of reproducible research. Significant parts of this thesis have been implemented in a reproducible fashion.

Several people contributed in various ways to the completion of my dissertation and I believe that those people are fully aware of my thankfulness. I would like to express my gratitude towards my supervisor Prof. Dr. Jens Tronicke for his confidence in my work within the broad field of attribute analysis, image and signal processing; to Carsten Riggelsen, who became a good friend that has always been open to a broad range of scientific discussions; to all the colleagues who contributed to a memorable and productive time at the University of Potsdam. I am also very grateful to Marko Dubnitzki for his excellent work on managing the instrument pool and always making

sure that the field equipment was in excellent shape.

Especially, I would like to thank Tina for her endless support also during difficult periods in my scientific career. I am also grateful to my family, especially my mother, for accompanying and encouraging me along my entire educational path.



# INTRODUCTION

---

Ground-penetrating radar (GPR) has become a well-established geophysical method to address near-surface problems in various disciplines; for example, archaeology, hydrogeology, and engineering (e.g., Mellett, 1995; Sternberg and McGill, 1995; Annan and Davis, 1997; Grandjean et al., 2000; Bristow and Jol, 2003; Conyers, 2004; Daniels, 2004; Annan, 2005; Lambot et al., 2008; Jol, 2009). In GPR surveying, excitation and reception of a high frequency (MHz–GHz) electromagnetic wavefield at two spatially separated antennae allows for reflection imaging of the subsurface predominantly based on variations of the dielectric permittivity of the material sampled by the propagating wavefront. Governed by the frequency of the employed antennae pair and the structural and electromagnetic properties of the subsurface, depth of penetration ranges from centimeters (Orlando and Slob, 2009) to hundreds of meters (Moran et al., 2000; Francke and Utsi, 2009). Currently, GPR is regarded as the method providing the highest spatial resolution in near-surface geophysical exploration, especially when used in three-dimensional (3D) surveying mode (Butler, 2005). The ongoing success of two-dimensional (2D) and 3D GPR surveying can be attributed to numerous advances in various related fields. This includes recent advances in kinematic surveying (Czarnowski et al., 1996; Lehmann and Green, 1999; Young and Lord, 2002; Grasmueck and Viggiano, 2007), electromagnetic wavefield modeling (Bergmann et al., 1999; Holliger et al., 2003; Giannopoulos, 2005), and the design and application of novel processing algorithms (Beres et al., 1999; Daniels, 2004; Gross et al., 2004).

Standard processing of 2D and 3D GPR reflection data sets focuses on enhancing and correctly imaging structural features, such as geological layer boundaries or man-made buried objects. However, it has been recognized that GPR data may comprise further information (e.g., regarding subsurface material properties) not extracted by standard processing flows (Sigurdsson and Overgaard, 1998; Neal, 2004). Similar observations have been made regarding reservoir related problems faced by the oil and gas industry using reflection seismic data (Chopra and Marfurt, 2007). Reservoir characterization and its assessment (e.g., the geometry of a salt dome, channel thickness, or material properties of relevant formations) have been significantly improved

by the introduction of so-called seismic attributes, often originating from modern signal and image processing algorithms calculated from the reflection seismic data (Brown, 2004; Chopra and Marfurt, 2007). Consequently, a novel field of research, called attribute analysis, has emerged. Today's success of 2D and 3D seismic interpretation can clearly be associated with the advances in attribute-driven data analysis.

GPR data are often considered as an equivalent to post-stack seismic reflection data (Loughridge, 1998). Thus, GPR data processing and analysis is largely based on techniques adapted from reflection seismics. However, attribute analysis is rarely employed when analyzing and interpreting GPR data. One reason is that many GPR specific targets are not comparable to geological targets faced by reflection seismics and thus, the corresponding processing approaches often do not readily address GPR specific problems. However, to further advance the applicability of the GPR method, there is clearly a need for improved analysis and interpretation approaches, for example, the development of GPR specific attributes.

A pre-requisite for 3D GPR data analysis in general, and for multi-trace attribute processing in particular, is a dense data grid with accurate trace localization. This can only be efficiently achieved by high-precision kinematic surveying. In the following, I review existing real-time kinematic positioning approaches. Then, I briefly introduce the field of attribute-based analyses of reflection seismic and GPR data. At the end of this chapter, I formulate the motivation and objectives of this thesis.

## 1.1 Positioning in kinematic GPR surveying

Within the past decade, it has been recognized that modern surveying solutions such as those based on the global positioning system (GPS), allow for acquiring near-surface geophysical data efficiently. Especially in the context of high-resolution 2D and 3D GPR surveying, different approaches have been suggested in the literature, as presented in the following sections.

### 1.1.1 RTK-GPS based surveying

The GPS consists of a network of orbiting satellites emitting phase modulated signal codes at two carrier frequencies, the so-called L1 (1575.4 MHz) and L2 (1227.6 MHz) bands (Kaplan, 1996). Carrier frequency modulation generates both C/A (coarse acquisition) and P (precision) codes. The spatial localization of a receiver is based on pseudo-range calculation ( $\delta x$ ,  $\delta y$ ,  $\delta z$ ) and a correction for transmitter-receiver clock errors ( $\delta t$ ). Therefore, a minimum of four satellites is required to determine a position; that is, to solve the resulting system of equations for the four unknowns

$\delta x$ ,  $\delta y$ ,  $\delta z$ , and  $\delta t$ . Driven by the removal of the artificially introduced positioning inaccuracy (known as selective availability) by the United States military in 2000, GPS based surveying has emerged as the most commonly applied kinematic surveying solution in near-surface geophysics. Given the required positional accuracy (Grasmueck et al., 2005) of low-to-intermediate-frequency GPR surveying, dual-frequency real-time kinematic (RTK) GPS setups are inevitable (Czarnowski et al., 1996).

Figure 1.1 illustrates the setup of such a dual-frequency RTK-GPS based surveying approach. While RTK setups require line-of-sight to five satellites during initialization in order to resolve ambiguities, once initialized, reception from four satellites is sufficient. As long as the reference station stays connected to the rover, high-precision positioning can be achieved with only a minor influence from the number of satellites used (Lemmon and Gerdan, 1999). Aside from the number of actual satellites connected to a GPS receiver, their geometrical distribution significantly influences the achievable positioning precision (Kaplan, 1996). Similar to differential GPS setups, RTK is based on the assumption of equal signal distortions (such as signal delays introduced by atmospheric water vapor; see Solheim et al. (1999)) across the study site.

Due to the wide-spread application of GPS-based surveying, most modern GPR systems are pre-equipped with serial ports (RS232) allowing for immediate GPS data in-

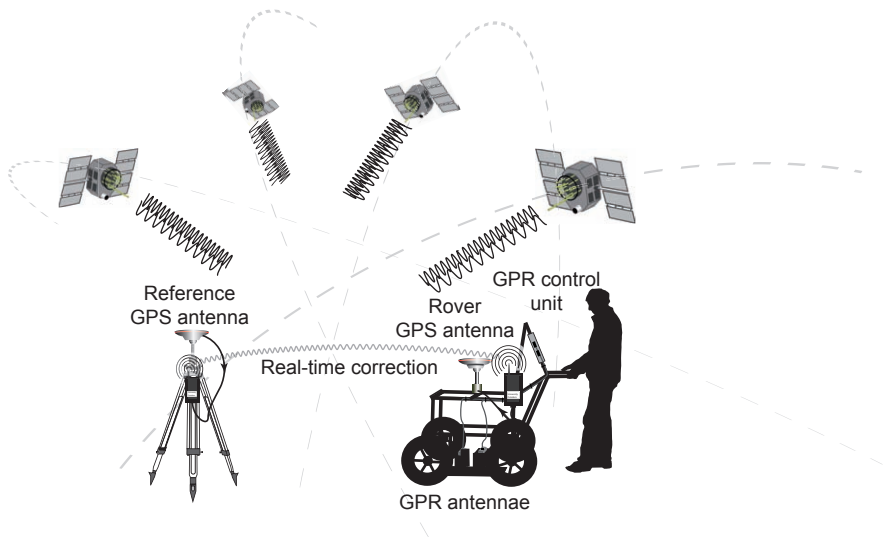


**FIGURE 1.1.** RTK-GPS based GPR surveying setup. Reference and rover GPS stations are used for real-time signal correction that allows for fusing positioning and GPR data on-the-fly. At least four satellites are required to achieve an appropriate positioning accuracy. Real-time communication is usually realized using radio communication.

tegration (Figure 1.1). The simplicity of GPS surveying has significantly contributed to its ongoing success in various fields requiring real-time positioning including geophysical studies.

Two main limitations of GPS-based surveying have to be emphasized. First, is the requirement of a line-of-sight between the GPS antennae and the satellites, which makes it impossible to use GPS systems indoor. Second, positioning errors resulting from multi-pathing, that is, the received signals are reflected (e.g., atmosphere, building, or mountain) along its propagation. These signal reflections consequently result in an erroneous pseudo-range calculation and thus, in positioning errors. Additionally, site conditions, ranging from free-field (good sight) to tree-covered (bad sight) areas, may significantly influence the positional accuracies over the extent of a survey. Such errors are difficult to quantify or even correct for.

### 1.1.2 TTS based surveying

Alternatively, Lehmann and Green (1999) introduced a self-tracking total station (TTS) based GPR surveying approach as illustrated in Figure 1.2. A total station combines angular measurements, traditionally known from theodolites, with an electronic distance measurement (EDM) based on the time-of-flight (TOF) of an infrared laser signal (see Figure 1.2). Knowledge of two angles (horizontal and vertical) and a distance is sufficient to determine the position of a point in space. Tracking total stations extend the capabilities of conventional total stations through their ability to

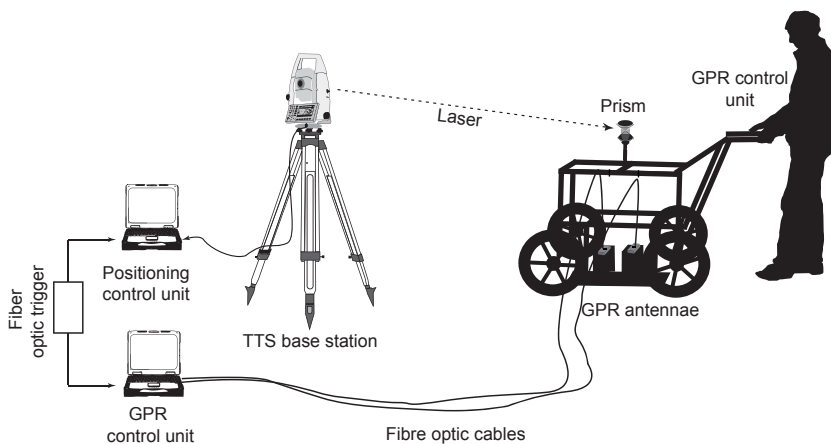


**FIGURE 1.2.** TTS based GPR surveying setup as proposed by Lehmann and Green (1999). Fixed cable connections are required for triggering and acquisition between the TTS base station and the GPR control unit. Two field computers control the positioning and GPR data acquisition of the system.

track a non-metallic 360° prism in real-time. This requires servo-driven motorization of the optical instrument and efficient automatic target-recognition algorithms. Target-recognition is based on a charge-coupled device (CCD) sensor that extracts the specific target response of the prism. Such TTS-based surveying solutions are extremely flexible as they can be used under various site conditions (e.g., indoor or forested areas). In addition, these instruments usually provide a cm-accuracy up to distances of  $\sim 1$  km with minor sensitivity to environmental conditions. However, line-of-sight is required between the TTS and the prism mounted on the surveying cart or sledge.

Figure 1.2 illustrates the surveying setup synchronizing positional and GPR data using a fiber optic trigger proposed by Lehmann and Green (1999). The major disadvantage of such a setup is the connection of the GPR control unit and the TTS via fiber optic cables. Such fixed cable connections impose constraints on the operational range and the practicability in complex terrain (e.g., covered by bushes and trees). Positioning and GPR data are stored on two individual field computers, including time markers, thus, post-acquisition processing is required to fuse the two data sets. As additional software developments and hardware modifications are needed to implement this surveying approach, it has not found wide-spread applications within the geophysical community.

### 1.1.3 Hybrid GPS-TTS based surveying

Young and Lord (2002) introduced a hybrid GPS-TTS system to overcome the fixed cable connections of Lehmann and Green (1999). This is achieved by assessing a

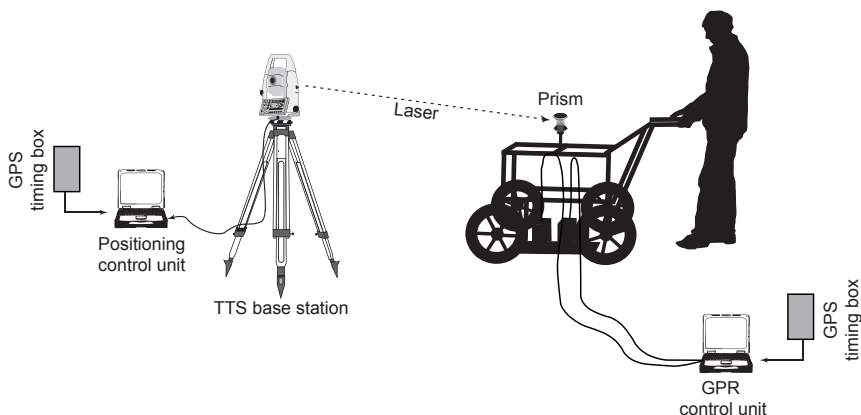


**FIGURE 1.3.** Hybrid GPS-TTS based GPR surveying setup as proposed by Young and Lord (2002). Positioning and GPR data are stored on individual field computers and GPS time markers are used to fuse the data sets in a post-acquisition processing step.

common time base through two GPS timing boxes attached to the TTS and the GPR systems. The synchronous time base can subsequently be used to fuse TTS and GPR data. Figure 1.3 schematically shows the corresponding surveying setup.

This setup represents a feasible extension because it avoids fixed cable connections between the TTS and the GPR control unit and soft- or hardware modifications. Nevertheless, this setup does not represent a real-time kinematic setup which requires on-the-fly data fusion.

### 1.1.4 RLPS based surveying

Grasmueck and Viggiano (2007) introduced another optical surveying approach illustrated in Figure 1.4. They used a rotary laser positioning system (RLPS/iGPS) developed for industrial 3D metrology (Maisano et al., 2008). Two rotary laser systems, operating at 20 Hz, continuously emit laser fans, which are registered at a laser detector (DET) attached to the surveying platform. Based on prior calibration and knowledge of the TOF from RLPS 1 and RLPS 2 to the DET, the spatial location of the DET can be calculated using the measured angles with respect to the RLPS positions. This calculation is performed at the RLPS unit attached to the GPR system. A synchronization trigger attached to the RLPS unit and the GPR data logger, is used to record the data from both instruments at the same temporal instance. The data are

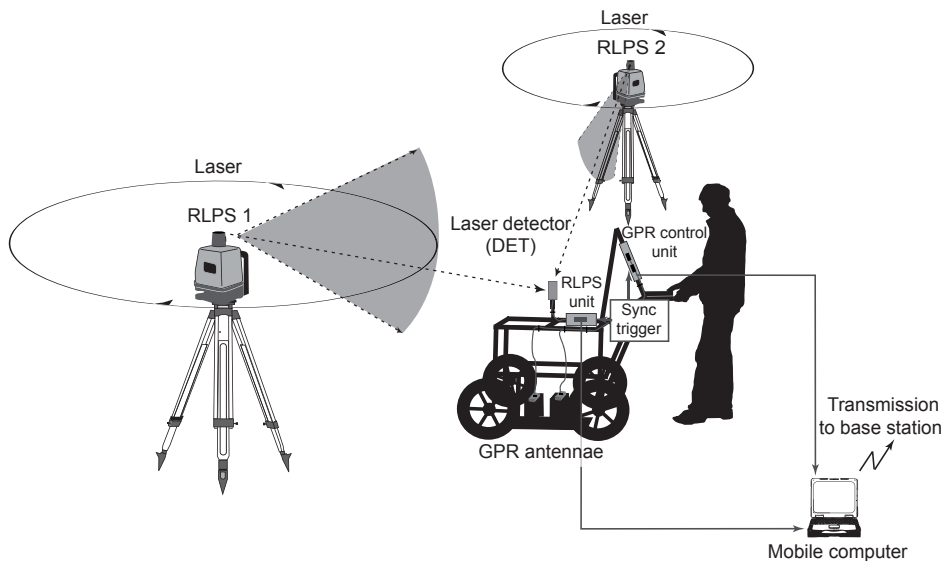


**FIGURE 1.4.** RLPS based GPR surveying setup proposed by Grasmueck and Viggiano (2007).

subsequently fused on a mobile computer and wirelessly transmitted to a base station using a wireless local area network (WLAN) connection.

Although this setup addresses most of the issues of kinematic data acquisition, there are some limitations. The communication range of each transmitter (RLPS) is currently limited to a range of  $\sim 25$  m (Maisano et al., 2008). Considering field-scale data acquisition, this limits its ubiquitous applications. Through the introduction of additional RLPSs into the setup one could address this problem. Maisano et al. (2008) further showed how the achievable positioning accuracy depends on the number of transmitters in use. They found that beyond five overlapping transmitter signals, no positional improvement could be observed and suggested, that at least three transmitters should cover the survey site.

Additionally, several hardware elements, especially the DET electronics and its cable connections, are attached to the GPR surveying platform. The introduction of additive electronic equipment onto the GPR antennae system might also result in increased system cross-talk, especially when using unshielded antennae. Lastly, this setup requires a considerable amount of hard- and software-developments. Apart from the high acquisition costs, this is probably the main reason for its limited practical application so far.

As discussed, all of the surveying solutions presented previously have their advantages and disadvantages regarding applicability, flexibility, and surveying and cost efficiency. These points have to be considered when a certain surveying solution is used for 2D or 3D GPR data acquisition. In addition, the GPR user has to consider potential cross-talk between the different instrumental components and to evaluate its influence on data quality. As shown later in this thesis, systematic latencies (i.e., the time delay between the actual position measurement by the TTS and its fusion with the GPR data) for a specific approach have to be investigated to compare the various setups in an objective manner.

## 1.2 Attribute based data analysis

*Seismic Attributes are all the information obtained from seismic data, either by direct measurements or by logical or experienced-based reasoning.*

— M. Turhan Taner, 2001

Seismic attributes were introduced in the early 1970s. The ability of an experienced seismic interpreter to visually identify and characterize complex reflection patterns

in seismic sections, given temporal or spatial waveform changes, has been acknowledged for a long time. In an attempt to capture these interpretational skills in a mathematical framework, seismic attributes have been developed.

Driven by the developments in computer hardware, Balch (1971) introduced a “computer-graphic-photographic” approach for a simultaneous visualization of frequency spectra and the original seismic waveforms. Thus, the introduction of seismic color displays has significantly contributed to the multi-dimensional data interpretation (e.g., Theophanis and Queen, 2000; Henderson et al., 2008). Following the initial development of color-based interpretation, Taner and Sheriff (1977) and Taner et al. (1979) introduced a new mathematical approach toward seismic interpretation, which they called complex trace analysis. Assuming that a recorded trace represents the real part of an analytical signal, the complex trace can be calculated through the Hilbert transform of the original signal. Until the end of the 1980s, attribute-based analyses mainly focused on instantaneous signal characteristics derived from the complex trace (e.g., instantaneous phase or frequency). Today, a variety of seismic attributes derived from the resulting real and complex part of the Hilbert transform (Chopra and Marfurt, 2007) and the Generalized Hilbert transform (Luo et al., 2003) are used.

The introduction of the 3D seismic technology in the early 1990s acted as a catalyst for an increasing development of attribute-based processing approaches. This can be considered as the onset of a broad field of seismic data analysis, incorporating state-of-the-art algorithms adapted largely from image and signal processing. Today’s applications of attribute-based data analysis ranges from fault detection (Marfurt et al., 1998; Thorseth et al., 1997; Chopra and Pickford, 2001; de Rooij and Tingdahl, 2002; Qu et al., 2008) over attribute-based facies analysis (Farzadi and Hestharnmer, 2007; Kashihara and Tsuji, 2010), to quantitative reservoir characterization (Hart and Balch, 2000; Hampson et al., 2001; Kadkhodaie-Ikhchi et al., 2009).

Figure 1.5 represents a condensed list of exemplary attributes classified after Taner (1997). Using this classification, attributes can be grouped into geometrical, physical, and corporate attributes. Geometrical attributes (e.g., dip, continuity, curvature) refer to the geometrical variation of seismic data along time slices or horizons, whereas physical attributes (e.g., instantaneous phase or frequency) are related to wave-propagation characteristics, lithology, or generally speaking, physical variations along the path of propagation (Taner, 1997). Corporate attributes define a class of attributes containing the characteristics of both geometrical and physical attributes. Taner (1997) further distinguished between pre- and post-stack attributes. In the context of this thesis, by focusing on common-offset GPR data, which can be considered to be equivalent to post-stack seismic reflection data, I have avoided such a further sub-classification.



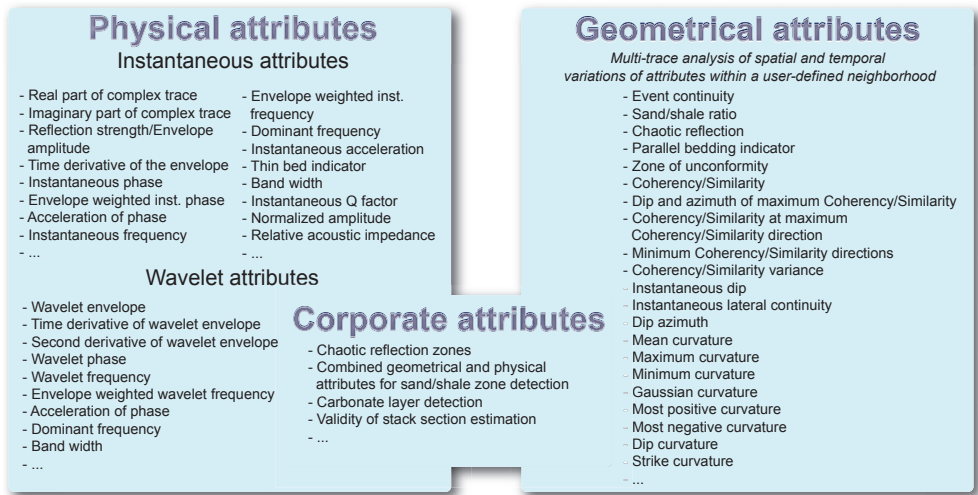


**FIGURE 1.5.** Overview of seismic attributes and their classification into geometrical, physical, and corporate attributes after Taner (1997). Given the rapidly evolving nature of attribute-based analyses, this list does not claim completeness.

Figure 1.6 shows an example of the successful application of an edge detection algorithm applied to a data volume from the Arabian Peninsula (Chopra and Marfurt, 2007). Hidden in the original amplitude time slice (Figure 1.6(a)), the application of

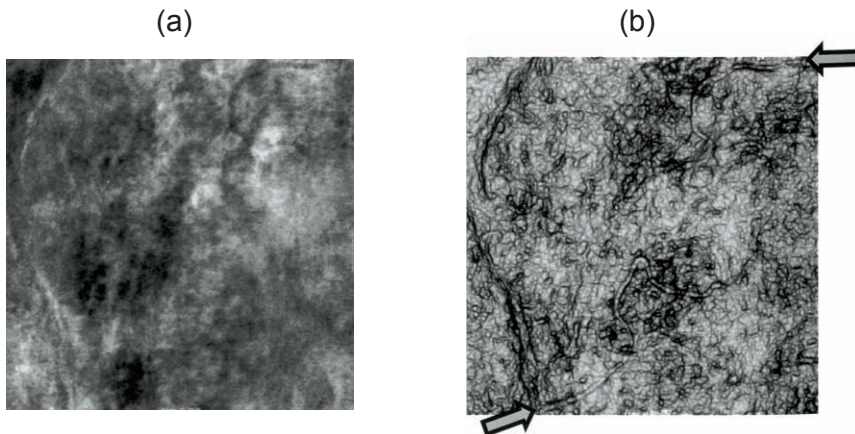


**FIGURE 1.6.** Example of attribute-based time slice analysis after Luo et al. (2003) and modified after Chopra and Marfurt (2007). (a) amplitude time slice at  $t = 1.026$  s from a 3D survey acquired in Saudi Arabia. (b) time slice after application of a multi-step, multi-window Kuwahara filtering, followed by the edge detection algorithm. Arrows identify a meandering channel not visible in the amplitude time slice.

multi-step, multi-window Kuwahara filtering, followed by the edge detection algorithm described by Luo et al. (2003), successfully highlights a meandering channel in the resulting seismic attribute volume (Figure 1.6(b)). This example clearly illustrates the benefit of attribute analysis toward more comprehensive reservoir characterizations.

Despite methodological similarities between seismic and GPR surveying, the target features to be imaged often differ from each other considerably. The broad-range of GPR applications (from geological, hydrological, archaeological to engineering targets) consequently hold a lot of potential for developing GPR specific data attributes. Nevertheless, the majority of published GPR attribute studies still address geological problems similar to those identified by the oil and gas industry. Several publications, for example, made use of seismic attributes to detect and characterize faults and fractures in 3D GPR data (Young et al., 1997; Tronicke et al., 2006; McClymont et al., 2008; Sassen and Everett, 2009).

Young et al.'s (1997) study was one of the first publications adapting state-of-the-art attribute processing to 3D GPR data. Although rarely applied by others, in their seminal work, the authors demonstrated how 3D dip-filtering followed by coherency calculation helps to clarify interpretation illustrated on a data set from a fluvial-deltaic sequence of Pennsylvanian age located in the United States midcontinent. Figure 1.7 shows a modified version of the analysis presented in Young et al. (1997) applied to a selected time slice from a 3D GPR data set collected across the Maleme Fault Zone (North Island, New Zealand). Details of this data set can be found in Tronicke et al. (2006). Similar to the application of the radon dip-rejection filter used by Young et al. (1997), the application of a dip-median filter along the local dip, calculated from a sliding 3D fast Fourier transform (FFT), allows significant enhancement of data quality and continuity. Comparing Figures 1.7(a) and 1.7(b), a clear reduction of the speckled noise and an increased feature continuity can be observed. Figure 1.7(c) shows the result extracted at a travel time of 173.2 ns from a coherency volume. Although already visible in the migrated data set, coherency enhances the individual fault strands found in this data set and reduces the potential for misinterpretation that could result from interpreting the amplitude data shown in Figures 1.7(a) and 1.7(b). To quantify the fault geometry further, Young et al. (1997) calculated the azimuth, whereas the amount of dip was used to control the hue of the used color scale. Figure 1.7(d) illustrates this analysis applied to the New Zealand 3D data set. All visible faults have a predominant azimuth of  $180^\circ$  following the y-coordinate. High dips of  $\leq 0.06$  m/ns are mostly found around  $y < -10$  m. Based on these attributes the location and geometry of the faults found at this site can be efficiently quantified. Similarly, McClymont et al. (2008) assessed fault geometries and displacement rates, also making use of coherency in combination with textural attributes to further distinguish the different geological constituents.

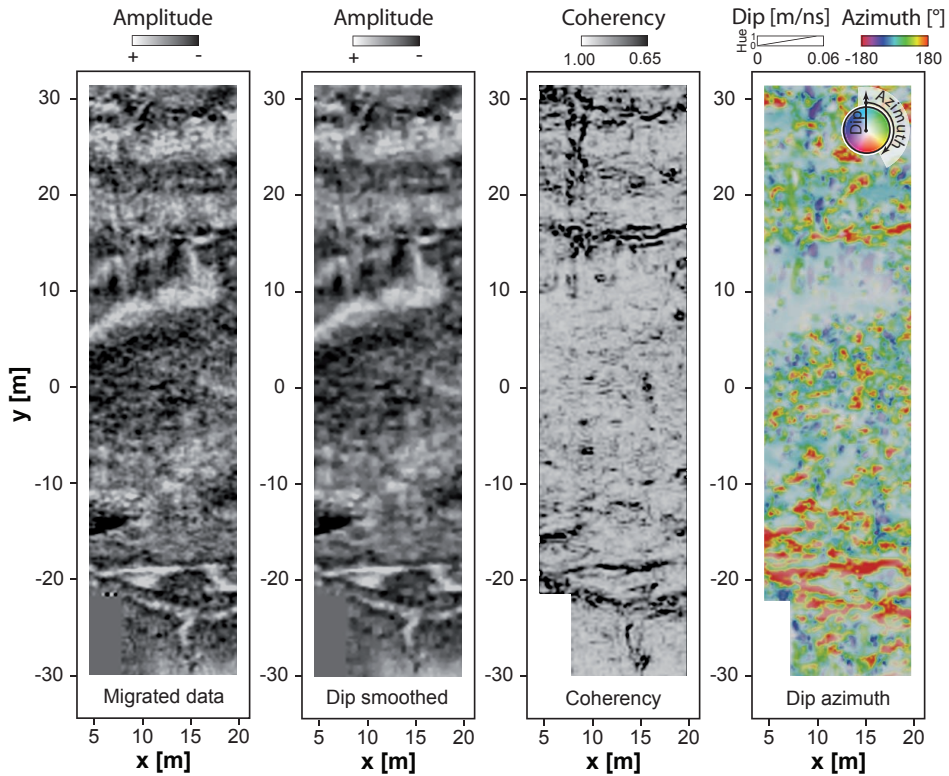


**FIGURE 1.7.** Attribute processing approach introduced by Young et al. (1997), modified and calculated for a 3D data set presented by Tronicke et al. (2006). Time slices are located at 173.2 ns ( $\sim 5.32$  m depth). Data extracted from the (a) raw data volume, (b) the dip-median filtered data volume, (c) the coherency volume, and (d) the dip-modified azimuth volume.

In addition to geological targets, first attempts have been made to use attribute analysis to identify other GPR specific targets. For example, within the past decade, the social demands, to assess unexploded ordnance (UXO) have significantly influenced the advances of 2D and 3D GPR processing. This increased focus has resulted in a variety of attributes (no terminological consensus in this context) to extract and characterize buried UXOs (e.g., Daniels, 2004; Karlsen et al., 2001; Ng et al., 2008; Zeng et al., 2009). Another evolving field, which Thomas et al. (2009) recently brought to attention, is the stakeholders need for precise utility detection. World-wide, unregistered utilities pose significant safety problems. Apart from the human danger, the annual industrial and societal costs, in the United Kingdom for example, are estimated to be around £1.5 billion per year (McMahon et al., 2005). Within this context, certain characteristic GPR features (e.g., the shape of diffraction hyperbolas) have

been evaluated in order to detect and characterize buried utilities (e.g., Al-Nuaimy et al., 2000). Such studies indicate the potential of attribute analyses for GPR specific targets and illustrate that there is definitely an increasing need for high-resolution, efficient, 3D methods to characterize near-surface environments. Therefore, it can be assumed that the need for high-precision 3D GPR surveying and efficient analysis and interpretation will become increasingly important in the years to come.

### 1.3 Objectives and outline of this thesis

Successful applications of 2D or 3D attribute analyses, as mentioned before, require that the recorded GPR traces are localized at a high spatial accuracy. Especially, when multi-trace attributes (i.e., attributes calculated considering information from neighboring traces) are employed, positioning errors might be critical. Thus, the first goal of this thesis is to develop and evaluate the possibilities for efficient and robust, kinematic GPR data acquisition at a high spatial accuracy. Afterward, considering state-of-the-art GPR data acquisition, the potential of attribute based processing flows will be investigated. Consequently, the second goal of this thesis is to evaluate and develop attribute-based processing flows tailored to selected GPR specific problems. This thesis predominantly focuses on applications found in archaeology and engineering.

Kinematic near-surface geophysical data acquisition has been an emerging field over the past decades, for example, to acquire large 3D GPR data sets in a very cost-effective manner. Chapter 2 presents a flexible and efficient combination of GPR and a modern TTS using wireless data transmission, making use of the possibility to transmit positional data in a GPS-like data format. The influence of wireless transmission and real-time data fusion on the GPR data quality and spatial accuracy is studied. It is shown that signal degradation through systematic cross-talk only occurs in close vicinity to the TTS system. It is also shown that through repetitive acquisition of a calibration profile in the forward and reverse manner, one can assess the magnitude of the so-called system latency. Latency, that is, the time elapsed until a measurement is available at the data logger, is inherent to all real-time applications to varying degrees and has so far not been evaluated systematically in kinematic GPR surveying. These studies show that modern TTS systems provide the capability to acquire high-precision GPR data under a variety of conditions.

Coherency and similarity represent multi-trace attributes developed to highlight faults in oil reservoirs. Knowledge of the geometry and distribution of these fault systems is of major importance to assess the quality of a reservoir in the deployment phase. So far, applications of these attributes for GPR are limited to the problem of fault identification. Considering the broad field of application of 2D or 3D GPR surveying, fault identification only plays a minor role. Nevertheless, waveform similarity

(i.e., coherency and similarity) provides a feasible attribute to address different types of problems. In Chapter 3, I present two high-resolution indoor 3D GPR data sets acquired at two different archaeological sites using the developed TTS based surveying approach. I show how coherency and similarity successfully highlight and isolate the target archaeological structures. Compared to conventional processing and analysis strategies (using, for example, migrated amplitude data), this attribute-based analysis is a major improvement as the archaeological features are significantly enhanced.

Chapter 4 shows how integrated data analysis using composite imaging allows further enhancement the interpretation. Multiple data sets, namely GPR, magnetic, and high-resolution topographic data have been collected across an archaeological site in Paretz, Germany. Composite imaging refers to a display technique to visualize multiple data sets simultaneously by assigning each data set (including attributes derived from the data) to an individual RGB and potentially an alpha channel. In such a complementary fashion it can be shown how the different data sets complement each other and result in a more comprehensive interpretation of the archaeological targets.

Polarization of electromagnetic wavefields at subsurface scatterers represents an important phenomenon, which many GPR applications usually ignore. In Chapter 5, a novel processing scheme to highlight such polarization effects is introduced for improved detection and characterization of buried utility pipes, which represents one of the most relevant engineering targets for GPR. The novel GPR attribute, called depolarization, combines geometrical and physical information into a single measure. Extraction of geometry related information makes use of the intrinsic symmetry of man-made subsurface targets. Phase symmetry is an image feature introduced to highlight symmetric features within images based on log-Gabor filter-bank decomposition. Isolation of these features also allows for efficiently determining the feature angle. Physical characterization makes use of the polarization effect itself through the determination of a so-called feature angle derived from principle component analysis (PCA) of dual-component GPR data. It is shown that through a combination of these attributes the magnitude of polarization can be effectively highlighted. This also allows the classification of different materials based on their polarization characteristics.

In Chapter 6, a novel tree-based pursuit approach is introduced to analyze GPR data. This allows for high-resolution time-frequency analysis using various wavelet dictionaries. Matching pursuit approaches have shown to provide detailed results to study temporal frequency variations. Tree-based approaches significantly increase the efficiency of the atomic decomposition through tree-structure atom matching. Incorporation of phase variation into the matching procedure can be done in two ways. First, phase information can be introduced into the waveform itself. Second, I introduce an alternative approach by incorporating the phase into the signal to be decomposed. Considering that for several commonly used geophysical waveforms,

modifications, including phase variation is not straightforward, it is shown that the alternative approach provides large flexibility for waveform usage. Tree-based pursuit thereby allows extraction of the dominant waveforms in a greedy manner, providing frequency and phase information simultaneously. Apart from the classical application to highlight thin-beds, I demonstrate the potential of processing using sparse atomic decompositions.

Chapters 2, 3, and 4 have been published or are in press in *IEEE Transactions on Geoscience and Remote Sensing*, *Journal of Archaeological Science*, and *Geophysics*, respectively. Chapter 5 and 6 have been submitted to *IEEE Transactions on Geoscience and Remote Sensing* and to *Journal of Applied Geophysics*, respectively.

# ON THE POTENTIAL OF KINEMATIC GPR SURVEYING USING A SELF-TRACKING TOTAL STATION: EVALUATING SYSTEM CROSS-TALK AND LATENCY

**Böniger U., Tronicke, J.**

*IEEE Transactions on Geosciences and Remote Sensing*, 2010, **48** (10), 3792 – 3798,  
doi: 10.1109/TGRS.2010.2048332

Published by IEEE Geoscience and Remote Sensing Society

---

## 2.1 Abstract

In this study, we present an efficient kinematic ground-penetrating radar (GPR) surveying setup using a self-tracking total station (TTS). This setup combines the ability of modern GPR systems to interface with Global Positioning Systems (GPS) and the capability of the employed TTS system to immediately make the positioning information available in a standardized GPS data format. Wireless communication between the GPR and the TTS system is established by using gain variable radio modems. Such a kinematic surveying setup faces two major potential limitations. First, possible crosstalk effects between the GPR and the positioning system have to be evaluated. Based on multiple walkaway experiments, we show that, for reasonable field setups, instrumental crosstalk has no significant impact on GPR data quality. Second, we investigate systematic latency (i.e., the time delay between the actual position measurement by TTS and its fusion with the GPR data) and its impact on the positional precision of kinematically acquired 2D and 3D GPR data. To quantify latency for our kinematic survey setup, we acquired forward–reverse profile pairs across a well-known subsurface target. Comparing the forward and reverse GPR images using three fidelity measures allows determining the optimum latency value and correcting for it. Accounting for both of these potential limitations allows to kinematically acquire high-quality and high-precision GPR data using off-the-shelf instrumentation without further hardware modifications. Until now, these issues have

not been investigated in detail and, thus, we believe that our findings have significant implications also for other geophysical surveying approaches.

## 2.2 Introduction

Driven by recent hardware developments allowing for higher sampling frequencies and longer continuous data acquisition, high-resolution three-dimensional (3D) ground-penetrating radar (GPR) has become an increasingly popular technique in a variety of disciplines including engineering, hydrology, and archaeology (Knight, 2001; Aaltonen and Nissen, 2002; Daniels, 2004; Troncke et al., 2006; Streich and van der Kruk, 2007; Francese et al., 2009). In order to address current and future environmental and engineering problems, efficient surveying solutions as well as reliable high-resolution data sets are required. The improvements provided by high-resolution 3D data acquisition (i.e., dense data coverage at a high positional accuracy) have been acknowledged (e.g., Grasmueck et al., 2005). The increase in sampling frequency of today's GPR systems requires a high spatial coordinate accuracy in order to adequately account for the more detailed database. Although there has been a steady development in post-processing algorithms, increasing the efficiency and precision of the positioning procedure has only recently been studied.

Over the past decade, several authors have presented kinematic acquisition strategies jointly acquiring GPR and positional data (e.g., Lehmann and Green, 1999; Aaltonen and Nissen, 2002; Young and Lord, 2002; Grasmueck and Viggiano, 2007). Apart from the spatial localization of each individual GPR trace, such approaches additionally provide a high-resolution digital terrain model of the survey site, which, for example, is essential to accurately migrate GPR data at sites with significant topography (Lehmann and Green, 2000) or multi-component data sets acquired separately (Streich and van der Kruk, 2007). Additionally, local topographic variations might also be linked to subsurface targets and thereby represent another data source for interpretation (Kvamme et al., 2006; Piro et al., 2007). A prerequisite for joint acquisition of GPR and positional data is the potential to obtain 3D coordinates at a frequency usually within the order of the sampling frequency at which the GPR instrument operates. The inability to meet this requirement with high positional accuracy (usually, a few centimeters are required) made joint surveying (positional and GPR) impracticable for several decades. However, recent advances in modern surveying systems, especially in Global Positioning Systems (GPS) and tracking total stations (TTS) (e.g., Schofield and Breach, 2007), allow GPR users to overcome these limitations. Recently, several feasible solutions for real-time kinematic data acquisition have been presented. These solutions can be divided into post-acquisition and real-time data fusion approaches.



Post-acquisition data fusion refers to merging GPR and positional data subsequent to the field survey. In order to perform the actual data merging, these methods must overcome the problem of data synchronization. To this end, the study in Lehmann and Green (1999) introduced an acquisition approach combining a GPR unit with a high-precision TTS, which automatically tracks a 360° prism mounted on the GPR antennae sledge. The two simultaneously acquired data sets were recorded using two field computers linked to both systems (GPR and TTS) via fixed cable connections. These cables reduce the flexibility and practicability of this approach. More recently, Young and Lord (2002) also used a TTS-based approach, but overcame the aforementioned limitations of fixed cable connections by employing two GPS receivers providing synchronous time markers used for subsequent data merging.

In contrast to post-acquisition data fusion approaches, real-time data fusion refers to combining GPR and positional data on-the-fly (i.e., while the data are recorded in the field). Ideally, this eliminates the need for any post-acquisition processing. Due to the popularity and the potential accuracy of the latest GPS systems (usually dual frequency systems used in RTK mode), most of today's GPR instruments are equipped with an RS232 port providing an interface for continuous GPS data streams. As a result, data loggers combine the GPR and the GPS data during acquisition. Therefore, GPS-based surveying represents the first mainstream, real-time GPR acquisition solution offering automatic data fusion using off-the-shelf instruments without additional hardware and/or software modifications (e.g., Aaltonen and Nissen, 2002; Paoletti et al., 2005; Onishi et al., 2005; Streich et al., 2006). An additional real-time approach has been developed by Grasmueck and Viggiano (2007) based on a rotary laser positioning system (RLPS). Fusion of the two data sets is achieved by using the RLPS internal clock for linking GPR and positional data in real-time.

Even though dual-frequency RTK GPS surveying has proven to be a simple, fast, and feasible surveying solution, it is not applicable to all geophysical site settings. Environmental variables, including satellite coverage, atmospheric conditions, and multi-pathing, affect the positional accuracy of a GPS. In case of obstructed satellite view (e.g., in valleys, urban areas, or indoor), the system may even be rendered inoperable. If operable, GPS solutions are still often affected by temporal variations in signal quality which may result in varying positional accuracies over the extent of a survey. This effect is very difficult to be corrected for (see Dimc et al., 2006) and its impact on kinematic GPR data acquisition is often neglected. On the other hand, TTS systems provide continuous positional precision over the entire survey with a very limited sensitivity to environmental variables. We believe that TTS systems hold a lot of potential, but that a thorough study of the applicability and performance using modern TTS systems for kinematic GPR data acquisition is required.

In the following, we present a TTS-based GPR surveying setup using off-the-shelf instrumentation. We further study two main aspects of this setup, which have to be

considered when acquiring GPR data in such a kinematic fashion. First, we study system cross-talk between the positioning and the GPR system and quantify its influence on GPR data quality. Second, we study the so-called systematic latency in order to qualitatively assess the positioning accuracy of the GPR data traces. We believe that these two aspects are of major importance for every kinematic surveying approach.

## 2.3 TTS Based GPR Surveying

Most of today's kinematic high-precision applications (e.g., machine guidance for leveling) make use of TTS systems in order to achieve the often required subcentimeter positioning precision (Ingensand and Stempfhuber, 2008). Figure 2.1 shows our kinematic surveying setup for GPR data acquisition, combining a modern GPR instrument (pulseEKKO PRO; Sensors&Software) with a tripod-mounted TTS (TPS1200; Leica Geosystems) acting as base station. Automatic tracking of a 360° prism allows kinematic surveying with positional update rates of up to 10 Hz. GPR surveying (3D in particular) usually requires a positional precision within the centimeter range in order to accurately process and interpret the data. As stated by the manufacturer, the positional accuracy of the used TTS is  $\sim 0.003$  m (up to distances of 600 m) in the auto-tracking mode, which is typical for most modern TTS systems. The study in Lehmann and Green (1999) has already presented a comparison of kinematically and statically positional data acquired using a similar TTS. They found that, for moderate

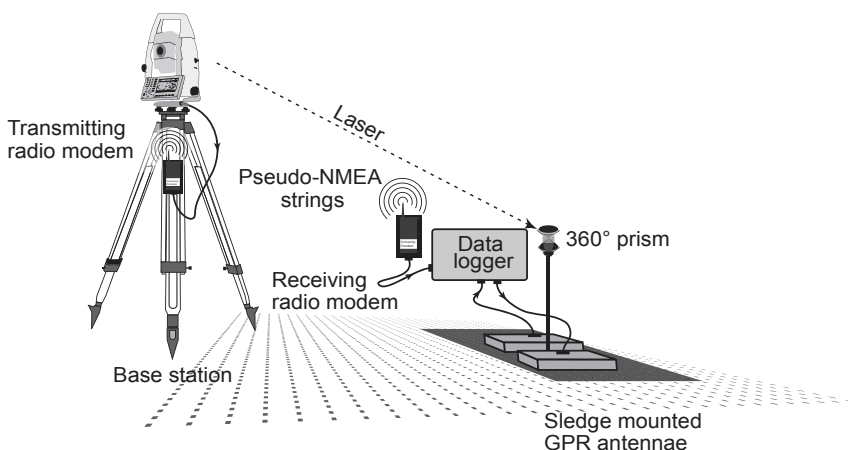


**FIGURE 2.1.** Sketch of the acquisition setup (not to scale). Static base station (TTS) combined with a GPR instrument equipped with a 360° prism (TTS mode). Arrows along the cable connections indicate data flow directions.

walking speed, the kinematically acquired coordinate accuracy is within the accuracy range stated by the manufacturer.

To avoid fixed cable connections and improve flexibility in the field, we establish a real-time data exchange between the TTS and the GPR unit using two gain variable (-10–14 dBm) radio modems (NiceCom901; Amber Wireless), which are connected to the TTS communication port and the GPS data port at the data logger. These radio modems operate in the 868-MHz band and use a frequency modulation technique known as frequency-shift keying. They operate at a default gain of 13 dBm resulting in a maximum transmission range of  $\sim 2$  km. While the TTS automatically tracks the 360° prism, which is mounted onto a surveying platform (e.g., sledge or cart), the positional information is continuously streamed to the GPR system via the radio modems. Fusion of the positional and the GPR data makes use of so-called pseudo-NMEA (Leica terminology) strings commonly implemented into modern TTS systems. Pseudo-NMEA means that TTS positional information is converted into a GPS-like format, i.e., mimicking the use of a GPS system to the GPR unit. Compared to other presented approaches, such a setup is as simple as GPS based approaches as it avoids additional hardware and/or software developments. Furthermore, definition of a local coordinate system, using the local resection method, allows to orient local North or East along the inline direction. The resection method is well known from engineering surveying to establish the coordinates of points by observations to or from known points (Schofield and Breach, 2007). In our case, application of the local resection is based on two points located along the user-defined inline orientation of the survey grid. This facilitates further processing steps, making coordinate rotations (as used by Lehmann and Green, 1999) obsolete. Additionally, we employ a GPS repeater display (not included into Figure 2.1) in order to navigate along coordinate isolines, avoiding the setup of a additional reference line (e.g., a using measuring tape or spray paint). To further evaluate our surveying setup, we investigate the potential cross-talk between the positioning system and the GPR unit and potential transmission latencies.

## 2.4 Influence of cross-talk on data quality

To quantify the influence of potential cross-talk between the GPR system and the TTS positioning systems, which include radio communication, we designed a special walkaway experiment. The GPR data were acquired using a sledge-mounted and unshielded 200-MHz antenna pair with a fixed antenna offset of 1.0 m. We used 32 vertical stacks and a sample interval of 0.05 ns in order to adequately sample potential high frequency noise. Simulating realistic field data acquisition, the sledge was steadily pulled away from the TTS system, equipped with the transmitter modem, while the receiving modem was carried by the operator ( $\sim 1.5$  m in front of the

sledge). Midpoint offsets (i.e., the distance between the TTS system and the midpoint between the two GPR antennae) of up to 20 m were recorded. This experiment was repeated for four different scenarios: without TTS positioning and radio communication using step-mode acquisition and measuring tape, as well as with TTS positioning and radio communication using 12-, 10-, and 6-dBm modem gains in RTK acquisition mode.

In order to study the influence of potential cross-talk, Figure 2.2 compares the selected GPR trace spectra acquired without using TTS positioning and radio communication (solid gray) with the trace spectra acquired using TTS positioning and radio communication at 12 dBm modem gain (solid black). The shown trace spectra were recorded at three different offsets; i.e., 0.60, 6.25, and 16.20 m. For the intermediate- and far-offset range, the spectra recorded without and with the TTS positioning system are similar indicating that the positioning system has no significant influence on GPR data quality. For the near-offset range, the higher noise level introduced by the TTS and the radio modems, respectively, is obvious, especially, at frequencies  $> 500$  MHz; i.e., at frequencies beyond the actual GPR signal bandwidth. As a result of the frequency modulation technique of the used radio modems in combination with the sequential GPR receiver, the modem signals in the 868 MHz band are not adequately sampled by the GPR system. Most time-domain GPR systems (such as the one used in this study) do not sample the received waveforms in real time. They rather employ sequential receivers utilizing the equivalent-time sampling approach, which requires repetitive waveforms throughout the entire sampling cycle (Koppenjan, 2009).

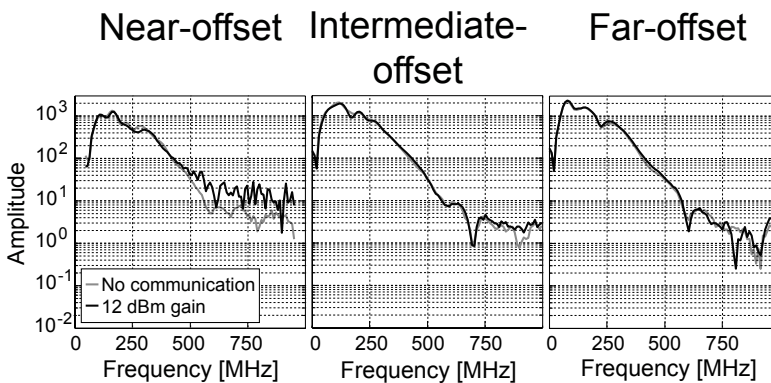


**FIGURE 2.2.** Influence of radio communication on selected GPR trace spectra. Comparison of the amplitude spectra recorded using 200-MHz unshielded GPR antennae in the near- (0.60 m), intermediate- (6.25 m), and far-offset (16.20 m) range for data recorded (gray) without TTS positioning and no radio communication and (black) with real-time TTS positioning and radio communication using 12-dBm gain.

To further assess the offset-dependent impact of the positioning system on GPR data quality, we calculated the signal-to-noise ratio (SNR) from the raw data through power spectral densities using Burg's algorithm (Stoica and Moses, 1997) over all recorded midpoint positions. The noise and signal window were defined as a 27.5-ns-long window prior and after the first breaks, respectively. Figure 2.3 shows the SNR as a function of midpoint offset. The influence of TTS-based positioning using radio communication on the SNR is clearly visible. Depending on the applied gain, the positioning system degrades the SNR up to distances of  $\sim 4\text{--}6$  m. The receiving modem, on the other hand, does not have a significant contribution to the noise level as measurements, including radio communication, reach the same SNR range (plateau beyond  $\sim 10$  m) as the step-mode measurements without TTS and radio modems. Additionally, Figure 2.3 shows, as to be expected, that decreasing modem gain improves SNR. For the selected unshielded 200-MHz antennae, this experiment illustrates that the influence of the positioning system can be neglected for distances beyond  $\sim 4\text{--}6$  m, depending on the used gain. In this context, it should also be noted that, in kinematic field applications requiring a positioning accuracy in the centimeter range, the distance between the TTS and the prism to be tracked should be at least several meters because at smaller distances, the angular velocity of the TTS might have a significant impact on the positioning accuracy (Lehmann and Green, 1999). Additionally, we would like to highlight that our results presented above can

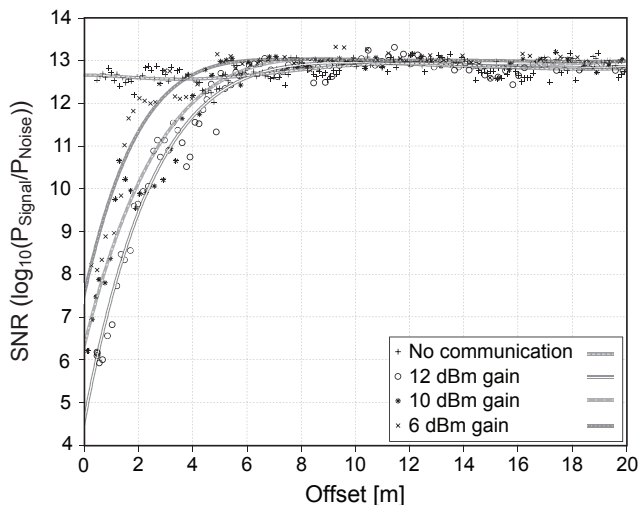


**FIGURE 2.3.** SNR versus midpoint offset (distance from transmitting modem attached at the TTS to the midpoint of the antennae pair) illustrating the influence of radio communication (without radio communication and with radio communication) using 12-, 10-, and 6 dBm modem gains on GPR data collected using unshielded 200-MHz antennae.

be regarded as a worst-case scenario because we have used unshielded GPR antennae. Thus, further significant attenuation of cross-talk effects could be achieved by making use of shielded antenna systems as they are preferentially used for high-frequency (>500 MHz) GPR surveys. Furthermore, digital filters might be effective to suppress cross-talk-related noise, e.g., if the noise is separated from the effective frequency band of the employed GPR antennae. We conclude that, for reasonable field setups (i.e., the distance between TTS and GPR antennae in the order of several meters), instrumental cross-talk has no significant impact on GPR data quality. However, when using other geophysical hardware (e.g., a GPR system utilizing real-time sampling or magnetometers), we recommend to perform similar experiments to quantify potential cross-talk effects.

## 2.5 Latency Estimation and Correction

The positional precision of kinematically acquired GPR data is predominantly governed by two factors — the accuracy of the positioning system in use and a systematic latency. Latency is well known in other disciplines such as civil engineering (e.g., Bouvet and Garcia, 2000) but it has been largely ignored in near-surface geophysical surveying so far. We therefore believe that a detailed discussion of latency effects is an important topic that has to be addressed when acquiring GPR data in a kinematic fashion.

Latency refers to the time elapsed between the *measure instance* and the availability or visibility of the measurement. For GPR data acquisition, this refers to the time delay between the actual position measurement (using a GPS or TTS system) and its fusion with the GPR trace. In our acquisition setup (Figure 2.1), this time delay is introduced by processing within the TTS and GPR and data transfer via cables and modems. In this study, latency is regarded as being stationary as no temporal variations have been recognized by the authors in this and numerous other experiments. We refer to latency as the total latency ( $l_{Tot}$ ) being the sum of the individual contributions from each hardware system ( $l_{TTS}$ ,  $l_{Modem}$ , and  $l_{GPR}$ ):

$$l_{Tot} = l_{TTS} + l_{Modem} + l_{GPR}. \quad (2.1)$$

Figure 2.4 shows the effect of latency and, if  $l_{Tot}$  is constant and known, its correction. For a specific trace, the coordinate  $C(t^{meas})$  that is visible at the GPR unit when merging TTS coordinates and GPR data is incorrect because  $C(t^{meas})$  is the position of a trace measured  $l_{Tot} = t^{meas} - t^{corr}$  before. If  $l_{Tot}$  is known, the coordinate  $C(t^{corr})$  can be evaluated at  $t^{corr}$ , and it is assigned to the trace measured at  $t^{meas}$ . Assessing latency experimentally, considering stationarity of  $l_{Tot}$ , should result in

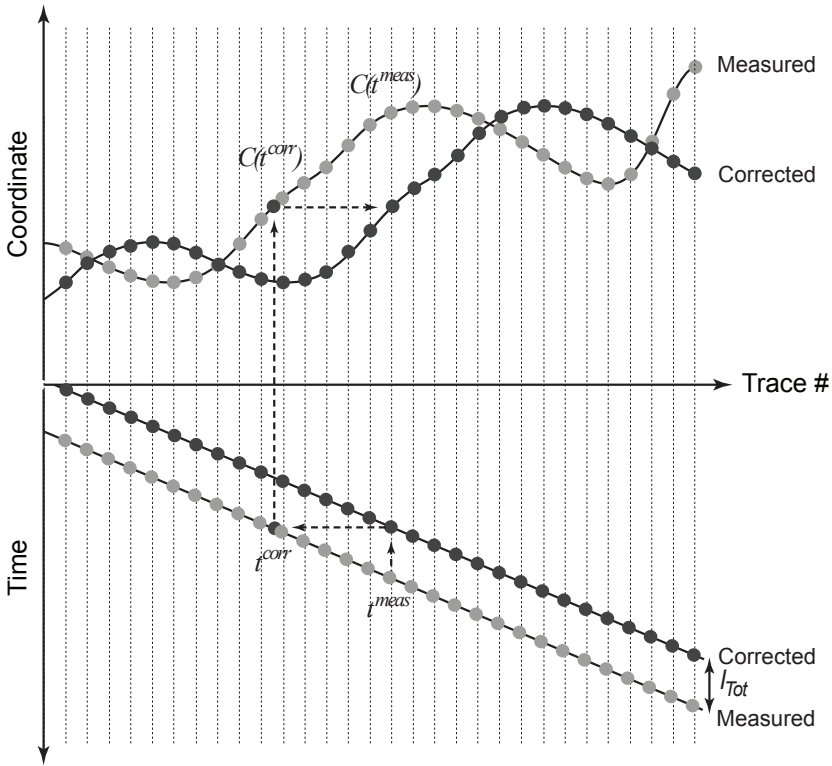


**FIGURE 2.4.** Sketch illustrating the effect of latency ( $l_{Tot} = t^{meas} - t^{corr}$ ) and its correction if its magnitude is constant and known. For details, see text.

low variance estimates of  $l_{Tot}$  over multiple realizations for a fixed survey setup and different acquisition speeds.

To study latency we collected 2D and 3D GPR data at a field site with buried metallic pipes known from excavations. The expected strong diffractions from these objects and their linear lateral extent are beneficial in determining and highlighting the influence of latency on 2D and 3D GPR data. The experimental setup consisted of a pair of sledge-mounted unshielded 200 MHz antennae with a fixed antennae offset of 1.0 m, using a sample interval of 0.2 ns for both 2D and 3D data acquisition. To estimate  $l_{Tot}$ , we recorded the same profile in forward ( $d^f$ ) and reverse ( $d^r$ ) directions using different acquisition speeds. In the case  $l_{Tot} = 0$  (no latency), subsurface structures (e.g., diffractions and reflectors) would be positioned at the same locations, i.e., independent of profile direction (forward or reverse) with the accuracy provided by the TTS system. In the case  $l_{Tot} > 0$ , we would expect, when comparing forward and reverse profiles, that the same subsurface objects would not be located at the same position. Correcting latency (as shown in Figure 2.4) using increasingly larger

latency times would spatially relocate the structures up to the best match ( $l_{\text{Opt}}$ ) and would subsequently separate them again.

As the alignment or match of a latency corrected profile pair ( $d^f, d^r$ ) acquired at walking speeds can not be quantified visually, we make use of different fidelity measures to describe the likeness of a corrected profile pair. In addition to the well known correlation coefficient ( $\text{Corr}(d^f, d^r)$ ) and mean squared error ( $\text{MSE}(d^f, d^r)$ ), we use the Structural Similarity Index ( $\text{SSIM}(d^f, d^r)$ ). In the field of image processing, the SSIM and its modifications have shown to be superior compared to more classical fidelity measures such as MSE. For a tutorial paper, we would like to refer the interested reader to Wang and Bovik (2009). For our application, the SSIM can be defined as (Wang et al., 2004):

$$\text{SSIM}(d^f, d^r) = \frac{(2\mu_{df}\mu_{dr} + C_1)(2\sigma_{df,dr} + C_2)}{(\mu_{df}^2 + \mu_{dr}^2 + C_1)(\sigma_{df}^2 + \sigma_{dr}^2 + C_2)}, \quad (2.2)$$

where  $\mu$  is the mean,  $\sigma$  is the standard deviation, and  $\sigma_{df,dr}$  is calculated by

$$\sigma_{df,dr} = \frac{1}{N-1} \sum_{i=1}^N (d_i^f - \mu_{df})(d_i^r - \mu_{dr}). \quad (2.3)$$

$N$  equals the number of samples, and  $C_1$  and  $C_2$  are constants that are used to avoid instabilities (for details see Wang et al., 2004). To incorporate local information of the two images to be compared, the study in Wang et al. (2004) additionally introduced the mean SSIM (MSSIM). Compared to the global calculation as given in Equation (2.2), the MSSIM corresponds to the structural similarity calculated within sliding windows over the entire data set (Wang et al., 2004). In order to avoid ‘‘blocking’’ artifacts in the MSSIM calculation, the study in Wang et al. (2004) further introduced the application of a rotationally symmetric Gaussian filter prior to the calculation of the local statistics. In this study we always used a Gaussian filter of size 11 (samples) using a standard deviation of 1.5 (samples). For the aforementioned fidelity measures, we define the optimum latency ( $l_{\text{Opt}}$ ) as

$$l_{\text{Opt}}^{\text{Corr}} = \arg \max_l \text{Corr}(d_l^f, d_l^r), \quad (2.4)$$

$$l_{\text{Opt}}^{\text{MSE}} = \arg \min_l \text{MSE}(d_l^f, d_l^r), \quad (2.5)$$

and

$$l_{\text{Opt}}^{\text{MSSIM}} = \arg \max_l \text{MSSIM}(d_l^f, d_l^r). \quad (2.6)$$



For our 2D experimental GPR data, Figure 2.5 compares the different fidelity measures for one selected profile pair. Basic data processing includes dewow filtering and dc removal. Latency corrections between 0 and 1 s using a step size of 0.002 s are evaluated. The latency corrected data are gridded onto an inline spacing of 0.3 m using an inverse distance gridding algorithm. The MSE and MSSIM are normalized to their maxima for display. All measures show a distinct similar extremal latency ( $l_{\text{Opt}} \approx 0.416$ ) but with differing sharpness. Particularly, the correlation coefficient shows a less distinct extremum compared to MSE and MSSIM.

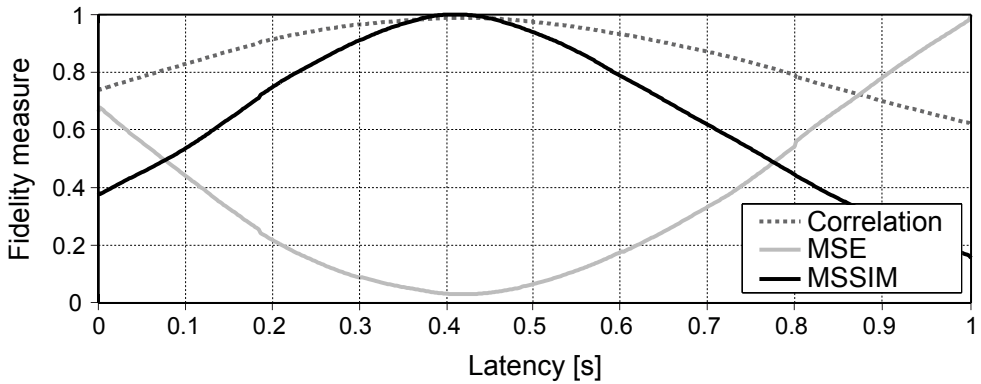


**FIGURE 2.5.** Variation of different fidelity measures between the forward ( $d^f$ ) and reverse ( $d^r$ ) direction for a selected profile pair using latency corrections between 0 and 1 second using a discretization of 0.002 s. The MSE and MSSIM measures have been normalized to their maxima for display.

Figure 2.6 shows the optimum latencies for 13 profile pairs acquired at walking speeds ranging from  $\sim 0.1$  to  $\sim 1.4$  m/s (acquisition speed sorted). All three fidelity measures result in approximately the same mean latency ( $\mu_{\text{Lat}}$ ) of about 0.416 s with no obvious dependence on acquisition speed. While the correlation coefficient and the MSE have high standard deviations of about 0.025 s, the MSSIM results in a rather small standard deviation of 0.006 s, outperforming correlation and MSE. Considering the aforementioned prerequisites of a successful experimental latency assessment, we believe that the MSSIM fidelity measure provides the best estimate of latency from our experimental data. For example, considering a walking speed of 0.5 m/s, the trace mispositioning for a latency of 0.416 s would be in the order of 0.21 m for each trace. Applying a latency correction, as shown in Figure 2.4, would thereby reposition each trace and the resulting positioning accuracy would be  $\pm 0.003$  m (using  $\sigma_{\text{Lat}}$  MSSIM).

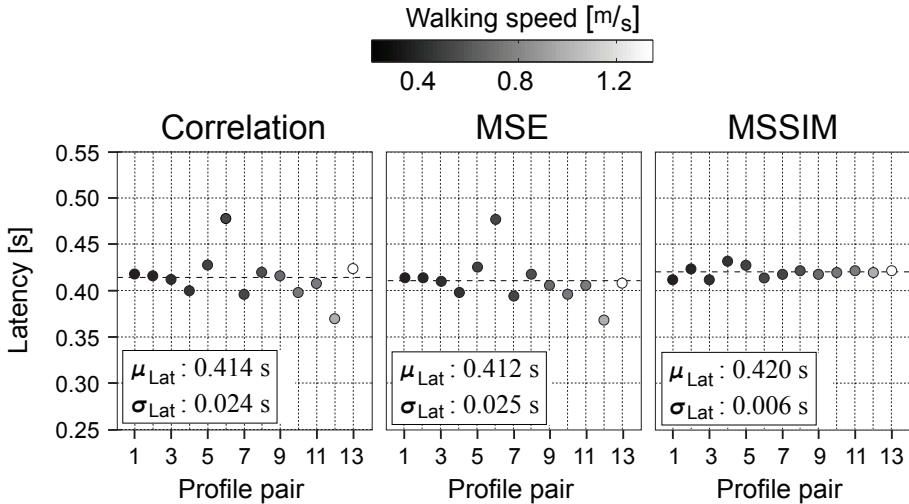


**FIGURE 2.6.** Determining optimum latency with three different fidelity measures using 200 MHz GPR data. Optimum latencies at fidelity extrema for 13 profile pairs acquired at different walking speeds are shown. Grayscale coding indicates mean walking speed of the corresponding profile pairs. For comparison, mean latency ( $\mu_{\text{Lat}}$ ) and standard deviation ( $\sigma_{\text{Lat}}$ ) are presented for each fidelity measure.

To demonstrate the impact of latency corrections, Figure 2.7 shows one selected profile pair corrected using three different latencies (0, 0.42, and 0.85 s). Visual evaluation of the forward and reverse profile for the different corrections is very difficult. On the other hand, calculating the difference between the two profiles ( $d^f - d^r$ ), shows that there are significant positional shifts for the un- and overcorrected profiles. Correction based on the MSSIM ( $l_{\text{Opt}}^{\text{MSSIM}}$ ) shows no structural (e.g., diffractions) residuals (see Figure 2.7(b)).

To further illustrate the effect of erroneous latency corrections, Figure 2.8 shows a selected timeslice from the raw 3D data set (acquired using an in- and crossline trace spacing of  $\sim 0.10$  m). In order to maximize the visibility of the expected zigzag patterns, we decided to grid the data set using a basic nearest neighbor algorithm and a  $0.05 \times 0.05$  m regular grid. In this case including multiple spatial neighbors into the gridding algorithm might introduce undesired averaging effects that attenuate the visibility of potential zigzag patterns. Given the knowledge of linear metallic pipes buried at our field site, an optimal latency correction would align pipe diffractions and provide sharp continuous feature edges. While Figure 2.8(a) (uncorrected) and Figure 2.8(c) (overcorrected) show significant zigzag patterns, Figure 2.8(b) provides a sharp image without significant zigzag patterns. This example clearly illustrates the importance of using an appropriate latency correction when acquiring high-resolution GPR data sets.

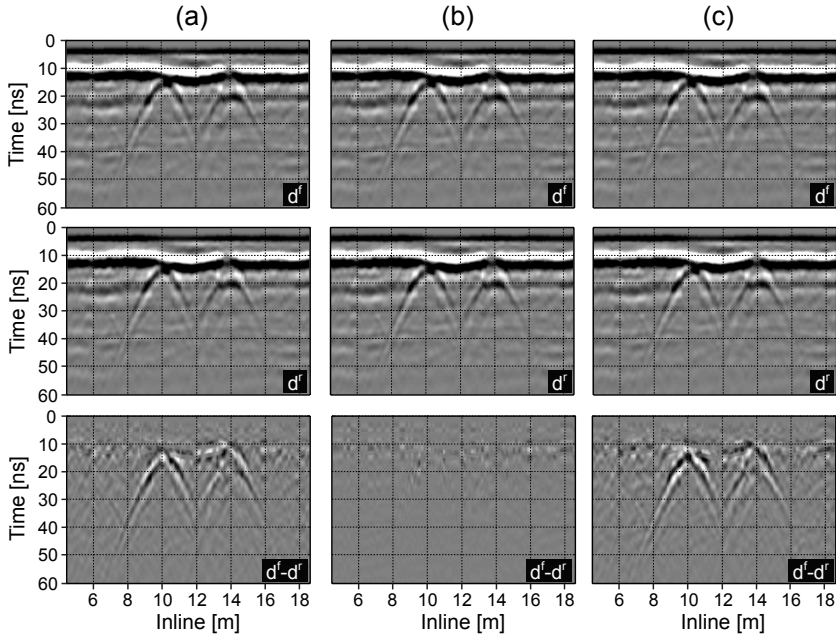


**FIGURE 2.7.** Influence of latency correction on 2D GPR data. Correction of a selected GPR profile pair ( $d^f, d^r$ ) using different latencies of (a) 0 s (uncorrected), (b) 0.42 s ( $l_{Opt}^{MSSIM}$ ), (c) 0.85 s (overcorrected). To highlight the actual differences between the undercorrected, optimal corrected, and overcorrected profiles, the difference ( $d^f - d^r$ ) is shown in the bottom row.

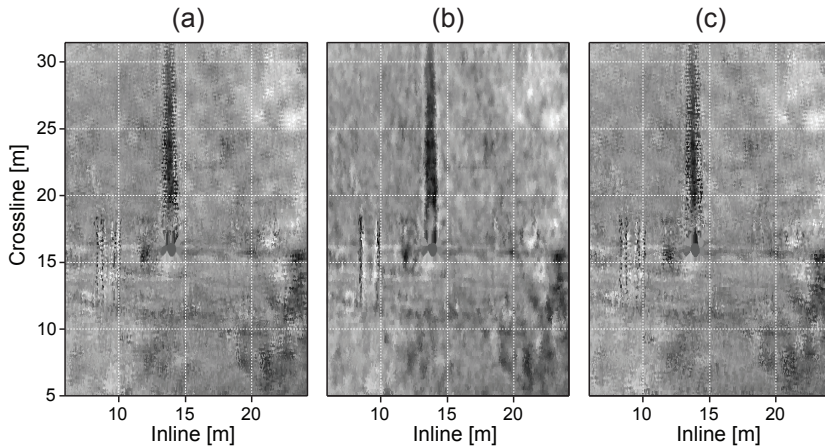


**FIGURE 2.8.** Influence of latency correction on 3D GPR data. Gridded timeslice of a 3D 200 MHz GPR data cube at a field with buried metallic pipes represented by crossline-oriented linear features. Correction of 3D GPR data using different latencies of (a) 0 s (uncorrected), (b) 0.42 s ( $l_{Opt}^{MSSIM}$ ), (c) 0.85 s (overcorrected). Optimal latency correction reduces zigzag patterns and results in aligned reflection anomalies.

## 2.6 Conclusions

We successfully presented how modern TTS systems can be used to kinematically acquire GPR data using off-the-shelf instrumentation and without any hardware modifications. Making use of pseudo-NMEA strings allows to directly merge geophysical data, in general, and GPR data in particular, with the positional information measured by the TTS. Detailed studies about the influences of such an acquisition setup on the GPR data have, to the best of our knowledge, not been presented before.

Our walkaway experiments have shown that GPR data quality is influenced up to distances of  $\sim 4\text{--}6$  m by radio cross-talk which, as expected, is offset dependent and can be effectively controlled via modem gain. Additionally, one might further decrease such cross-talk by using other wireless communication standards (e.g., bluetooth or WLAN).

Furthermore, we successfully demonstrated how latency can be estimated using a simple forward–reverse experimental procedure. From the different fidelity measures used to determine the optimum latency for subsequent correction, the MSSIM has proven to provide the most robust results. For our experimental setup using unshielded 200 MHz antennae, we found a optimum latency of 0.42 s. If not corrected for, such a latency might result in positioning errors of  $\sim 0.2$  m at typical walking speeds, which might be critical, especially, for dense and/or multi–component 3D data sets. For 2D data assuming constant acquisition direction, the positional error introduced by latency might be less evident and critical. Thereby, the need to evaluate and correct for system latency is driven by the individual application and the required positional accuracy. Considering that the actual latency is hardware-setup dependent and that it might potentially vary from setup to setup, we suggest that similar, perhaps less extensive, latency experiment should in our point of view become standard to every kinematic GPR field survey to minimize potential positioning errors. For example, we believe that zigzag patterns also often visible in other near-surface geophysical surveys might be attributed, at least to some extent, to systematic latencies introduced through kinematic positioning solutions. Finally, the presented setup and considerations are not limited to GPR applications, and they can also be adapted to any other kinematic geophysical surveying approach (e.g., magnetics) and other surveying solutions (e.g., GPS).

## 2.7 Acknowledgments

The authors would like to thank the anonymous reviewers for their constructive comments, which significantly improved the quality of this manuscript.

# IMPROVING THE INTERPRETABILITY OF 3D GPR DATA USING TARGET-SPECIFIC ATTRIBUTES: APPLICATION TO TOMB DETECTION

Böniger U., Tronicke, J.

*Journal of Archaeological Science*, 2010, **37** (4), 672–679,

doi:10.1016/j.jas.2010.01.013

Published by Elsevier

---

## 3.1 Abstract

Three-dimensional (3D) ground-penetrating radar (GPR) represents an efficient high-resolution geophysical surveying method allowing to explore archaeological sites in a non-destructive manner. To effectively analyze large 3D GPR data sets, their combination with modern visualization techniques (e.g., 3D isoamplitude displays) has been acknowledged to facilitate interpretation beyond classical time-slice analysis. In this study, we focus on the application of data attributes (namely energy, coherency, and similarity), originally developed for petroleum reservoir related problems addressed by reflection seismology, to emphasize temporal and spatial variations within GPR data cubes. Based on two case studies, we illustrate the potential of such attribute based analyzes towards a more comprehensive 3D GPR data interpretation.

The main goal of both case studies was to localize and potentially characterize tombs inside medieval chapels situated in the state of Brandenburg, Germany. Comparing the calculated data attributes to the conventionally processed data cubes we demonstrate the superior interpretability of the coherency and the similarity attribute for target identification and characterization.

### 3.2 Introduction

The principles of ground-penetrating radar (GPR) are based on the reflection and refraction of electromagnetic (EM) waves at subsurface features characterized by changes in their electrical properties (Daniels, 2004). Given its high spatial resolution and the possibility to retrieve depth-related information, GPR has become a popular geophysical method for non-destructive archaeological exploration (e.g., Goodman and Nishimura, 1993; Gracia et al., 2000; Leucci and Negri, 2006; Francese et al., 2009).

We think that a commonly encountered characteristic of GPR data acquired at archaeological sites is their enhanced complexity compared to other typical applications such as geological investigations. Beside the fundamental target differences (shape and continuity of subsurface structures), this might also be attributed to multiple anthropogenic developments over centuries, resulting in strong subsurface disturbances. Figure 3.1 visualizes this observation by two typical GPR profiles; one acquired in a sand and gravel pit using 100 MHz antennae and the other at an archaeological site using shielded 500 MHz antennae. For a basic geological interpretation primarily fo-

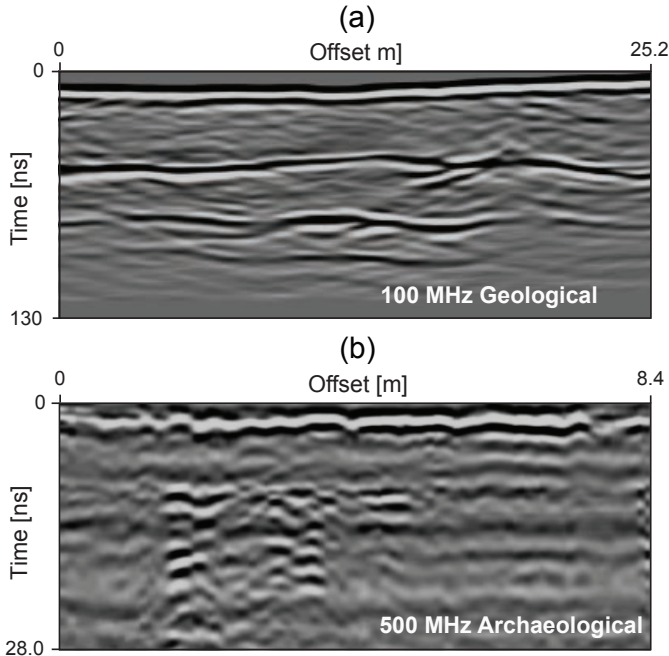


**FIGURE 3.1.** (a) Representative geological 100 MHz GPR data set consisting of several continuous reflectors along the profile. (b) Archaeological 500 MHz profile with a characteristic discontinuous and complex reflection pattern.

cusing on the geometry of subsurface interfaces (i.e., boundary between materials of different composition), a single 2D profile (as shown in Figure 3.1(a)) might already suffice to interpret and understand subsurface architecture. On the other hand, typical archaeological profiles (such as the one shown in Figure 3.1(b)) are characterized by discontinuous and complex reflection patterns with strong amplitude variations, which make the interpretation of individual 2D profiles very difficult or even impossible. Therefore, 3D GPR data acquisition, processing, and interpretation seems to be inevitable to thoroughly interpret and understand complex subsurface structures typically found at archaeological sites.

For a long time, 3D GPR surveying has been considered as being an inefficient surveying technique, mainly due to the enormous field effort when collecting dense 3D data sets using measuring tape or odometer solutions. Driven by recent advances in kinematic positioning solutions, 3D real-time kinematic data acquisition has become an attractive and efficient surveying solution (see Lehmann and Green, 1999; Paoletti et al., 2005; Francese et al., 2009). Most studies have employed global positioning system (GPS) based solutions as for example used by Francese et al. (2009). However, when satellite coverage is poor (e.g., at urban or indoor sites) GPS based surveying solutions might not provide the required accuracy (usually in centimeter-range) or even fail. As applied in this study, modern self-tracking total station (TTS) systems are more than an alternative for 3D GPR data acquisition.

For 3D data sets, modern 3D visualization techniques, like the extraction of isosurfaces (Nuzzo et al., 2002), have been acknowledged for improved data interpretation compared to more traditional techniques such as time-slice analyzes (Goodman and Nishimura, 1993). We believe that attribute based analysis can further improve the quality and efficiency of 3D GPR data interpretation. In this context, we define a data attribute as a specific quantity calculated from the data in order to visually enhance or isolate the features of interest. For decades, such attribute analyzes have been successfully applied to several reservoir related problems faced by the petroleum industry using reflection seismic data (Gersztenkorn and Marfurt, 1999; Chopra and Marfurt, 2007; Liu and Marfurt, 2007). However, the principles of attribute analysis and their application to GPR data are only slowly perceived by the GPR community (Young et al., 1997; Sénéchal et al., 2000; Tronicke et al., 2006; McClymont et al., 2008) and most published GPR attribute studies focused on geological targets similar to the ones encountered in reflection seismics (such as detecting and characterizing faults and bounding surfaces). Given the variety of established attributes (see Chopra and Marfurt, 2007) each addressing a specific problem, we found that the so-called coherency (Bahorich and Farmer, 1995; Young et al., 1997; Marfurt et al., 1998) and similarity (de Rooij and Tingdahl, 2002) attributes, originally developed to highlight discontinuities (such as faults) in seismic data, are extremely feasible for GPR data approaching archaeological targets. More details about these attributes are given be-

low.

In the following, we present two case studies illustrating the potential and usefulness of attribute based GPR processing to highlight typical archaeological targets. After providing information regarding data acquisition, processing, and attribute calculation we illustrate the interpretational gain resulting from the coherency and similarity attributes using two field data sets collected to detect and characterize buried tombs.

### 3.3 Data Acquisition and Standard Processing

Here, we present two 3D GPR data sets recorded inside two medieval chapels with the principle goal to detect and eventually characterize burial sites expected at depths of up to  $\sim 1.0$  m. Both 3D GPR data sets were acquired using a pair of shielded 500 MHz antennae, providing the best compromise between resolution and penetration depth at the two sites. Data were recorded using a sampling interval of 0.1 ns and 16 vertical stacks for each trace. As both sites were indoor, use of a real-time kinematic GPS surveying setup for positioning was not possible. We therefore employed a surveying solution combining a self-tracking total station (TTS) with a standard GPR unit. Figure 3.2 illustrates this setup comprising a TTS for real-time positioning with centimeter-precision and two radio modems for transferring the data in real-time to the GPR control unit. To efficiently acquire the data sets without laying out a survey grid, using for example measuring tapes, we used a GPS repeater to

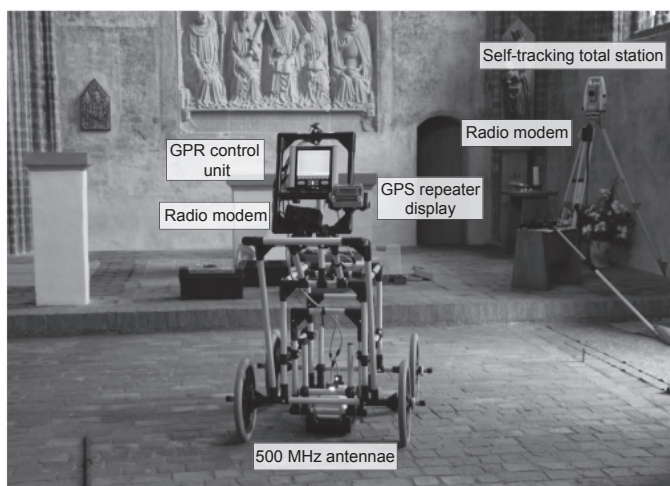


**FIGURE 3.2.** 3D GPR surveying setup: cart-mounted 500 MHz shielded antennae combined with a wireless positioning system using a TTS and a GPS repeater display for navigation.



display coordinates in real-time. Orientation of the local TTS coordinate system was parallel to the in- and crossline direction (using the local resection method) allowing to navigate the acquisition cart along coordinate isochrones. This surveying setup has proven to be extremely flexible and allows for efficient data acquisition at virtually all field settings. For survey site I and II (described in the following section), continuous recording resulted in an inline trace spacing of  $\sim 0.02$  m, using crossline spacings of 0.1 m and 0.05 m, respectively.

GPR data were processed using a standard processing sequence including DC removal and a dewow filter, followed by zero time correction, amplitude scaling, and lowpass filtering. The data were then gridded on a regular grid using a natural neighbor routine. Finally, we migrated both data sets using a 3D Stolt algorithm. Migration velocities were obtained from a combination of common midpoint (CMP) and diffraction analyzes, resulting in constant velocities of 0.115 m/ns and 0.097 m/ns for survey site I and II, respectively.

In order to reduce remaining noise and improve the overall continuity of reflections, we additionally applied a dip-oriented median filter to the migrated data (Young et al., 1997). Selected attributes (energy, coherency, and similarity) were then calculated using the median filtered data cube.

### 3.4 Attribute Analysis

In this section, we briefly introduce the attributes which have proven to provide the best results in this study. Energy is a commonly used attribute in archaeological GPR data sets. It highlights areas characterized by energy changes of the reflected signal. Coherency and similarity on the other hand are used to emphasize the variability of neighboring data and thereby allow to enhance edges along anthropogenic features. For more details (various possibilities of implementation and typical applications to reflection seismic data) we refer to the comprehensive textbook by Chopra and Marfurt (2007) and the additional references given below. Figure 3.3 illustrates the trace notations used in the following.

#### 3.4.1 Energy

The energy attribute is usually used to highlight areas characterized by strong amplitude changes. Signal energy, as used in this study, is mathematically defined as

$$E_{T_{m,n}}(t) = \frac{1}{2N + 1} \cdot \sum_{i=-N}^N T_{m,n}(t + i)^2,$$

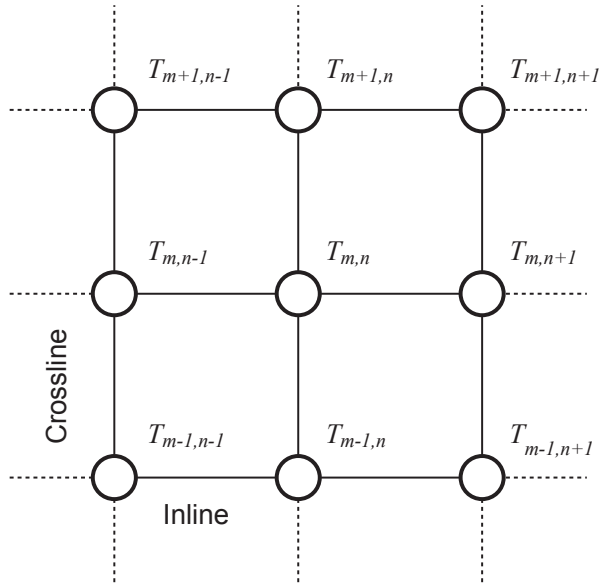


**FIGURE 3.3.** Sketch illustrating a neighborhood of nine individual traces selected from a 3D GPR data set.

where  $E_{T_{m,n}}(t)$  denotes the energy value for a trace ( $T$ ) with crossline position  $m$ , inline position  $n$  calculated at time sample  $t$  using a window length of  $2N + 1$  samples. Evaluation of this equation over all inline, crossline, and time samples of a 3D data set results in a so-called energy cube. Our experience with this attribute shows that the best results are obtained when the time window length corresponds approximately to two wavelengths calculated using the dominant frequency of the data. For both case studies we have chosen a window length of 6 ns using the 500 MHz 3D GPR data.

### 3.4.2 Coherency

Coherency (and also similarity) are multi-trace attributes where the information of neighboring traces is included into the calculation of such attributes. Coherency was originally developed to enhance discontinuities within seismic data sets often related to geological faulting (Bahorich and Farmer, 1995). Coherency ( $\bar{C}_{T_{m,n}}(t)$ ), as used in this study, is calculated by selecting the maximum crosscorrelation between a segment centered around a time sample  $t$  of a trace  $T_{m,n}$ , and segments centered around  $t - \tau_k$  of neighboring traces  $T_{m,n+1}$  and  $T_{m+1,n}$ . For example, crosscorrelation between  $T_{m,n}$  and  $T_{m,n+1}$  is calculated by

$$\begin{aligned}
C_{T_{m,n}, T_{m,n+1}}(t) &= \max_{\tau_k} \left( \sum_{i=-N}^N \{ (T_{m,n}(t + i\Delta t) - \bar{T}_{m,n}(t)) \right. \\
&\times \{ (T_{m,n+1}(t + i\Delta t - \tau_k) - \bar{T}_{m,n+1}(t - \tau_k)) \} \\
&\times \left( \sum_{i=-N}^N \{ (T_{m,n}(t + i\Delta t) - \bar{T}_{m,n}(t)) \}^2 \right. \\
&\times \left. \left. \sum_{i=-N}^N \{ (T_{m,n+1}(t + i\Delta t - \tau_k) - \bar{T}_{m,n+1}(t - \tau_k)) \} \right)^{-1/2} \right),
\end{aligned}$$

where  $\tau_k$  defines discrete time shifts of the selection window for  $T_{m,n+1}$  and  $\bar{T}$  denotes the average calculated over the specified time window.  $C_{T_{m,n}, T_{m+1,n}}$  is calculated in a similar way and then the average coherency  $\bar{C}_{T_{m,n}}(t)$  between the neighbors is calculated by

$$\bar{C}_{T_{m,n}}(t) = \frac{1}{2} \cdot (C_{T_{m,n}, T_{m,n+1}} + C_{T_{m,n}, T_{m+1,n}}).$$

Based on numerous tests the window length was set to 5.8 ns, which provided the best performance for the data sets presented in this study.

### 3.4.3 Similarity

As coherency, similarity is a distance measure quantifying the alikeness of two data vectors. Similarity in its form used here was introduced by de Rooij and Tingdahl (2002) and is calculated, exemplarily along the inline direction by

$$S_{T_{m,n-1}, T_{m,n+1}}(t) = 1 - \frac{\left\{ \sum_{i=-N}^N [(T_{m,n-1}(t + i) - T_{m,n+1}(t + i))]^2 \right\}^{1/2}}{\left\{ \sum_{i=-N}^N T_{m,n-1}(t + i)^2 \right\}^{1/2} + \left\{ \sum_{i=-N}^N T_{m,n+1}(t + i)^2 \right\}^{1/2}},$$

where the average similarity  $\bar{S}_{T_{m,n}}(t)$  between all possible neighbors is calculated by

$$\begin{aligned}
\bar{S}_{T_{m,n}}(t) &= \frac{1}{4} \cdot S_{T_{m,n-1}, T_{m,n+1}}(t) + S_{T_{m+1,n}, T_{m-1,n}}(t) \\
&+ S_{T_{m+1,n-1}, T_{m-1,n+1}}(t) + S_{T_{m-1,n-1}, T_{m+1,n+1}}(t).
\end{aligned}$$

In order to obtain a 3D similarity cube, we calculate  $\overline{S}_{T_{m,n}}(t)$  for all possible in-line, crossline, and time positions. Additionally, to avoid artifacts using horizontally oriented trace segments (Chopra and Marfurt, 2007), the similarity calculation was steered along the local dip information (de Rooij and Tingdahl, 2002). A window length of 5.8 ns is applied to the data sets presented in this study.

## 3.5 Field Sites

The survey sites presented in this study are two medieval chapels located in Brandenburg, Germany. Given historical evidence from the sites, historians expect tombs to be located inside both chapels. For better understanding the history of both chapels and to guide potential future excavations, any information on the location and condition of the tombs are of major interest. Aside from the common conception about the construction of such burials (east–west orientation along the central axis of the nave), no further information was available.

### 3.5.1 Survey site I: Old Chapel Golm

The Old Chapel of Golm was first referenced in 1289 and represents the oldest actively used building in the city of Potsdam, Germany. It is predominantly built from cloister format bricks with embedded cobblestones. In 1718, the chapel has undergone major reconstructions and enlargements resulting in its today's appearance. After the construction of the Kaiser-Friedrich church in the close vicinity, the Old Chapel of Golm was mainly disregarded and served as a burial chapel. Accompanied by the inauguration of the new church (1886) a tombstone showing an effigy of the local aristocratic couple Claus von Schönöw († 1449) and Margarete von Gröben († 1468) was moved to the newly built church. This tomb top represents the only historical evidence indicating that this couple was buried inside the Old chapel. Starting in 2002, an emerging local interest of scientific comprehension and protection of the monument has been observed. In order to complete the understanding of the historical background, the authors were approached to locate the expected burial sites inside the chapel. Figure 3.4(a) shows an outside view of the chapel and Figure 3.4(b) the tomb top with effigy. Its dimensions are annotated in Figure 3.4(b) and will be referenced in the subsequent interpretation. Taking the local geology into account, we expected the subsurface to consist predominantly of sand dominated glacial sediments.

The area surveyed with GPR inside this building measures  $\sim 6 \times 12$  m. Figures 3.5(a)–3.5(c) show three typical shallow time slices ranging from 4 ns ( $\sim 0.23$  m, ground wave) to 12 ns ( $\sim 0.69$  m). Most of the linear features visible in Figure 3.5(a) are highly correlated with variations in the floor tiling. From Figure 3.5(b) and 3.5(c),

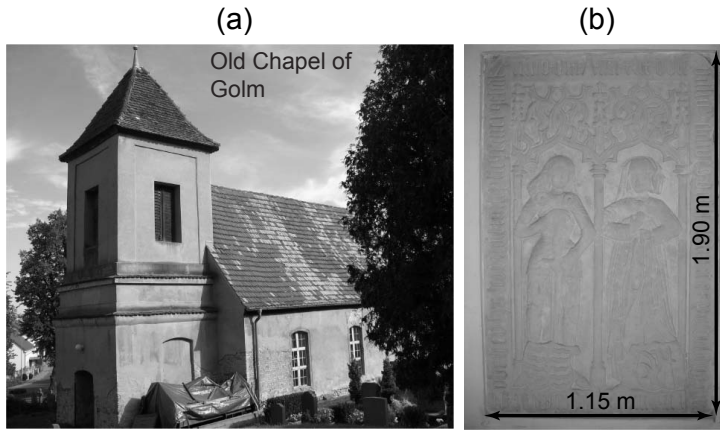


**FIGURE 3.4.** (a) Medieval chapel of Golm, historically referenced for the first time in 1289. (b) Preserved tomb top with an effigy of the aristocratic couple Claus von Schönow and Margarete von Gröben.

the position of two burial sites, located between  $\sim 2$  to  $\sim 5$  m northing and  $\sim 8$  to  $\sim 11$  m easting, is already apparent as almost rectangular high amplitude anomalies. Apart from the actual localization, a more detailed characterization (accurate dimensions, separation, potential damage) of the tombs is rather challenging. To conduct a more detailed interpretation, we calculated the attributes energy, coherency and sim-

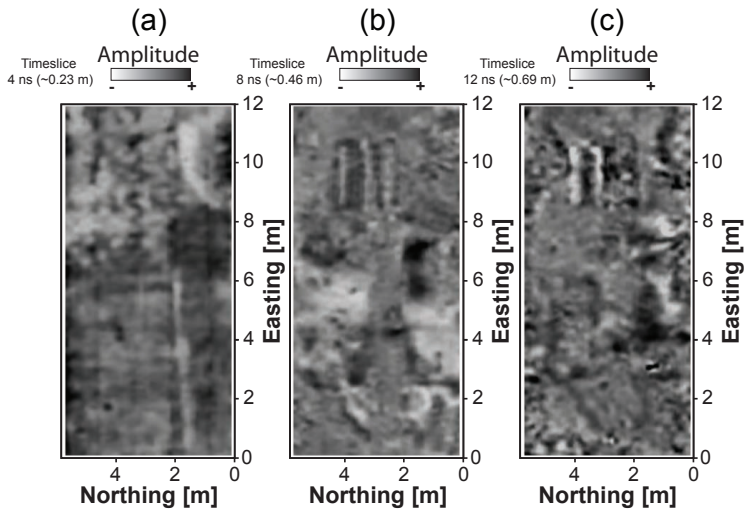


**FIGURE 3.5.** Exemplary time slices through the median-filtered data cube at two-way-travel times (depths) of (a) 4 ns ( $\sim 0.23$  m), (b) 8 ns ( $\sim 0.46$  m), and (c) 12 ns ( $\sim 0.69$  m). Depths were estimated using a velocity of 0.115 m/ns.

ilarity from the dip median filtered data cube (see Figure 3.6). While energy is used to enhance differences in the reflected signal strength (which can often be related to archaeologically relevant features), coherency and similarity highlight discontinuities present in the data. Figure 3.6 shows that energy allows to enhance the left tomb, while the right structure (interpreted as a second tomb) fades due to a lower amplitude contrast to the surrounding material. The success of the energy attribute is related to the assumption that the features of interest respond with significant amplitude changes compared to their surroundings. On the other hand, coherency and similarity (Figures 3.6(c) and 3.6(d)) are both successful in depicting the structural edges of the two objects, allowing for a clear separation and further interpretations. Although the overall appearance is quite similar, coherency seems to result in a more binary image while similarity improves the structural continuity. This observation can be attributed to the additional amplitude sensitivity included in the similarity definition. The intrinsic normalization process when calculating coherency and similarity results in attribute values from 0 to 1 (dissimilar/incoherent and similar/coherent), which further facilitates the calculation of isosurfaces in 3D.

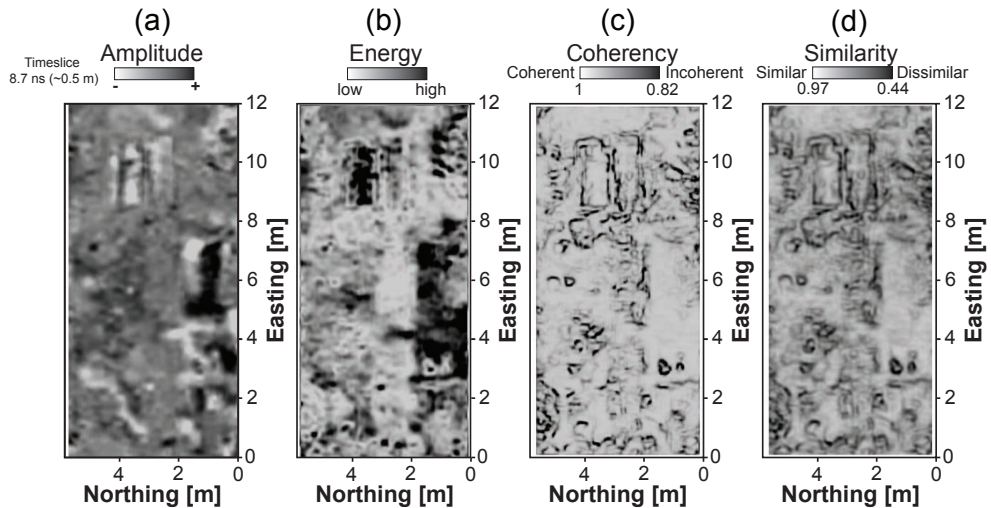


**FIGURE 3.6.** Comparison of a selected time slice at a two-way traveltime of 8.7 ns using (a) dip-median filtered data, (b) energy, (c) coherency, (d) and similarity (for details see text).

The results of these attribute analyzes allow for a more detailed volumetric interpretation (Figure 3.7). Figures 3.7(a)–3.7(d) focus on an estimate of the extension of the tombs and on an interpretation of the characteristics of one side wall indicating some degree of damage. Figure 3.7(a) shows a similarity slice illustrating a discontinuity in one of the side walls of the tomb (indicated by an arrow and a dashed white rectangle). When inspecting two migrated crossline profiles running over this discontinuity

(Figures 3.7(b)–3.7(c)) at  $\sim 9.55$  and  $\sim 9.75$  m easting in detail, it becomes evident that while in Figure 3.7(b) the two top reflections smoothly join, a small horizontal reflector is present in Figure 3.7(c) interpreted as the side wall reflection. Based on a subvolume of the cube, we then calculated an isosurface following constant similarity values (Figure 3.7(d)). 3D rendering allowed to successfully study the size and constitution of the two objects (e.g., the indicated side wall damage) in detail and beyond the possibilities provided by the dip-median filtered or the energy data. A comparison of the dimensions extracted from the 3D volume with the preserved

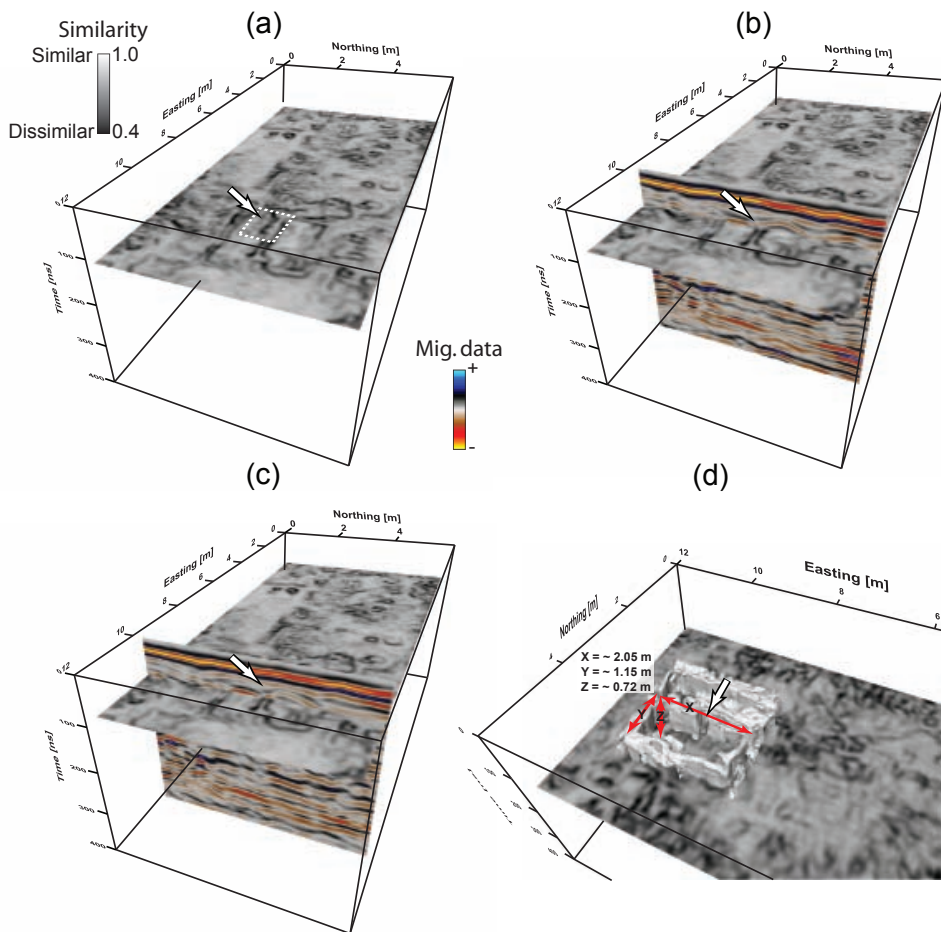


**FIGURE 3.7.** Detailed interpretation based on the similarity data cube. Figure (a)–(c) highlight a subtle feature although visible along in- or crossline slices not visible in migrated timeslices. The arrow indicates the area of special focus, for details see text. Figure (d) shows an isosurface calculated within a subvolume allowing for detailed interpretation.

tomb top (see Figure 3.4) results in a good match.

### 3.5.2 Survey Site II: Chapel Bishops Residence Ziesar

The second survey site is a chapel of the medieval bishops residence Ziesar, Germany (Bergstedt et al., 2009). From the inscription on a wall-recessed votive stone, it is known that bishop Dietrich von Stechow († 1472) inaugurated the chapel in 1470. The building represents one of today's last authentic examples of a late Gothic chapel with a mural covered interior. Throughout time the chapel underwent several reconstructions often accompanied with a change of use. Based on a hand-written note from the early 18<sup>th</sup> century it is known that bishop Dietrich von Stechow himself was buried inside the chapel. The presence of the Calvinists, starting around 1690, had a strong impact on historical evidence. Given the clearing of the chapel from its condemned papacy, this was probably the period when most of the historical evidence about the actual burial site was lost. Starting in 2002, the whole residence has undergone scientific investigations and restorations partially funded by the world monument fund. In order to fully comprehend the relationship between architecture and murals, the viewpoint between votive stone and tomb top, and the forms of religiousness during the time of construction, the exact location of the burial site of the bishop is of major importance. As the chapel is still in sacral use, only a non-invasive investigation as represented by GPR is possible at the site.

Figure 3.8(a) shows an exterior view on the chapel and Figure 3.8(b) illustrates the



**FIGURE 3.8.** (a) Chapel of the medieval bishops residence Ziesar founded in 1470 by bishop Dietrich von Stechow (1459-72). (b) Preserved tomb top with an effigy of the bishop.



preserved tomb top, displayed in a nearby museum. Little was known about the composition of the uppermost layers relevant to the GPR survey. From historical evidence it is known that the chapel was built on and from the remains of numerous previous developments at the site and, therefore, we expected a heterogeneous and complex underground (background material) at this site.

The area surveyed with GPR inside this building measures  $\sim 8 \times \sim 14$  m. Figures 3.9(a)–3.9(c) show three exemplary time slices through the 3D data volume after dip-median filtering. Similar to Figure 3.5, we see the imprint of variations in the floor tiling in the shallowest parts of the GPR data. Compared to the well preserved subsurface architecture at survey site I, all slices illustrate the complexity of subsurface reflection patterns complicating a detailed interpretation.

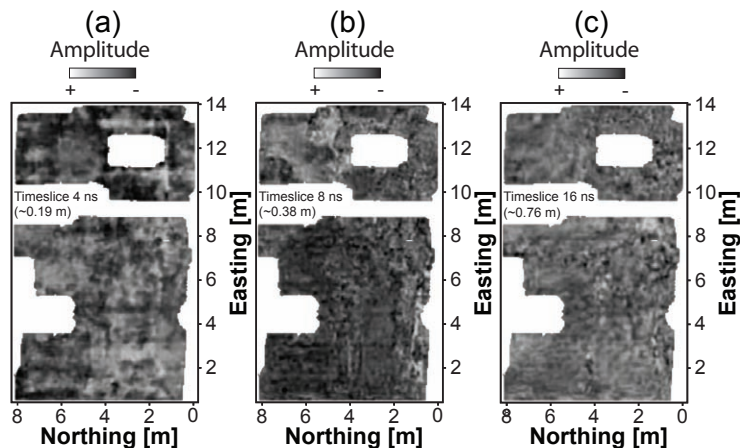


**FIGURE 3.9.** Exemplary time slices through the median-filtered data cube at two-way-travel times (depths) of (a) 4 ns ( $\sim 0.19$  m), (b) 8 ns ( $\sim 0.38$  m), and (c) 16 ns ( $\sim 0.76$  m). Depths were estimated using a velocity of 0.097 m/ns. White areas inside the survey area correspond to regions without data coverage due to obstructions (e.g., altar and columns).

Figure 3.10 shows time slices from dip-median filtered, energy, coherency, and similarity cubes. Comparison of the time slices from Figure 3.10(a) and 3.10(b) shows that the dip-median filtered and energy data indicate no clear rectangular feature, potentially highlighting a burial site. After inspecting the complete data cube, the only possible interpretation is the distinction between highly disturbed areas, characterized by chaotic reflection patterns, and a less disturbed area, characterized by low amplitudes and smoothly varying reflection patterns, located around 2–4 m northing and 4–6 m easting. Figure 3.10(c) and 3.10(d) reveal a rectangular structure similar to the ones from survey site I. Comparison of the spatial extent of this object with the preserved tomb top results in a slightly too small extent along the long axis of the tomb. Nevertheless, the feature shows an east–west orientation and is located cen-

trally inside the nave, indicating that this anomaly could be interpreted as the burial site of bishop Dietrich von Stechow. We believe that this case study is an illustrative example on how attributes can visualize information that is not visible after standard GPR data processing.

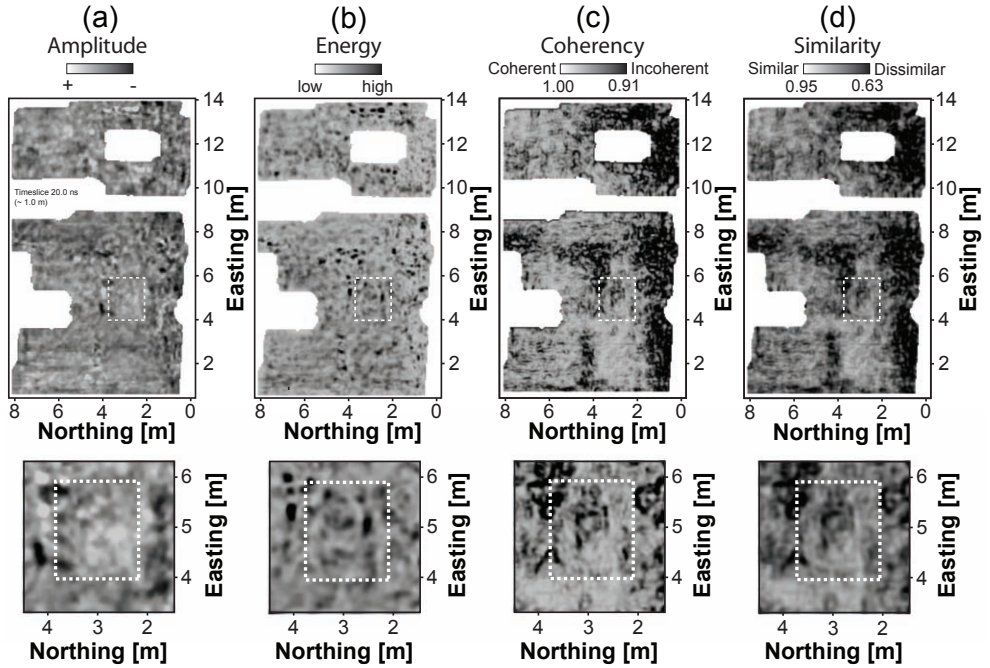


**FIGURE 3.10.** Comparison of a selected time slice after (a) median-filtering, (b) energy, (d) coherency, and (c) similarity calculation. The interpreted location of the tomb is highlighted by a dashed rectangle. The lower row of panels corresponds to zooms around the highlighted areas. In (a) and (b), no obvious structure could be imaged, while both coherency and similarity enhance a rectangular east-west oriented object.

### 3.6 Conclusions

We have shown that systematic 3D GPR attribute analyzes, going beyond standard processing flows, allow for a comprehensive and more detailed interpretation of complex GPR data sets. In particular, coherency and similarity have proven to enhance relevant structural variations based on multi-trace amplitude and waveform variations. Subtle changes in the waveform characteristics are enhanced and result in sharp transitions that allow for an improved target detection (as shown in the second case study) and very detailed structural analyzes (as shown in the first case study). We have experienced that especially the additional sensitivity of the similarity attribute

to amplitude variations is favorable compared to the coherency attribute in order to obtain a more continuous image from archaeological GPR data sets.

In both presented case studies, we have successfully shown an increased interpretability of the data cubes by enhancing subsurface structures using target-specific attributes. We believe that the application of similarity and coherency on dense 3D GPR data sets significantly enhances the foundation of subsequent detailed interpretations. We further believe that target-directed GPR attribute analyzes have a great potential to improve the interpretation of a variety of typical archaeological GPR data sets.

### **3.7 Acknowledgments**

The authors would like to thank dGB Earth Sciences for making their Interpretation Software OpenDTect freely available to academic research. We also want to express our gratitude to H.-G. and H. Löhmannsröben supporting our measurements in Golm and C. Bergstedt from the the museum Ziesar for fruitful collaboration. Additionally, we would like to thank the Deutschen Forschungsgemeinschaft (DFG) for supporting the project TR512/1-2.



# INTEGRATED DATA ANALYSIS AT AN ARCHAEOLOGICAL SITE: A CASE STUDY USING 3D GPR, MAGNETIC, AND HIGH-RESOLUTION TOPOGRAPHIC DATA

**Böniger U.**, Tronicke, J.

*Geophysics*, 2010, **75** (4), B169–B176, doi:10.1190/1.3460432

Published by Society of Exploration Geophysicists

---

## 4.1 Abstract

We have collected magnetic, 3D ground-penetrating radar (GPR), and topographic data at an archaeological site within the Palace Garden of Paretz, Germany. The survey site covers an area of  $\sim 35 \times 40$  m across a hill structure (dips of up to  $\sim 15^\circ$ ) that is partly covered by trees. The primary goal of this study was to detect and locate the remains of ancient architectural elements, which, from historical records, were expected to be buried in the subsurface at this site. To acquire our geophysical data, we used a recently developed surveying approach that combines the magnetic and GPR instrument with a tracking total station (TTS). Besides efficient data acquisition this approach provides positional information at an accuracy within the centimeter range. At the Paretz field site, this information was critical for processing and analyzing our geophysical data (in particular GPR data) and enabled us to generate a high-resolution digital terrain model (DTM) of the surveyed area. Integrated analysis and interpretation based on composite images of the magnetic, 3D GPR, and high-resolution DTM data, as well as selected attributes derived from these data sets allowed us to outline the remains of an artificial grotto and temple. Our work illustrates the benefit of using multiple surveying technologies, analyzing and interpreting the resulting data in an integrated fashion. It further demonstrates how modern surveying solutions allow for efficient, accurate data acquisition even in difficult terrain.

## 4.2 Introduction

For decades, geophysical approaches have been used successfully in archaeological applications to locate and characterize relevant structures buried in the shallow subsurface (Wynn, 1986; Scollar et al., 1990; Jones, 2008). Geophysical mapping techniques such as magnetic surveying are the most popular approaches because they are robust, easy to use, and efficient. Especially across large-scale field sites, these techniques often provide a valuable overview without extensive and time-consuming data processing. Such archaeomagnetic data sets typically are collected using a vertical gradiometer configuration; thus, the analysis and interpretation usually focuses on the vertical gradient of the total magnetic field or of its vertical component (Jones, 2008). In aeromagnetic exploration, the use of data attributes (such as those derived from derivative-based transformations) has proven to allow for a more detailed and accurate interpretation (e.g., Roest et al., 1992; Miller and Singh, 1994; Wijns et al., 2005; Cooper and Cowan, 2006). Although the potential of such attributes has been demonstrated for archaeological targets (e.g., Tabbagh et al., 1997), they are not standard in analyzing archaeomagnetic data (Büyüksarac et al., 2008).

If detailed 3D information on subsurface structures is required, ground-penetrating radar (GPR) is increasingly used because, under favorable site conditions, it provides the highest spatial resolution of any near-surface geophysical technique. Details regarding this technique and its potential in archaeological studies can be found in Jol (2009). However, compared to standard mapping techniques, acquiring, processing, and analyzing 3D GPR data is generally more complex and time-consuming. For example, to obtain accurate 3D subsurface models, a dense data grid with trace coordinates at an accuracy in the centimeter-range is required (Grasmueck et al., 2005). In addition, 3D migration routines have to be used to move dipping reflections to their correct position, unravel crossing events and collapse diffractions (Yilmaz, 2001). Especially when 3D GPR data are collected across topographically rugged terrain (i.e., when local surface gradients are larger than  $\sim 10\%$ ), these points must be considered (Lehmann et al., 2000; Heincke et al., 2005). The interpretation of 3D GPR data usually relies on migrated data volumes. In geological applications, several studies demonstrate the usefulness of attribute-based interpretation (e.g., Tronicke et al., 2006; McClymont et al., 2008). However, GPR data over archaeological targets usually show more complex reflection patterns often hindering a comprehensive interpretation of migrated data volumes. Böniger and Tronicke (2010a) show how target-specific attributes can enhance the interpretability of such 3D archaeological GPR data sets.

In addition to geophysical approaches, the usefulness of microtopographic mapping using differential global positioning systems (GPS) or tracking total stations (TTS) has been demonstrated for archaeological site characterization (Barratt et al., 2000;

Kvamme et al., 2006). The resulting detailed digital terrain model (DTM) allows one to identify subtle variations in surface topography, which might be associated with past anthropogenic activities. However, the required dense grid of accurate topographic data (i.e., with a centimeter accuracy) usually must be acquired as an additional individual survey. Thus, microtopographic surveying is not a standard technique in archaeological site characterization.

The potential of multimethod surveying strategies has also been recognized in archaeological prospecting (e.g., Dabas et al., 2000; Von Der Osten–Wohlenberg, 2005; Drahor, 2006; Kvamme et al., 2006; Keay et al., 2009). Comparable to other near-surface geophysical applications, as in hydrology (e.g., Hyndmann and Tronicke, 2005), collecting multiple geophysical data sets across the same archaeological site offers the opportunity to reduce uncertainties and ambiguities in data analysis and interpretation. However, because all data sets are usually collected individually and efficient, easy-to-use, and easy-to-implement hardware solutions for archaeogeophysical surveying have only recently been introduced (e.g., Hill et al., 2004; Gaffney et al., 2008), most published case studies rely on a single data set. In addition, if several data sets are available, the results are typically presented and analyzed individually; it is not common practice to visualize and interpret an archaeogeophysical database in an integrated fashion. Only few attempts to perform an integrative analysis and interpretation have been published (Piro et al., 2000; Kvamme et al., 2006; Keay et al., 2009).

In this case study, we use a recently introduced TTS-based geophysical surveying approach to acquire magnetic and 3D GPR data accurately and efficiently across an artificial hill structure (with topographic dips of up to  $\sim 15^\circ$ ) in the Palace Garden of Paretz, Germany. After introducing the field site including the archaeological targets, we discuss our data acquisition, processing, and analysis schemes. Using target-specific data attributes and composite imaging approaches, we demonstrate the benefit of a high-resolution, multi-attribute database derived from magnetic, GPR, and detailed topographic data. Finally, we interpret our results in an integrated fashion and illustrate how such a database in combination with historical evidence can be used for a detailed archaeological site characterization.

### 4.3 Field Site

The village of Paretz is located approximately 20 km northwest of Potsdam, the capital of the state of Brandenburg, Germany. The Paretz Palace, including the surrounding village, was built from 1797 to 1804 as a summer residence for the Prussian crown prince, Friedrich Wilhelm, and his wife Luise. Paretz is one of the most significant documentary evidences of Prussian bucolic architecture around 1800. South of the

palace, the actual palace garden is located. From historical documents, it is known that the original architecture of the garden was typical for this time and included several different architectural elements, such as small buildings, grottos, ponds, moats, and bridges. After 1900, much of the original gardening and landscape architecture was destroyed. Currently, the Prussian Palaces and Gardens Foundation Berlin-Brandenburg (SPSG), which manages the Palace complex including the garden, is discussing to what extent the original garden architecture may be reconstructed. To evaluate the site and the buried remains of architectural elements using geophysical techniques, a cooperation between the SPSG and Potsdam University has been established.

In this study, we focus on a  $\sim 35 \times \sim 40$  m area located in the southeastern part of the garden, where a noticeable hill structure is located (Figure 4.1(a)). The hill is grassland, partly covered and surrounded by bushes and trees (Figure 4.1(b)); it shows a maximum elevation of  $\sim 4$  m compared to its surroundings. Surface dips across this structure are up to  $\sim 15^\circ$ . Historical sources provide evidence that the hill is a man-made structure belonging to the original garden architecture. Furthermore, it is known that a replica of a Chinese teahouse built over an artificial grotto and a small temple were located in this part of the garden. During the past 100 years, these buildings were destroyed; today, there is no evidence of their exact location. To locate and characterize the buried remains of these buildings, magnetic, 3D GPR, and topographic data have been acquired using a TTS-based surveying approach.

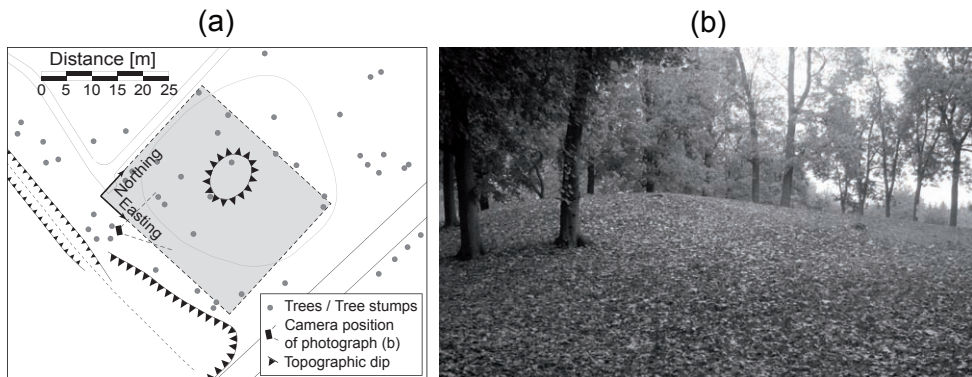


**FIGURE 4.1.** (a) Overview sketch of the study site in the Palace Garden of Paretz, Germany. The shaded rectangle outlines the area surveyed with magnetic and GPR techniques using a TTS-based surveying approach. Arrows indicate the orientation of the local coordinate system, filled gray circles represent trees, and solid triangles indicate topographic dip (b) Photograph of the study site illustrating field site conditions. The camera position and the view angle of this photo are indicated in (a).



## 4.4 Data Acquisition and Processing

### 4.4.1 Acquisition

Because our field site is partly covered and surrounded by trees (Figure 4.1), GPS-based geophysical surveying approaches would be unable to provide the required centimeter-range positioning accuracy. Thus, we collected magnetic and 3D GPR data using a recently introduced TTS-based surveying approach (Figure 4.2; Böniger and Tronicke, 2010a). In this approach, a tripod-mounted TTS (Leica TPS1200 system) automatically tracks a prism mounted on a surveying platform (cart or sledge). While the platform is moving, the TTS automatically measures the position of the prism at a sampling frequency of up to 10 Hz. Data exchange between the TTS and the geophysical instrument is established using two gain-variable radio modems. At the control unit of the geophysical instrument, TTS-generated NMEA strings [i.e., data in standardized GPS format defined by the National Marine Electronics Association (NMEA)] are handled as usual GPS coordinate strings, i.e., they are merged with the geophysical data during data acquisition.

To ensure equally dense data coverage, we use the local resection method to establish a local coordinate system. This well-known technique from engineering surveying establishes the coordinates of points by observations to or from known points (Schoefield and Breach, 2007). In our case, application of the local resection is based on two points located along the user-defined inline orientation of the survey grid. Furthermore, we use a GPS repeater display to navigate along coordinate isochrones.

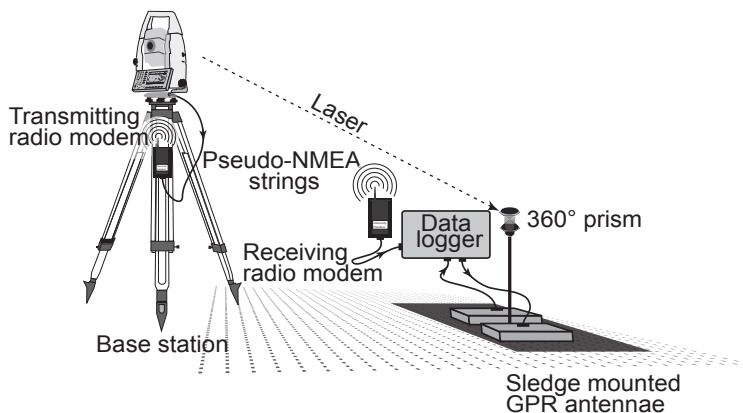


**FIGURE 4.2.** Sketch of the acquisition setup. A static base station (TTS) is combined with a geophysical instrument mounted on a moving surveying platform. Arrows along the cable connections indicate data-flow directions. For details, see text.

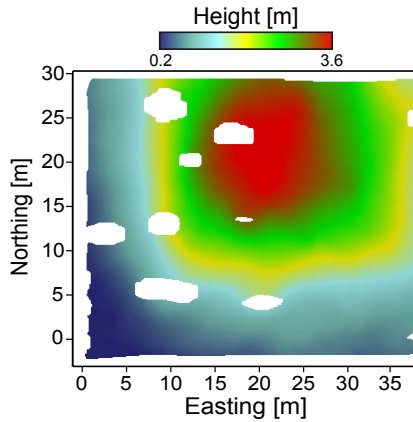
With this procedure other guidelines for orientation (e.g., measuring tape) are dispensable. Further technical details and applications of our surveying approach are given in Böniger and Tronicke (2010a) and Böniger and Tronicke (2010b).

Magnetic and GPR data were acquired separately along approximately parallel lines using a line spacing of  $\sim 0.25$  m. Acquisition with slow to moderate walking speed and continuously recording at the maximum sampling frequency of each geophysical instrument resulted in a mean inline data-point spacing of  $\sim 0.05$  m for both data sets. The magnetic data (total field strength of the earth's magnetic field) were recorded with a cesium optically pumped magnetometer system (Geometrics G-858G) using two sensors with a vertical spacing of 1 m (vertical gradiometer configuration). The 3D GPR data were collected using a pulseEKKO PRO® system (Sensors and Software Inc.) with a pair of unshielded 200-MHz antennae in common-offset mode using an antennae spacing of 1 m.

#### 4.4.2 Standard Processing

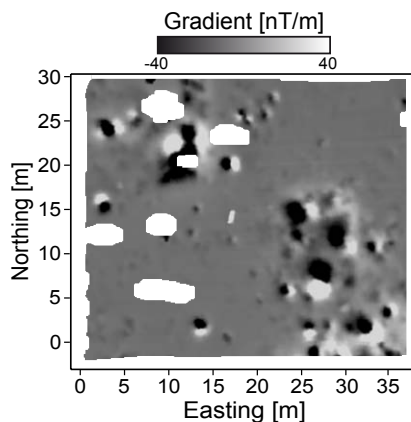
To account for the prism height and the mast inclination of the surveying platforms, we applied a pole-correction algorithm (Lehmann and Green, 1999) to the magnetic and GPR data sets. Additionally, we corrected the data sets for transmission latencies (see Bouvet and Garcia, 2000) i.e., the time delay between the positional measurement and its availability to the geophysical instrument. Such latencies are inherent to all real-time kinematic applications, and their magnitude can be quantified through specially designed experiments based on multiple bidirectional (forward and reverse) data acquisition over the same profile. Using such bidirectional data sets, one can evaluate the temporal delay (latency) between the positioning and the geophysical data; the forward and reverse profiles show a positional displacement if no latency correction is applied. Correcting the positional information for each measurement is based on assigning the interpolated position measured at the time of the geophysical measurement minus latency. By gridding the data sets using different latencies followed by evaluating a fidelity measure (e.g., mean squared error or correlation coefficient) between the forward and reverse profiles it is possible to define the optimum latency to correct for.

After these pre-processing steps, we obtain a detailed local DTM from each survey. Figure 4.3 illustrates the DTM generated by gridding the positioning data of our 3D GPR data set to a  $0.125 \times 0.125$  m regular grid using a natural neighbor-based gridding algorithm (Watson, 1992). White areas in this model (and in all following illustrations) correspond to data gaps due to trees, tree stumps, or bushes. Processing of the magnetic data consisted of natural neighbor-based gridding of the two sensor data sets with an in- and crossline bin size of 0.125 m. After gridding, we applied a



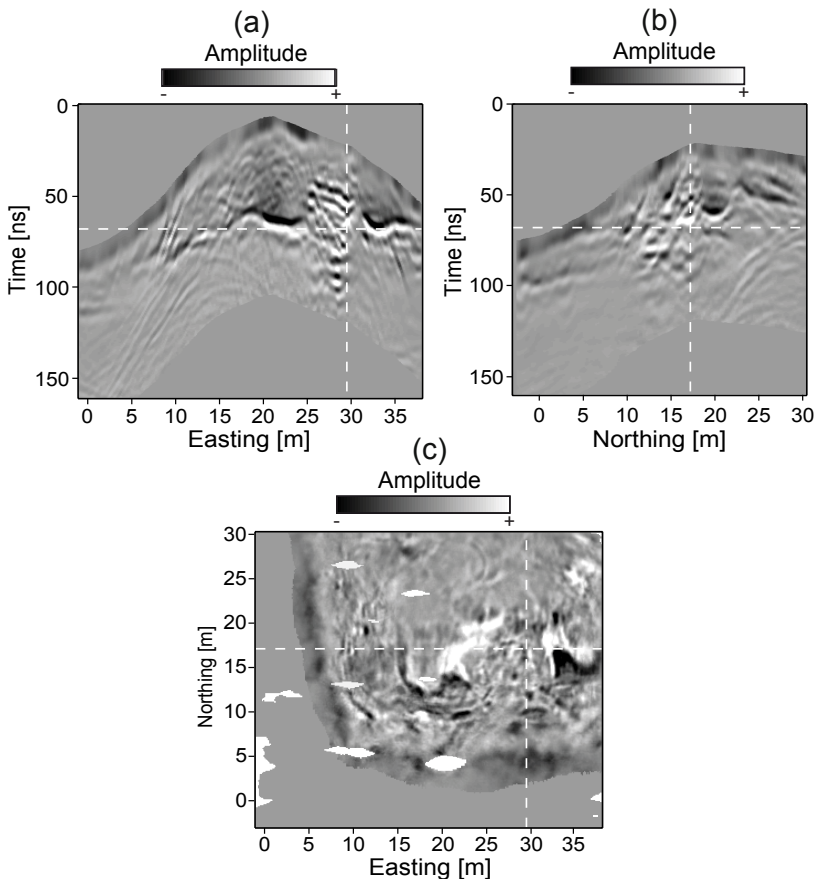
**FIGURE 4.3.** DTM acquired kinematically during magnetic data collection. Color coding indicates the height above 0/0 defining the origin of the local coordinate system. Positional gaps refer to inaccessible survey locations resulting from physical obstructions such as trees and bushes.

spatial filter (2D Wiener) to remove high-frequency spatial noise from the data. Figure 4.4 illustrates our magnetic data set in terms of the vertical gradient. GPR data processing included dewow filtering, band-pass filtering, amplitude scaling (based on division by a time and spatially smoothed amplitude envelope), natural neighbors-based gridding ( $0.125 \times 0.125$  m grid), topographic migration (Lehmann et al., 2000), and static corrections. For migration and static corrections, the high-resolution DTM (Figure 4.4) is critical to image subsurface structures in this environment accurately.



**FIGURE 4.4.** Gridded magnetic gradient map. The data are clipped between  $\pm 40$  nT/m to emphasize the features of interest.

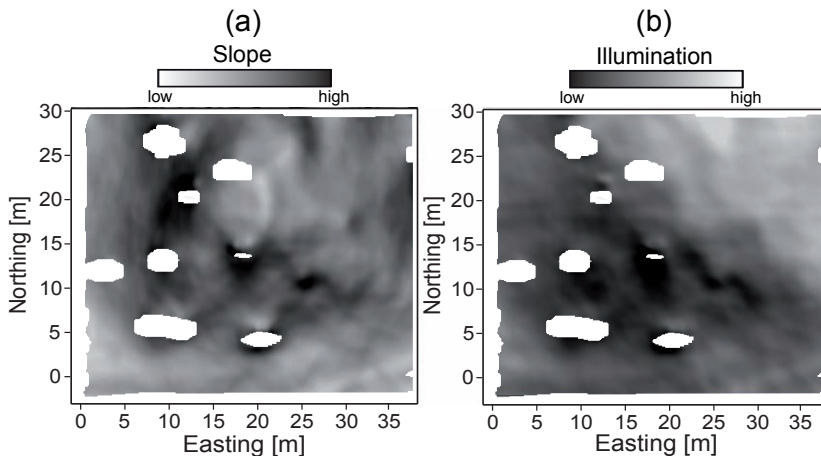
Subsurface velocities were estimated using a combination of common-midpoint measurement analysis and matching diffraction hyperbolas in common-offset sections. Only minor subsurface velocity variations were detected; as such, a constant velocity of 0.09 m/ns for processing the common-offset data was used. Figure 4.5 illustrates the resulting 3D data cube in terms of a typical inline, crossline, and time slice. The strong topographic variations (up to  $\sim 4$  m) of the study site are evident in Figure 4.5(a) and 4.5(b).



**FIGURE 4.5.** Typical (a) inline (17.125 m northing), (b) crossline (29.500 m easting), and (c) time slice (67.8 ns) through our migrated GPR data cube. Dashed white lines indicate the positions of the two intersecting slices. Assuming a constant velocity of 0.09 m/ns, a two-way travelttime of 150 ns corresponds to a depth of 6.75 m.

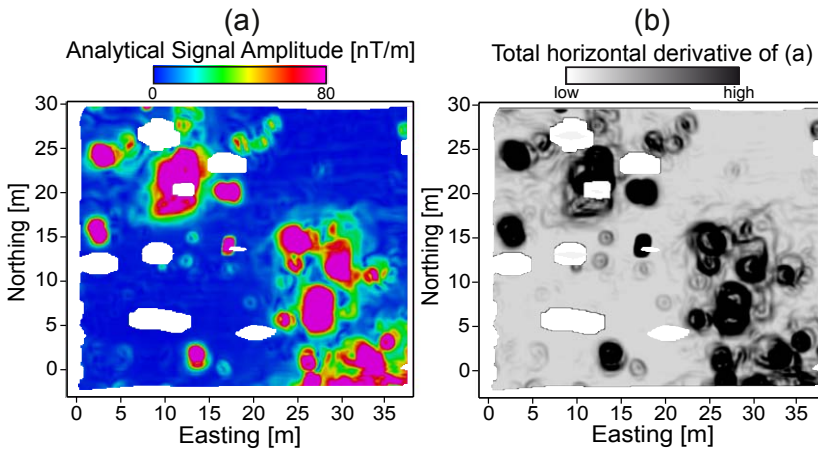
### 4.4.3 Attribute Analysis

From the topographic, magnetic, and GPR data, we calculated various data attributes to visually enhance or isolate the features of interest and thus ease the interpretation. To highlight minor variations within our DTM (Figure 4.3), we calculated the topographic slope from the directional derivatives of the topographic surface (Wilson and Gallant, 2000). Furthermore, we analyzed the data using a hill-shading algorithm (Burrough and McDonnell, 1998). The resulting attributes are shown in Figure 4.6 and provide further insights into the detailed topographical data set. The asymmetric dipole character of magnetic anomalies in mid-latitude regions complicates the interpretation of magnetic maps — for example to outline the locations and edges of buried magnetic sources. Analyses based on the magnetic analytical signal amplitude have helped overcome some of these problems, facilitating interpretation. Here, we use the absolute value of the analytic signal, which is defined as the square root of the squared sum of the vertical and the two horizontal derivatives of the magnetic field (Roest et al., 1992). The advantage of using the analytical signal is that its shape is independent of the earth's magnetic-field parameters and of the direction of magnetization of the source material. To enhance the edges of magnetic anomalies, we calculate the horizontal derivative of the analytical signal, which we define as the square root of the squared sum of the two horizontal derivatives.



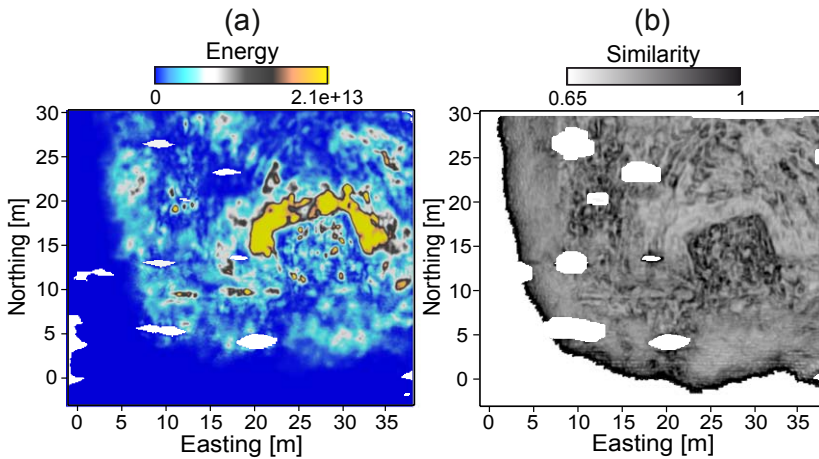
**FIGURE 4.6.** Topographic attributes derived from the DTM shown in Figure 4.3. (a) Slope and (b) DTM processed using hill shading with an azimuth of  $60^\circ$ .

Figure 4.7 illustrates the resulting attribute maps for our magnetic data. GPR data over archaeological targets usually show complex reflection patterns often complicating a comprehensive interpretation. Böniger and Tronicke (2010a) show how target-specific attributes enhance the interpretability of such 3D GPR data sets. Here, we found energy and similarity to be extremely useful in delineating the target features. Energy is a common attribute in archaeological prospecting using GPR and is de-



**FIGURE 4.7.** Attributes derived from the magnetic data set illustrated in Figure 4.4 as vertical gradient. (a) Absolute value of the analytic signal and (b) total horizontal derivative calculated from (a).

defined as the averaged sum of squared amplitudes over a specified time window. It highlights high-energy areas in the reflected signals, which are often associated with archaeological targets such as wall or foundation remains. Similarity, on the other hand, emphasizes the variability within a data cube i.e., it can be used for edge detection. It is a distance measure quantifying the likeness of two data vectors using a specified window length, usually averaged over all neighboring vector pairs around the sample to be evaluated (de Rooij and Tingdahl, 2002). Based on the success of the energy attribute at this site, we found that subtle features can be further enhanced by reflection strength, a classical seismic attribute (Chopra and Marfurt, 2007). Thus, calculating similarity on reflection strength sharpens the image. Typical slices from the calculated energy and similarity cubes are shown in Figure 4.8.



**FIGURE 4.8.** GPR attributes derived from the migrated data cube illustrated in Figure 4.5. (a) GPR energy; (b) similarity on reflection strength.

#### 4.4.4 Composite Imaging

To analyze our multi-attribute database efficiently, we created composite images using visualization techniques also known as color stacking, red-green-blue (RGB) blending, or pseudo-color coding. These approaches are well established in the remote-sensing and digital image processing communities (e.g., Pohl and van Genderen, 1998) and have also been used successfully to analyze multimethod or multiattribute geophysical sets (e.g., Guo et al., 2008; Keay et al., 2009). Using the RGB color model, three co-located data sets can be combined into one pseudo-color image by assigning each data set to one of the color channels. Adding an alpha (transparency) channel defines the RGBA model and allows one to include a fourth dimension (data set).

Modern computer visualizations techniques such as those implemented in many geophysical analysis and interpretation software packages use this idea to generate composite images of multiple data sets and attributes. Our experience shows that composite images are extremely helpful to analyze and interpret the results of multimethod near-surface geophysical surveys because they represent a simple but efficient method in order to evaluate a database consisting of several data sets. The common approach is to compare different data sets or models side by side. This approach is rather cumbersome, difficult, and highly subjective. Composite imaging attempts to ease the interpretation and reduce subjectivity. For example, combining magnetic anomaly maps with individual GPR time slices into several composite images allows one to estimate the source depth of magnetic anomalies because color mixing indicates concurrent magnetic and GPR anomalies. Two examples created in this study from our

multimethod/multiattribute database are illustrated in Figure 4.9.

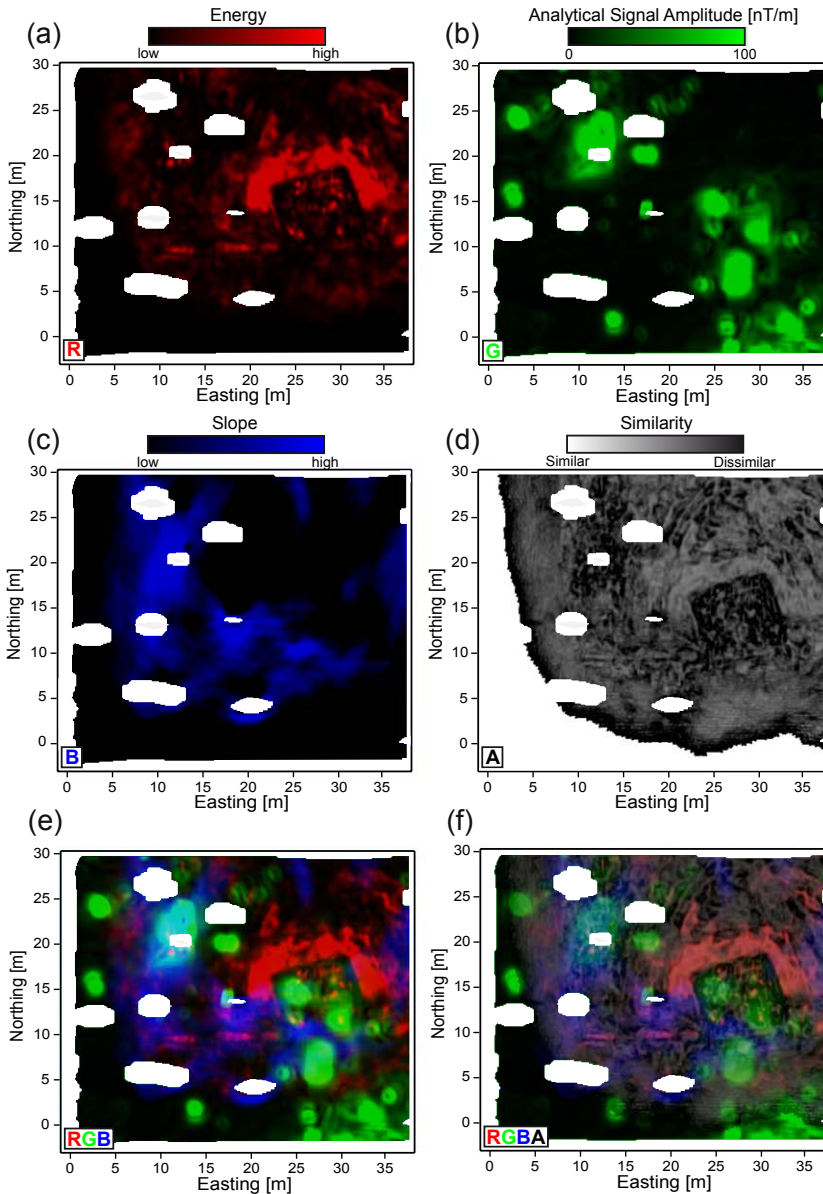


**FIGURE 4.9.** Examples of composite images using (a) GPR energy (red channel), (b) analytical signal (green channel), (c) topographic slope (blue channel), and (d) similarity (alpha channel). (e) Composite image generated from (a)–(c) using the RGB model. (f) Composite image generated from (a)–(d) using the RGBA model.



## 4.5 Results

The DTM (Figure 4.3), the magnetic data set (Figure 4.4), and the 3D GPR data cube (Figure 4.5) build the database for the following analyses and interpretation. Figure 4.3 clearly depicts the hill structure and illustrates maximum topographic variations of  $\sim 4$  m. Analyzing this model in more detail shows that local dips partly exceed  $10^\circ$ , with maximum values of more than  $15^\circ$ . To highlight variations within the DTM, we calculate the slope as shown in Figure 4.6(a). East and south of the flat hilltop (located around 20 m northing and 20 m easting), distinct anomalies characterized by high slopes (black) are visible. To highlight more subtle features in our DTM, we applied a hill-shading algorithm evaluated with different lightening scenarios. The example in Figure 4.6(b) provides further insight into our topographic data. For example, around 10–15 m northing and 25–30 m easting, some linear features almost perpendicular to each other are emphasized. These lineaments outline the boundaries of a relatively flat area (see also Figure 4.6(a)).

In the magnetic gradient map (Figure 4.4) and even more clearly in the analytical signal (Figure 4.7(a)), several distinct anomalies are visible. Aside from isolated dipole-shaped anomalies (most likely from shallow metallic objects), the two most prominent anomalous areas are located around 10–15 m northing and 25–30 m easting, and around 20–25 m northing and 10–15 m easting, respectively. These areas outline approximately rectangular anomaly patterns and thus might be the actual target anomalies.

The processed GPR data (Figure 4.5) provide further details and depth-related information on subsurface structures. Remaining diffraction hyperbolae originate from above-surface scatterers (e.g., trees). The continuous sub-horizontal reflection around 70 ns (clearly visible in Figure 4.5(a)) can be interpreted as the ground surface before the artificial hill structure has been heaped up. This interpretation is based on the observation that this reflector is approximately at the same elevation as the current surface topography outside the artificial hill structure. In addition, Figure 4.5(a) shows a distinct and complicated reflection pattern at  $\sim 25$ – $\sim 30$  m easting and between  $\sim 40$  and  $\sim 100$  ns. Time slices through the migrated data volume further help to reveal the structure of these anomalous reflection patterns (Figure 4.5(c)). However, when comparing Figure 4.5(c) with the calculated attribute slices (Figure 4.8), it is evident that these attributes significantly highlight the features of interest. For example, the complicated reflection pattern at  $\sim 25$ – $\sim 30$  m easting (Figure 4.5(a)) is associated with high energy values (Figure 4.8(a)) but the boundaries of this feature are clearly depicted by similarity (Figure 4.8(b)). To analyze our results in more detail and to ease an integrated interpretation, we generate several composite images.

## 4.6 Interpretation

Our interpretation is based on integrated visualizations of the processed data sets. Figure 4.9 presents two examples of composite images. In the first example (Figure 4.9(e)), we combine a GPR energy slice (Figure 4.9(a); red channel), the analytical signal (Figure 4.9(b); green channel), and the topographic slope (Figure 4.9(c); blue channel) to an RGB composite image. This image illustrates the complementary nature of the different data sets, because it is dominated by the primary colors: red, green, and blue. In some areas, color mixing occurs, which indicates the corresponding anomalies are detected by more than one data set. For example, violet denotes areas of coinciding GPR energy and topographic slope anomalies, but light blue highlights anomalies characterized by increased analytical signal amplitudes and increased topographic slope values. In Figure 4.9(f), we use the RGBA model and add the GPR similarity attribute (Figure 4.9(d)) as a transparency channel to Figure 4.9(e). As this attribute highlights subsurface discontinuities, it adds structural detail and further sharpens the composite image. Such composite images are then used for the final interpretation of our database, including a comparison to an available historical map of the garden.

Figure 4.10(a) illustrates an historic sketch (originally not to scale) of the surveyed area drawn by Rabe (1811). This sketch has been scaled and rotated to match the actual site dimensions. In Figure 4.10(b), we show the same sketch with the major anomalies (A–E) interpreted from the composite images (see Figures 4.9, 4.10(c), and 4.10(d)). Area A with its rectangular shape is the most prominent anomaly in all of our data. Although high GPR energy (red) and topographic slope values (blue) outline the boundaries of this feature, its inner part is characterized by complex magnetic anomalies (green channel). Including the GPR similarity as alpha (transparency) channel further sharpens the rectangular shape of area A while highlighting the complexity of the inner part. Considering the historical map, we interpret area A as the remains of an artificial grotto originally built underneath a teahouse. Because this structure is sharply outlined by our data, we conclude that the buried walls are well preserved. The complex magnetic and similarity signatures inside area A suggest that the interior of the grotto consists mainly of demolition rubble, possibly from the remains of the teahouse.

Area B is characterized by similar anomaly patterns in the analytical signal (green channel) and the topographic slope (blue channel). The GPR similarity attribute (transparency channel) illustrates that GPR reflection patterns in this area are highly dissimilar, whereas the GPR energy attribute (red channel) shows only minor variations. Considering the available historical sources, we interpret B as the remains of a small temple built from a vertical brick wall with its entrance located at  $\sim 20$  m northing and  $\sim 5$  m easting. The anomalies associated with this structure show a

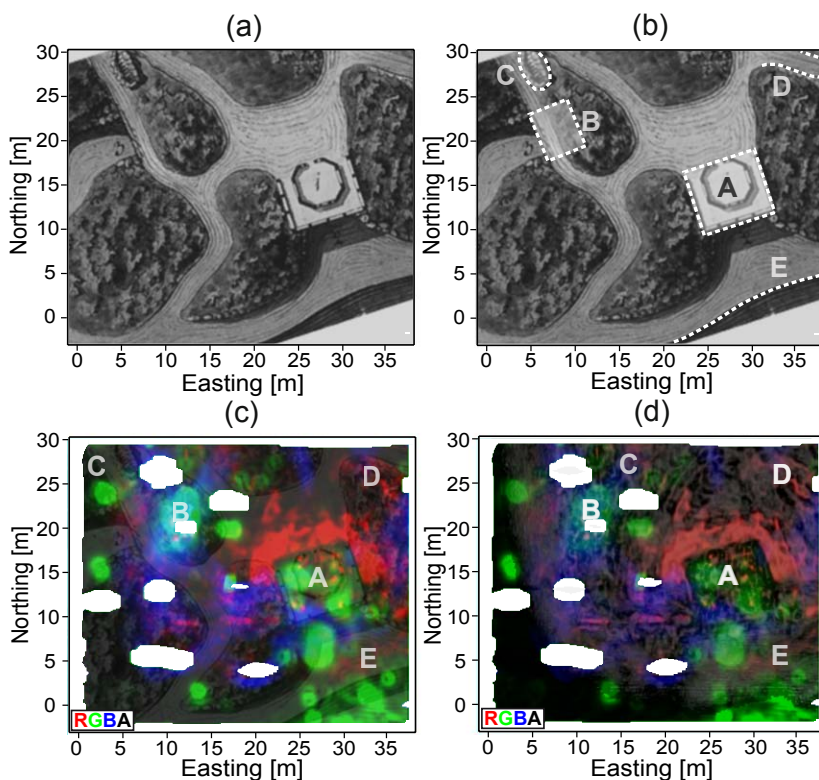


**FIGURE 4.10.** Interpretation of composite images. (a) Historical sketch (originally not to scale) of the surveyed area drawn by Rabe (1811). (b) The same as (a) but including major interpreted anomalies labeled A–E and further highlighted by dashed lines. (c) Composite image generated from Figure 4.9(a)–4.9(c) and (a) using the RGBA model. Labels A–E identify major anomalies. (d) Same as Figure 4.9(f) but including major interpreted anomalies, labeled A–E.

diffuse and chaotic character, which might indicate an accumulation of rubble and metallic objects. Comparing Figure 4.10(b) and our database in more detail, we see a disparity between the temple’s orientation and the location. From the historical map, a northwest–southeast orientation of the temple is expected; however our interpretation results indicate a north–south orientation (Figure 4.10(c); also Figures 4.6(a), 4.7(a), and 4.7(b)).

Further anomalies can be interpreted from our database. For example, from the historical map we expect a staircase northwest of the temple (C in Figure 4.10(b)). Our interpretation shows no significant anomalies in this area; however, especially in the similarity slice, we see a rectangular pattern (C)  $\sim 5$  m to the east. Taking the original attribute maps (Figures 4.6–4.8) into account, we deduce this structure is more or less

sharply imaged by all attributes and thus we have confidence in interpreting it as the remains of the staircase connecting the temple with the upper level of the hill.

Another example illustrating the potential of such composite images are areas (D) and (E) in Figure 4.10. The anomalies associated with D (mainly lineaments in GPR energy and similarity) seem to be linked to a former footpath. Area E, located in the southeast corner of our site, is characterized by rather strong magnetic anomalies. Figure 4.10(b) illustrates that originally a moat was located in this area; thus, we interpret the magnetic anomalies associated with E as a landfill.

## 4.7 Conclusions

In this case study, we have presented the results of an integrative analysis and interpretation of three different data sets: magnetic vertical gradiometer, 3D GPR, and topographic. Combining the geophysical instruments with a modern TTS allowed for efficient geophysical surveying with high positional accuracy at a field site characterized by strong topographic variations. Aside from standard processing, we calculated specific attributes enhancing the interpretability of each data set. We have shown how a combination of multiple attributes into composite images can further ease and corroborate the interpretation of a multimethod/multiattribute database. In addition, we have revealed the complementary nature of our database by composite image analysis. The results of this study will be used to develop excavation and eventual restoration plans for the surveyed part of the Palace Garden of Paretz, Germany. Our study shows the benefit of acquiring and interpreting multiple data sets in archaeological prospecting. Given the technical developments toward efficient near-surface geophysical data acquisition approaches (e.g., multi-sensor platforms using GPS or TTS positioning systems), we believe there will be an increasing need for powerful time- and cost-effective approaches for an integrative analysis of multiple data sets. In addition to archaeological studies, such approaches can assist a variety of applications, e.g., from environmental and engineering geophysics.

## 4.8 Acknowledgments

The German Research Foundation (DFG) supported this research under grant TR 512/2-1. We thank the Prussian Palaces and Gardens Foundation (SPSG) for allowing us to acquire and publish the presented field study. The Applied and Environmental Geophysics group at ETH Zürich providing us their topographic migration algorithm. For analyzing the 3D GPR data and visualizing our database, we used OpendTect. We thank dGB Earth Sciences for making this software freely available for university research and education.

# SUBSURFACE UTILITY EXTRACTION AND CHARACTERIZATION: COMBINING GPR SYMMETRY AND PCA POLARIZATION ATTRIBUTES

Böniger U., Tronicke, J.

submitted to *IEEE Transactions on Geoscience and Remote Sensing* (2010)

---

## 5.1 Abstract

Polarization of the electromagnetic wavefield has significant implications for the acquisition and interpretation of GPR data. Based on the geometrical and physical properties of the subsurface scatterer and the physical properties of its host material, strong polarization phenomena might occur. We developed an attribute-based analysis approach to extract and characterize buried utility pipes using two broadside antenna configurations.

First, we enhance and extract the utilities by making use of their distinct symmetric nature through the application of a symmetry enhancing image processing algorithm known as phase symmetry. Second, we perform a physical characterization of the target features by calculating two polarization attributes (polarization angle and linearity) using principle component analysis. Combination of attributes derived from these steps into a novel depolarization attribute allows to efficiently detect and characterize utilities within 3D GPR data. The performance of our analysis approach is illustrated using synthetic examples and evaluated using field examples (including a dual-component 3D data set) collected across a field site, where detailed ground-truth information is available. Our results demonstrate that the proposed approach allows for extraction and combination of utility relevant information and thus, eases the interpretation of multi-component GPR data sets.

## 5.2 Introduction

In a variety of archaeological, environmental, engineering, and geological problems, ground-penetrating radar (GPR) has become a popular geophysical technique to study the shallow subsurface, mainly thanks to its high-resolution imaging capabilities (e.g., Daniels, 2004; Jol, 2009). Usually, the interpretation of two- and three-dimensional (2D and 3D) GPR data sets is limited to a pure structural interpretation by, for example, tracking coherent reflection events from subsurface horizons or picking diffraction hyperbolas caused by isolated objects and other discontinuities. Such a strategy focusing on target detection and depth determination may be sufficient for some applications; however, it largely ignores the vectorial nature of the GPR wavefield, which can be used to further characterize the buried targets (e.g., Roberts and Daniels, 1996; Radzevicius and Daniels, 2000; Tsoflias et al., 2004).

GPR data are commonly acquired using a perpendicular broadside antenna configuration; i.e., transmitter and receiver antennae are oriented parallel to each other and perpendicular to the direction of data acquisition (profile direction). As most GPR systems employ linearly polarized dipole antennae, the transmitting antenna emits an electromagnetic (EM) wavefield whose electric field is polarized parallel to the long axis of the dipole, and the receiving antenna records only the component parallel to its long axis. However, it has been noted that various targets of GPR surveys, such as buried pipes and fractures, have polarization-dependent scattering characteristics (e.g., Radzevicius and Daniels, 2000; Tsoflias et al., 2004; Orlando and Slob, 2009; Sassen and Everett, 2009). This implies that the visibility of a subsurface scatterer in the acquired data depends on the used antennae configuration (e.g., broadside configuration) and its orientation with respect to the feature to be imaged. As a consequence, certain subsurface objects might not be imaged using a single component perpendicular broadside antenna configuration. For example, Radzevicius and Daniels (2000) have found that the backscattered fields from buried cylinders (such as pipes and cables) may be strongly depolarized depending on the orientation of the cylinder relative to the antennae, the electrical properties of the cylinders and the background material, as well as the depth and radius-to-wavelength ratio of the cylinders. Thus, polarization dependent scattering properties have important implications for target detection, survey design, and data interpretation.

To address GPR polarization phenomena, various studies examined the use of recording GPR data at multiple transmitter-receiver configurations where, compared to the standard perpendicular broadside configuration, one or both antennae were rotated to acquire different components of the electric field. For example, Lehmann et al. (2000) suggested the combination of two GPR data sets recorded using perpendicular and parallel broadside antenna configurations, to create a pseudo-scalar wavefield. Furthermore, advanced 3D multi-configuration (also known as multi-component) imag-

ing approaches have been developed by van der Kruk et al. (2003) and Streich and van der Kruk (2007). Gestel and Stoffa (2001) made use of Alford rotations to extract the main axis of subsurface anisotropy and the orientation of buried objects from multi-polarization 2D GPR data while Seol et al. (2001) have applied a similar approach to find the strike of fractures. Tsoflias et al. (2004) made use of the phase characteristics from 2D multi-polarization measurements to detect vertical fractures. In addition, Roberts and Daniels (1996) have investigated GPR polarization phenomena associated with typical GPR targets and found that polarization characteristics may be extremely useful for detecting and characterizing small-diameter (relative to the incident wavelength), long circular cylinders such as buried pipes and cables. Radzevicius and Daniels (2000) have further investigated polarization and cylinder scattering concepts relevant for GPR. Considering the response of metal and plastic pipes with varying diameters, these authors also provide guidelines for survey design and data interpretation.

In this study, we present a dual-component 3D GPR processing flow using perpendicular and parallel broadside antenna configurations to efficiently image and characterize different types of buried utility pipes. Our attribute based processing and analysis strategy allows for improved target extraction and characterization by combining the geometrical and physical characteristics from both components into a novel depolarization attribute. Our strategy is illustrated using data collected at a field site where detailed ground-truth information is available. In the following, after introducing our field site and providing details regarding data acquisition and standard processing, we illustrate and discuss the main structural and polarization characteristics of our data. Then, we show how the structural information from both data sets can be enhanced by using a data attribute known as phase symmetry (Kovesi, 1996). To characterize the polarization characteristics of our two-component data set, we further employ two polarization attributes based on principle component analysis (PCA). Finally, through combination of the proposed structural and physical attributes, we illustrate how the major information from dual-component data sets can be fused into one attribute which significantly enhances the interpretability of such data sets.

## 5.3 Background

In the following sections, we introduce the survey site and our standard processing flow applied to the different data sets presented in this study.

### 5.3.1 Survey Site

GPR data has been acquired at a test site located in Horstwalde, Germany. This site has been installed by the University of Potsdam and the Federal Institute for Materials

Research and Testing and is located  $\sim 30$  km south of Berlin, Germany. The geology at the site is predominantly characterized by glacial sands and gravels deposited during the last glaciation periods. During the installation of this test site, consisting of several shallow to intermediate depth boreholes, numerous geophysical surveys have been conducted. The primary goal of these surveys was to identify optimum borehole locations which included the detection of subsurface utilities installed during the past century when the site was used as a military training area. During these studies, we found that the GPR technique provides the best performance at this site (compared to other geophysical techniques such as magnetic or EM induction mapping) and that multi-polarization data sets may further help to characterize the detected buried utilities.

### 5.3.2 Data Acquisition and Standard Processing

We conducted a dual-component 3D GPR data set (Figure 5.1) covering an area of  $\sim 20 \times 20$  m and several radial profiles (2D, Figure 5.2) across two selected target objects to further study polarization phenomena. The data sets were acquired using cart mounted unshielded 200 MHz Sensors&Software antennae with a fixed offset of 0.9 m. Positioning of the GPR traces was performed kinematically using a self-tracking total station (TTS). Details of this acquisition approach are presented in Böniger and Tronicke (2010a,b). The data sets were recorded using a time window of 300 ns, a sample interval of 0.2 ns, 6 vertical stacks, and an in- and crossline trace spacing of  $\sim 0.05$  m and  $\sim 0.1$  m, respectively.

Processing the 3D GPR data involved latency correction (Böniger and Tronicke, 2010b), zero-time correction, wow-removal, frequency filtering, and amplitude scaling using a smoothed average envelope. It should be noted that the same amplitude scaling function was used for both data sets  $X_{11}$  and  $X_{22}$  recorded using the perpendicular and parallel broadside antenna configuration, respectively. The data were then gridded onto a rectangular grid ( $0.1 \times 0.1$  m) using a natural neighbor based algorithm. Afterwards, the pre-processed data cubes were migrated using a 3D Stolt algorithm with a migration velocity of 0.111 m/ns derived from several common-midpoint (CMP) measurements. Figure 5.1 shows time slices through the unmigrated and migrated data cubes of the two co-polarized 3D data sets  $X_{11}$  and  $X_{22}$ . Here, we focus on the prominent linear features representing buried utility pipes. When comparing the  $X_{11}$  and the  $X_{22}$  slices, polarization effects are evident in the unmigrated and migrated data. Most of these features show a dominant polarization perpendicular to the orientation of the object. When comparing the unmigrated (Figures 5.1(a)–5.1(d)) and migrated data (Figures 5.1(e)–5.1(h)), we see that migration successfully focuses the diffracted energy and, thus, significantly improves the resolution capabilities of the data.



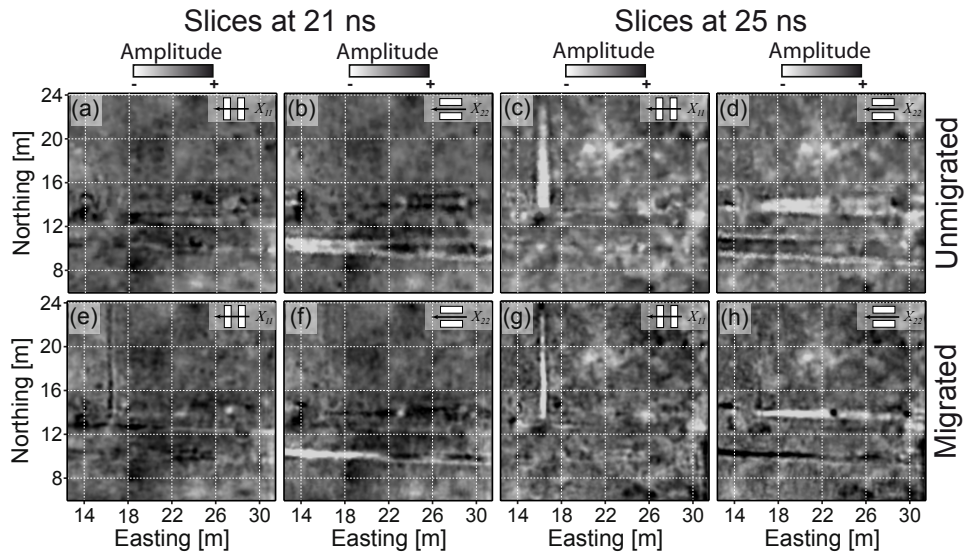


**FIGURE 5.1.** Unmigrated (a)–(d) and migrated (e)–(h) time slices through the 3D GPR data cubes at a two-way traveltime of 21 ns (a, b, e, and f) and 25 ns (c, d, g, and h). The symbols in the upper right corners indicate antenna orientation with respect to the inline direction.

To further analyze polarization phenomena in our 3D data, we acquired multiple radial profiles across two selected pipes showing different polarization behaviors. Figure 5.2 shows the survey geometry of these 2D lines including approximative pipe geometries derived from Figure 5.1. The radial surveys A and B were acquired using an angular discretization of  $\sim 10^\circ$  using a perpendicular broadside antennae configuration. Only basic processing (latency correction, zero-time correction, wow-removal and amplitude scaling followed by inline gridding) was applied to the radial profiles in order to highlight the observed polarization phenomena in minimally processed data. All profiles were gridded onto an offset range from -4 to 4 m relative to the pipe midpoint.  $0^\circ$  corresponds to a parallel and  $90^\circ$  to a perpendicular orientation relative to the observed pipe.

Figures 5.3 and 5.4 show the results of the radial surveys A and B, respectively. Focusing on the target of interest located at 0 m offset, Figure 5.3 highlights maximum amplitudes around  $0^\circ$ . While the corresponding diffraction hyperbola is still visible up to  $\sim 40^\circ$ , it is significantly attenuated at  $\sim 90^\circ$ . Visual inspection of all diffraction hyperbolas in Figure 5.3 already indicates that the event at 0 m offset is characterized by different polarization than the events at an offset of  $\sim -2$  m and  $\sim 2$  m, respectively. This observation is further supported by Figure 5.4, where the target diffraction at 0 m offset shows maximum amplitudes around  $90^\circ$ , while minimum amplitudes are

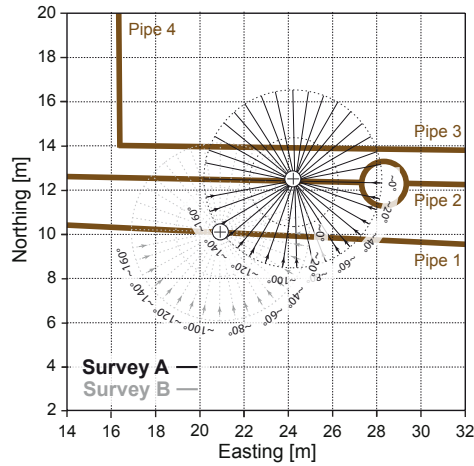


**FIGURE 5.2.** Geometry of the two radial GPR surveys A and B, each consisting of 18 rotated 200 MHz GPR profiles centered across two distinct subsurface linear features (utility pipes) showing different polarization characteristics. As known from the 3D GPR data (see Figure 5.1), A is located above a pipe with maximum amplitudes in the  $X_{11}$ -component while B is located above a pipe with maximum amplitudes in the  $X_{22}$ -component (see Figure 5.1). The pipes were numbered for future reference. The angles illustrate approximative orientation of the profiles relative to the respective pipe with arrowheads depicting the direction of acquisition. The dashed circles indicate the 2 and 4 m radial distance relative to the survey midpoint identified by +.

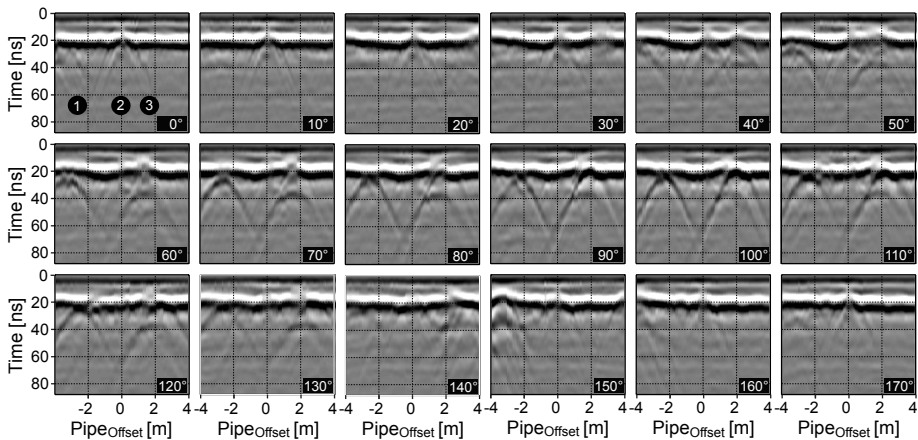


**FIGURE 5.3.** Gridded radial profiles from survey A (Figure 5.2) acquired at angles of  $0^\circ$ – $170^\circ$  relative to the pipe orientation. The survey midpoint is located at an offset of 0 m above the corresponding target utility pipe. The circular labels indicate an approximate pipe location. The pipe numbers refer to the ones introduced in Figure 5.2. All the profiles were plotted on an equal scale.

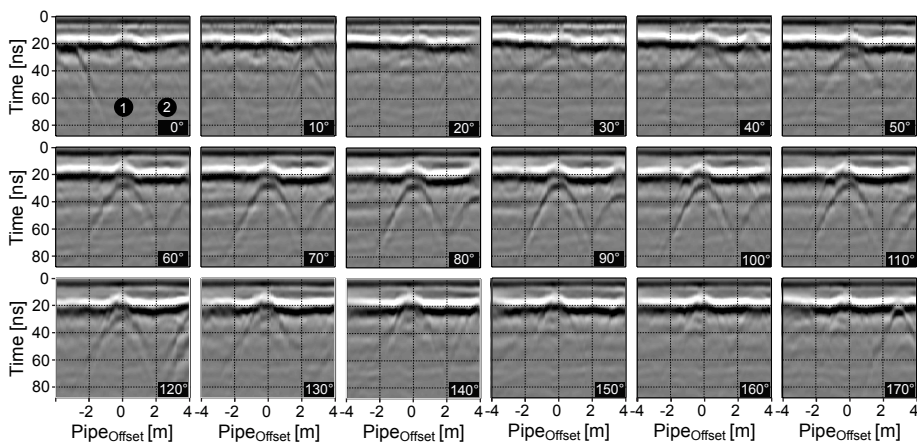


**FIGURE 5.4.** Gridded radial profiles from survey B (Figure 5.2) acquired at angles of  $0^\circ$ – $170^\circ$  relative to the pipe orientation. The survey midpoint is located at an offset of 0 m above the corresponding target utility pipe. The circular labels indicate an approximate pipe location. The pipe numbers refer to the ones introduced in Figure 5.2. All the profiles were plotted on an equal scale.

found around  $0^\circ$ . Summarizing the observations from Figures 5.1, 5.3, and 5.4, our data suggest that the survey site consists of two types of pipes characterized by differences in reflection and polarization strength. To further analyze and interpret these effects, we will introduce attributes focusing on: (1) enhancing the geometry of the target features (based on their characteristic symmetry) and (2) extract characteristic polarization effects. This may help to further characterize the physical properties of these features.

## 5.4 Geometrical Extraction using Phase Symmetry

Interpretation of GPR data is commonly based on visual inspection of coherent events, which from our point of view is often based on the perception of feature symmetry. Symmetry represents an important biological characteristic in order to distinct between, e.g., animals and static environmental backgrounds (Tyler, 2002; Wagemans, 1995), whereby its visual perception developed during evolution. Man-made objects often exhibit intrinsic symmetry (e.g., mirror or rotational) for different reasons, for example improved structural stability from an engineering point of view. Subsurface utilities also exhibit symmetry usually facilitating visual perception when inspecting GPR time slices. In order to detect and extract subsurface utilities from 3D GPR data in heterogeneous materials, we will exploit feature symmetry.

Another observation based on visual perception is the significance of phase informa-

tion for feature detection. Huang et al. (1975); Morrone and Owens (1987) showed how phase information contributes to the human perception of discontinuities (such as edges) in images. Following these studies, Kovesei (1997, 1999) introduced a phase based feature extraction algorithm making use of 2D rotational log-Gabor filters (Field, 1987) for edge and symmetry detection. Gabor filters, and subsequently log-Gabor filters have often been attributed filtering properties similar to the ones found in mammalian cortical cells (Field, 1987). Log-Gabor functions are defined by a Gaussian amplitude spectrum (if plotted on a logarithmic frequency scale with a zero DC component) and provide a high spatial and frequency localization. Phase symmetry, a contrast invariant measure, was introduced by Kovesei (1997) to highlight feature symmetry within 2D images. Russell et al. (2009) just recently applied a related phase-based edge detection algorithm to highlight faults in 3D seismic data.

In the following, we briefly introduce our phase symmetry based processing flow using a synthetic example in accordance with our field data. Subsequently, we apply our processing flow to the dual-component 3D GPR field data set. For a detailed introduction on phase based edge and symmetry detection, we refer the interested reader to Kovesei (1997).

### 5.4.1 Phase Symmetry

As introduced by Kovesei (1997) phase symmetry consists of 2D log-Gabor filter banks, obtained by element-wise multiplication of the radial component, i.e., the log-Gabor transfer function with an angular Gaussian scaling function,

$$G(\omega, \theta) = \exp \left( \frac{-\log(\omega/\omega_0)^2}{2 \cdot \log(k/\omega_0)^2} - \frac{d\theta^2}{2 \cdot \sigma_\theta^2} \right). \quad (5.1)$$

$\omega$  and  $\omega_0$  are the frequency range and the center frequency, respectively.  $k$  corresponds to a scaling factor,  $d\theta$  to the angular difference to the specified filter orientation, and  $\sigma_\theta$  defines the standard deviation of the applied Gaussian filter. Applied over multiple scales and orientations, one obtains a filter bank representation of the image (e.g., a GPR time slice) that consists of an even- and odd-symmetric filter output. As demonstrated for a 1D signal by Kovesei (1997), points with high symmetry are characterized by high magnitudes in the even-symmetric filter output but low magnitudes in the odd-symmetric filter outputs. Therefore, phase symmetry at the spatial coordinates  $i, j$  is defined as

$$\mathcal{S}(i, j) = \max \left\{ \frac{\sum_{r,n} \left( \left[ |e_{r,n}(i, j)| - |o_{r,n}(i, j)| \right] - T \right)}{\sum_{r,n} A_{r,n}(i, j) + \epsilon}, 0 \right\}, \quad (5.2)$$

where the max-operator limits the attribute to symmetric features, and  $e_{r,n}$  and  $o_{r,n}$  are the even- and odd-symmetric filter outputs, respectively, at orientation  $r$  and scale  $n$ .  $T$  represents a noise compensation term, and  $\epsilon$  was introduced to avoid instabilities by zero division.  $A_{r,n}$  represents the magnitude per orientation and scale, and is defined as

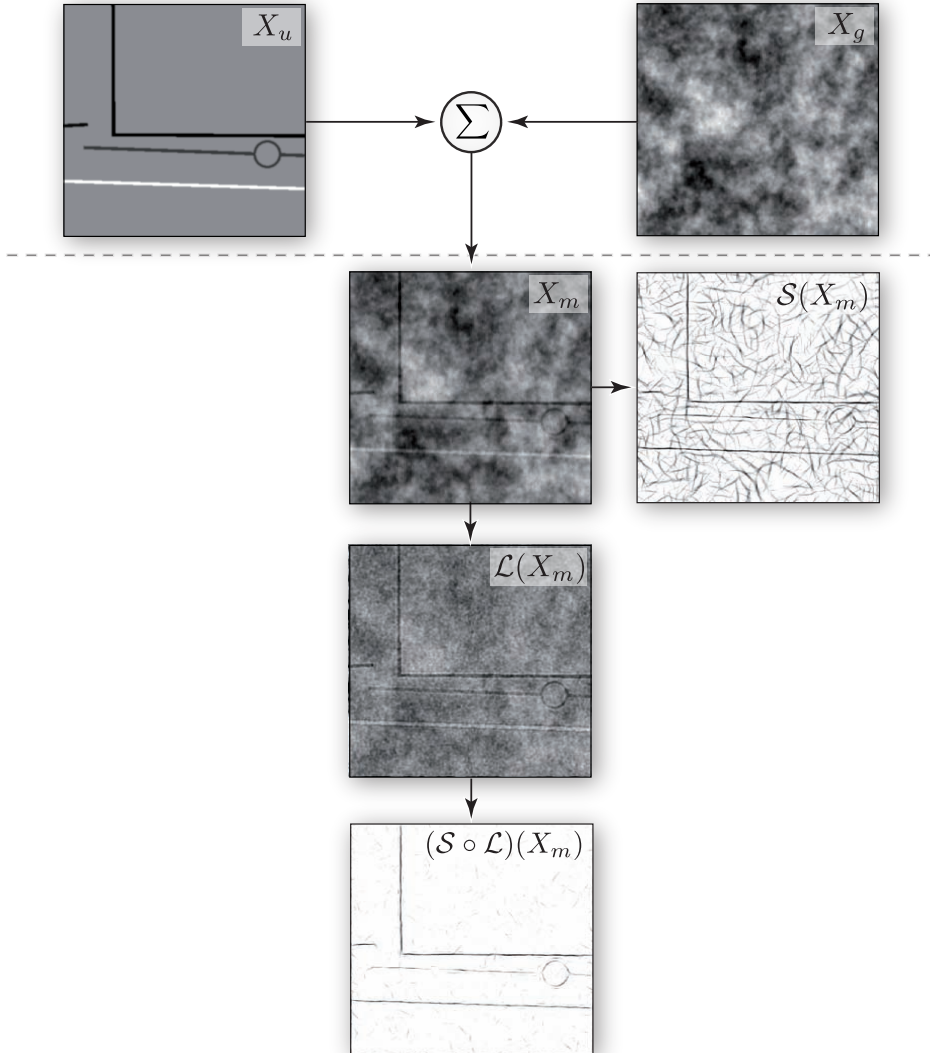
$$A_{r,n}(i, j) = \sqrt{e_{r,n}(i, j)^2 + o_{r,n}(i, j)^2}. \quad (5.3)$$

The advantages of this phase based symmetry measure is its normalization to a range between 0 and 1 and its robustness against changes in contrast as often observed in GPR time slice data.

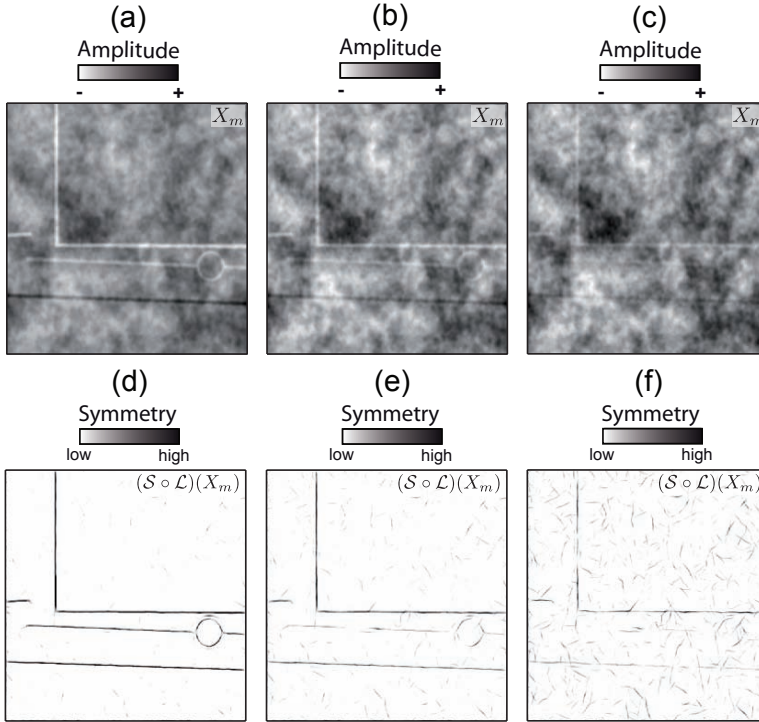
### 5.4.2 Synthetic Examples

Figure 5.5 illustrates our proposed feature extraction approach using a synthetic example in accordance to the previously introduced field data.  $X_u$  and  $X_g$  represent the utility and geological background response, respectively, and  $X_m = X_u + X_g$  simulates a migrated GPR time slice image. Calculation of phase symmetry  $\mathcal{S}(X_m)$  successfully enhances the target features from  $X_m$  as well as symmetric features from  $X_g$ . In order to suppress the geological background response, we use an image processing step called Laplacian-highboosting (Gonzalez and Woods, 2002) prior to the calculation of the  $\mathcal{S}$ -attribute. Thereby, we attenuate large scale, global features (introduced by  $X_g$ ) and enhance sharp local features. The result of applying Laplacian-highboosting to  $X_m$  is shown in the panel labeled  $\mathcal{L}(X_m)$ . Subsequent calculation of phase symmetry ( $\mathcal{S} \circ \mathcal{L})(X_m)$  shows a significantly improved result compared to  $\mathcal{S}(X_m)$ . Feature continuity agrees well with the one obtained by visual inspection.

To further investigate the efficiency of phase symmetry for utility extraction, we conducted a noise study using the synthetic example from Figure 5.5. In doing so, we steadily decreased the amplitude ratio between  $X_u$  and  $X_g$ . Figure 5.6 illustrates the results of this analysis for three selected  $X_u$ -to- $X_g$  ratios. As expected, by decreasing the  $X_u$ -to- $X_g$  ratio the resulting phase symmetry image ( $\mathcal{S} \circ \mathcal{L})(X_m)$  shows an increasing amount of features from  $X_g$  because Laplacian-highboosting becomes less efficient. However, for all  $X_u$ -to- $X_g$  ratios, the extracted utility features (Figures 5.6(d)–5.6(f)) are again in good agreement with features an experienced interpreter would depict by visually inspecting the individual images (Figures 5.6(a)–5.6(c)).



**FIGURE 5.5.** Suggested feature extraction approach applied to a synthetic image ( $X_m$ ) representing a single GPR time slice generated from utilities ( $X_u$ ) and a geological background ( $X_g$ ).  $\mathcal{S}(X_m)$  is the result when phase symmetry is calculated directly from  $X_m$ . In order to improve the phase symmetry result, preprocessing using Laplacian-highboosting ( $\mathcal{L}(X_m)$ ) is applied, which produces a favorable extraction result  $((\mathcal{S} \circ \mathcal{L})(X_m))$ . For details see text.



**FIGURE 5.6.** Evaluation of the influence of the  $X_u$ -to- $X_g$  ratio on the performance of phase symmetry based feature extraction. (a)–(c) GPR time slice images  $X_m$  with decreasing  $X_u$ -to- $X_g$  ratio from left to right. (d)–(f) corresponding phase symmetry images obtained after Laplacian-highboosting  $(S \circ L)(X_m)$ .

### 5.4.3 Application to Field Data

For the dual-component GPR data collected at the Horstwalde test site, we calculate  $\mathcal{S}$  for each data set after applying Laplacian-highboosting. The information from the  $X_{11}$  and  $X_{22}$  data is combined by

$$\mathcal{S}_{dc} = \max \{ (\mathcal{S} \circ \mathcal{L})(X_{11}), (\mathcal{S} \circ \mathcal{L})(X_{22}) \}, \quad (5.4)$$

to ensure maximum information from both components. The application of a temporal running-average filter (window size 1.4 ns) has proven to further emphasize the expected target features. Given the  $\mathcal{S}_{dc}$  image, we calculate the feature angle  $\phi_f$  using Prewitt gradients (Gonzalez and Woods, 2002) by

$$\phi_f = \left| \arctan \left( \frac{\mathcal{S}_{dc} * P_E}{\mathcal{S}_{dc} * P_N} \right) \right| - \frac{\pi}{4}, \quad (5.5)$$

with  $P_N$  and  $P_E$  being the convolutional Prewitt operators sensitive along local northing and easting, respectively. Figure 5.7 shows the application of this procedure to a selected time slice at 21 ns (see also Figure 5.1). For comparison, Figure 5.7(a) shows a migrated data slice after fusing the migrated data cubes  $X_{11}$  and  $X_{22}$  (Figure 5.1(e) and 5.1(f)). Fusion is performed using a weighted summation, where the weights are based on the signal energy calculated over a window length corresponding to the dominant wavelength. This fusion approach minimizes information loss (loss of sharpness) in a signal-driven manner.

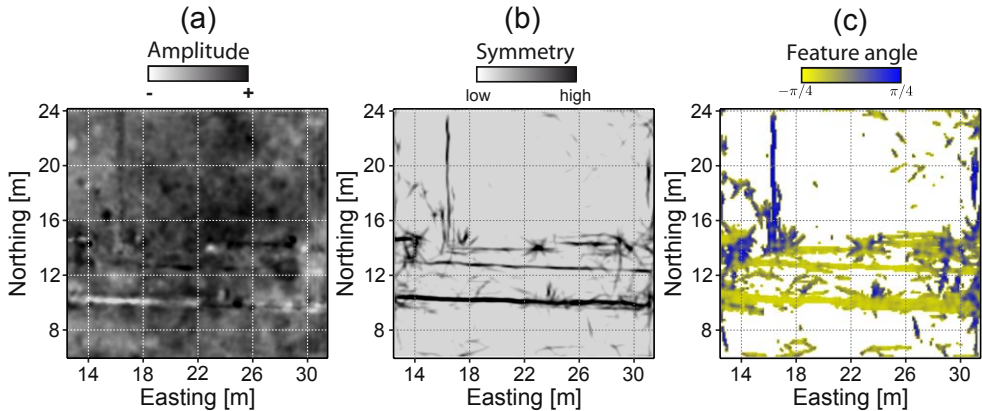


**FIGURE 5.7.** (a) Fused  $X_{11}$  and  $X_{22}$  data time slice at 21 ns, (b) corresponding phase symmetry  $\mathcal{S}_{dc}$ , and (c) feature angle  $\phi_f$  slices calculated using Equation 5.4 and 5.5, respectively.

An alternative, wavelet based, data fusion method can be found in Hugenschmidt and Kalogeropoulos (2009). It should be noted that the fused data is only used for comparison, while all attribute analyses are performed using the individual  $X_{11}$  and  $X_{22}$  data.

Comparing Figures 5.7(a)–5.7(c), we see that  $\mathcal{S}_{dc}$  successfully highlights the target objects, i.e., three west–east and one north–south oriented utility pipes, while  $\phi_f$  quantifies the orientation of these objects. Later on,  $\phi_f$  is used to calculate a new depolarization attribute and  $\mathcal{S}_{dc}$  is used to render the target objects in 3D.

## 5.5 PCA Derived Polarization Attributes

Principal component analysis (PCA) is a common statistical tool in various scientific fields including the analysis of geophysical data (Wagner and Owens, 1996; Scheevel and Payrazyan, 2001; Karlsen et al., 2001; Gámez et al., 2004; Pereira et al., 2010). In the following, we introduce the basics of PCA being relevant for our analyses. For



a detailed introduction into the field of PCA, we would like to refer the interested reader to Mari and Chapellier (1999); Jolliffe (2002).

PCA is based on the extraction of dominant features from the data covariance matrix. The eigenvalues of the covariance matrix, in our case from  $X_{11}$  and  $X_{22}$ , represent the so-called principal components. From these principle components, several attributes can be derived. In this study, we focus on the polarization angle  $\phi_p$  and the linearity  $\mathcal{R}$ . The polarization angle (Mahob and Castagna, 2002) is the orientation of the two principle components ( $pc_1$  and  $pc_2$ ) which we calculate by

$$\phi_p = \left| \arctan \left( \frac{pc_1}{pc_2} \right) \right| - \frac{\pi}{4}. \quad (5.6)$$

As used here, linearity (also termed degree of rectilinearity) has been introduced by Flinn (1965). In our case, it is defined as

$$\mathcal{R} = 1 - \left( \frac{\min \{ \lambda_{C,1}, \lambda_{C,2} \}}{\max \{ \lambda_{C,1}, \lambda_{C,2} \}} \right), \quad (5.7)$$

with  $\lambda_{C,i}$  being the  $i^{th}$  eigenvalue of the covariance matrix.

### 5.5.1 Synthetic Studies

To further illustrate  $\phi_p$  and  $\mathcal{R}$  to analyze GPR data, Figure 5.8 shows the influence of amplitude and phase variations of a Morlet wavelet on these attributes. In Figure 5.8(a), the two components/waveforms ( $X_{11}$  and  $X_{22}$ ) are identical and, thus, result in  $\phi_p = 0$  (no polarization) and  $\mathcal{R} = 1$  (complete redundancy). In Figure 5.8(b), we introduce a phase shift between the two waveforms of  $\pi/2$ , which results in  $\phi_p = 0.785$  and  $\mathcal{R} = 0$ . Here, it is obvious that for  $\mathcal{R}$  close to zero (e.g., circular polarization)  $\phi_p$  is not well defined. Figure 5.8(c) and 5.8(d) further demonstrate the influence of amplitude and phase variations. It can be seen that amplitude variations rotate  $\phi_p$ , while phase variations predominantly influence  $\mathcal{R}$ .

In order to investigate the influence of amplitude and phase variations between two waveforms, we calculated 2D parameter maps over varying amplitude and phase terms. Figure 5.9(a) represents the effects of amplitude variations between  $X_{11}$  and  $X_{22}$  and its influence on  $\phi_p$ .  $\phi_p$  clearly depicts the amplitude variations between  $X_{11}$  and  $X_{22}$ , while  $\mathcal{R}$  is insensitive to such variations (not shown in Figure 5.9(a)). Figure 5.9(b) shows the influence of phase variations between 0 and  $2\pi$  on  $\mathcal{R}$ . In contrast to amplitude variations, phase variations do not influence  $\phi_p$  (not shown Figure 5.9(b)) but have a significant influence on  $\mathcal{R}$ , which is indicated by the regular patterns in Figure 5.9(b). These plots help to understand the sensitivity of  $\phi_p$

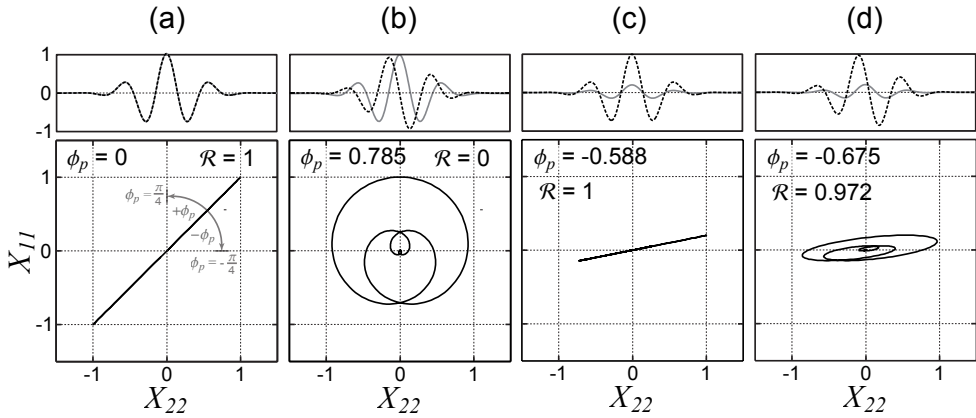


**FIGURE 5.8.** Four potential scenarios to illustrate the proposed attributes  $\phi_p$  and  $\mathcal{R}$ . The examples are calculated using Morlet wavelets to represent dual-component GPR data ( $X_{11}$ ,  $X_{22}$ ). (a) identical (unpolarized) waveforms, (b) phase-shifted waveforms, (c) in-phase waveforms with different amplitudes, and (d) phase-shifted waveforms with differing amplitudes.

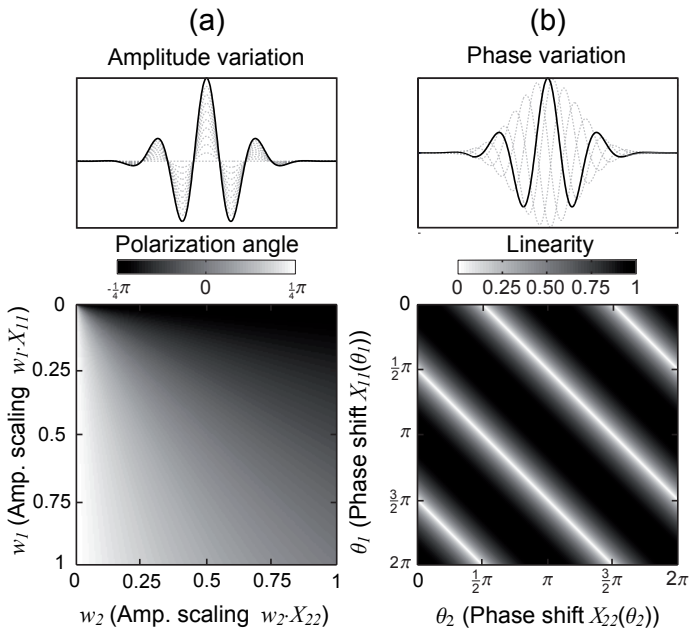


**FIGURE 5.9.** Influence of (a) waveform amplitude variations and (b) phase-shifts on the proposed attributes  $\phi_p$  and  $\mathcal{R}$ . The examples are calculated using Morlet wavelets to represent dual-component GPR data ( $X_{11}$  and  $X_{22}$ ).

and  $\mathcal{R}$  with respect to amplitude and phase differences between two waveforms and represent the basis to analyze our dual-component 3D GPR data.

### 5.5.2 Application to Field Data

For the dual-component GPR data collected at the Horstwalde field site, we calculated the PCA derived attributes  $\phi_p$  and  $\mathcal{R}$  using Equation 5.6 and 5.7 (Figure 5.10). We calculated  $\phi_p$  and  $\mathcal{R}$  from the unmigrated (Figures 5.10(a) and 5.10(b)) and migrated (Figures 5.10(c) and 5.10(d)) data cubes for a selected time slice at 21 ns (see Figure 5.1) using a time window of 12 ns. Polarization angles (Figures 5.10(a) and 5.10(c)) further quantify which data set dominates in specific areas; e.g., positive angles indicate that  $X_{11}$  amplitudes are significantly larger than the corresponding  $X_{22}$  amplitudes. Linearity (Figures 5.10(b) and 5.10(d)) enhances the target features. The

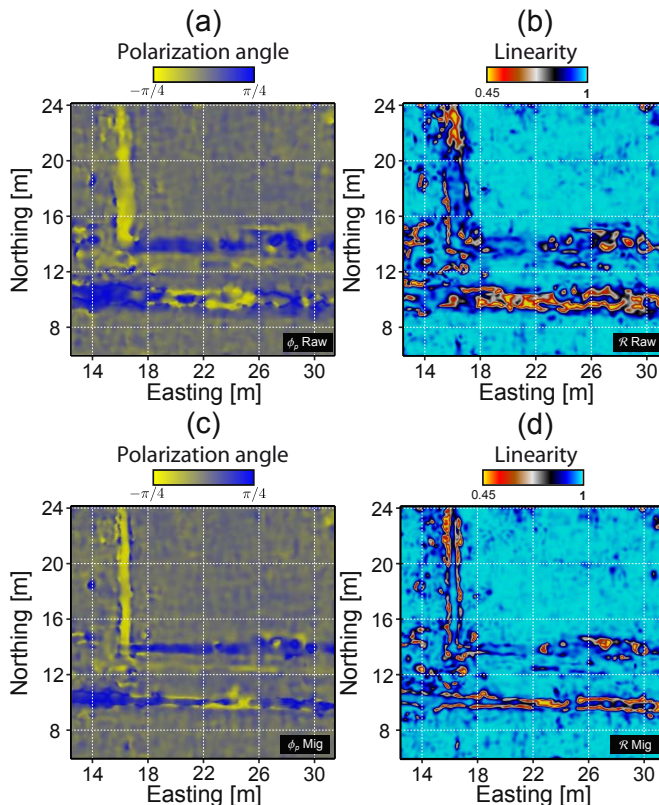


**FIGURE 5.10.** (a)  $\phi_p$  and (b)  $\mathcal{R}$  calculated over a time window length of 12 ns using the unmigrated data cubes. (c)  $\phi_p$  and (d)  $\mathcal{R}$  calculated over a time window length of 12 ns using the migrated data cubes.

result is similar to an edge enhancing attribute due to strong waveform changes at the pipe edges. Comparison of unmigrated and migrated attribute slices illustrates the focusing effect of migration, resulting in significantly sharper images. When comparing Figures 5.10(c), 5.10(d), and Figure 7(b), it is evident that the west–east oriented pipe at  $\sim 12\text{--}13$  m Northing is not clearly imaged by  $\mathcal{R}$ . For this object, negative  $\phi_p$  values indicate different polarization phenomena compared to the west–east oriented pipes at  $\sim 10$  m and  $\sim 14$  m Northing, respectively. Thus, we conclude that the polarization attributes  $\phi_p$  and  $\mathcal{R}$  represent efficient tools to highlight and summarize polarization effects usually present in multi-component GPR data.

## 5.6 Depolarization Analysis

In order to combine the information from the two attributes defined above (feature and polarization angle), we introduce a novel attribute, called depolarization  $D_p$ :

$$D_p = \begin{cases} \phi_p/\phi_f, & \text{if } |\phi_f| \geq |\phi_p| \\ \phi_f/\phi_p, & \text{if } |\phi_f| < |\phi_p|, \end{cases} \quad (5.8)$$

where  $\phi_f$  and  $\phi_p$  are calculated using Equation 5.5 and 5.6, respectively.  $D_p$  varies between -1 and 1. A  $D_p$  value of 1 indicates a feature exhibiting maximum polarization with the long axes of the antenna dipoles parallel to the long axis of the feature. In contrast, a  $D_p$  of -1 indicates a feature exhibiting maximum polarization with the long axes of the antenna dipoles perpendicular to the long axis of the feature.

Figure 5.11 shows the final interpretation of our dual-component data set including extracted target depths (Figure 5.11(a)), calculated  $D_p$  attribute values (Figure 5.11(b)), and available ground-truth information (Figure 5.11(c)). In Figures 5.11(a) and 5.11(b), rendering of all pipe features shown is based on iso-surfaces calculated from the 3D phase symmetry cube (see also Figure 7(b)). Figure 5.11(a) shows the extracted features with the top-depth mapped onto the iso-surface. It can be seen that the pipes are located at varying depths ranging from  $\sim 1.11$  m to  $\sim 0.95$  m. In Figure 5.11(b), we mapped  $D_p$  onto the same iso-surfaces. This Figure illustrates how this depolarization attribute successfully combines the geometrical and physical information of the  $X_{11}$  and  $X_{22}$  data sets. Pipes labeled 1, 3, and 4 are characterized by parallel polarizations, while Pipe 2 shows orthogonal polarization. Based on these observations our data suggest that two different kinds of pipes are present at our site. Strong parallel depolarization is usually indicative for steel pipes (e.g., Roberts and Daniels, 1996; Radzevicius and Daniels, 2000; Porsani et al., 2010), and thus, we interpret Pipes 1, 3, and 4 as steel pipes. On the other hand, Pipe 2 shows weaker amplitudes and a weak orthogonal polarization. This indicates that the dielectric

properties of the pipe material are comparable to those of the geologic background; i.e., Pipe 2 can be interpreted as a stoneware pipe (e.g., Porsani et al., 2010).

In order to validate this interpretation, we conducted excavations at four selected locations. Figure 5.11(c) illustrates our excavation results, which confirm our GPR data interpretation. Pipes 1, 3, and 4 (characterized by strong polarization effects) represent a network of galvanized steel pipes with a diameter of  $\sim 40$  mm located at a depth range between 1.10 and 0.66 m. The weakly polarized event (Pipe 3)

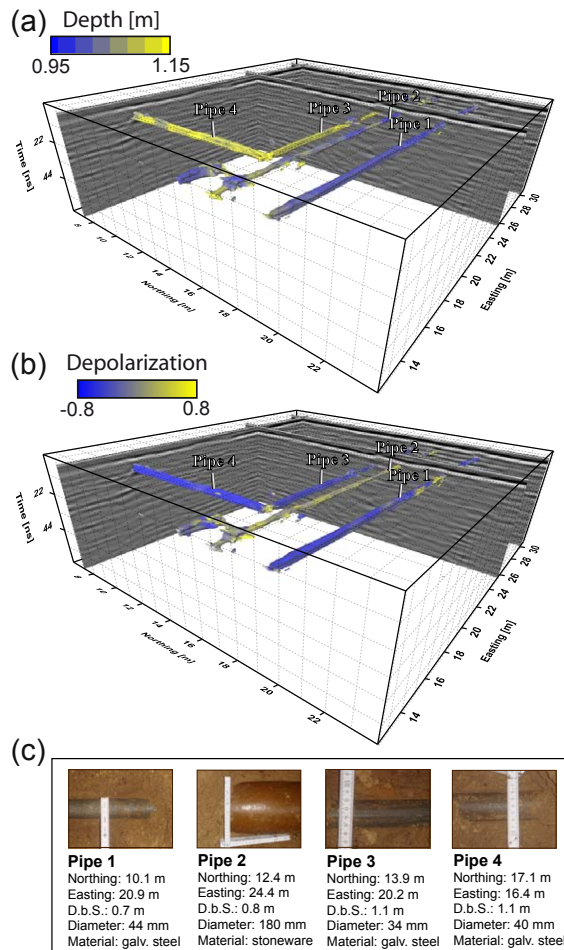


**FIGURE 5.11.** Final interpretation of the 3D GPR field data: (a) depth to the top pipe surface, calculated using a constant velocity of 0.111 m/ns, mapped onto iso-surfaces extracted from the phase symmetry cube. (b) depolarization attribute mapped onto the extracted iso-surfaces, and (c) ground-truth information obtained from excavation. The white markers in (a) and (b) correspond to the pipe locations from the available ground-truth information.

proved to be a sewer pipe made of stoneware with a diameter of  $\sim 180$  mm buried at a depth of  $\sim 0.74$  m below surface. The depths observed for Pipes 1 and 2 differ from the extracted ones. Inspecting Figures 5.3, 5.4, and 5.11 in detail, we see that the reflections from these pipes interfere with the ground-wave arrivals. Detailed analysis of the traces at the corresponding locations shows that this interference is predominantly shifting the peak energy of these pipe responses to larger depths. The strong depth and positional match between GPR and excavations results for Pipes 3 and 4 illustrate that using higher antenna frequencies (resulting in a clearer separation between the ground-wave and the pipe reflections) would also improve the extracted depth locations of these pipes.

## 5.7 Conclusions

Using field data recorded across different utility pipes at a well constrained field site, we have demonstrated the potential of considering and analyzing polarization phenomena in 3D GPR data. We have introduced an attribute based processing flow to enhance the structural and physical characteristics of the target objects. These attributes are calculated from dual-component 3D GPR data consisting of two data volumes recorded using parallel and perpendicular broadside antenna configurations, respectively.

Phase symmetry has proven to successfully delineate the objects of interest as this attribute highlights symmetrical features and also allows for volumetric feature extraction. Furthermore, principal component analysis has proven to be a feasible tool to extract the dominant polarization characteristics from dual-component GPR data. We have calculated the PCA-based attributes polarization angle and linearity and found that these attributes are extremely useful to further characterize the target utility objects. Combination of our structurally and physically based attributes into a single new attribute, called depolarization, allows at this point to distinguish between metallic and non-metallic objects based on their depolarization characteristics. This is a major improvement compared to standard GPR approaches largely relying on interpreting diffraction hyperbolas in single component data sets. Thus, we have successfully developed an approach towards the inclusion of polarization characteristics of GPR wavefields into attribute based analysis and interpretation flows.

Given the recent availability of multi-component sensor systems acquiring different antenna configurations simultaneously, we believe that a combined interpretation, as developed in this study, can result in significantly improved interpretation for utility detection and characterization. Application of this algorithm for automatic feature extraction and classification will be a focus of future work. Additionally, including cross-polarized or  $45^\circ$  broadside configurations into the surveying strategy might

further improve the potential of our approach. Aside from utility detection and characterization, our strategy might also be applicable to other GPR applications; e.g., the characterization of geological targets such as fractures and faults.

## 5.8 Acknowledgments

Significant parts of this study were implemented in the software package OpenDTect. We therefore would like to express our gratitude to dGB Earth Sciences for making their Interpretation Software OpenDTect freely available to academic research. We also would like to thank the Federal Institute for Material Research and Testing (BAM), Germany, and especially Ernst Niederleithinger for fruitful collaboration at the Horstwalde test site. This research was financially supported by the Deutschen Forschungsgemeinschaft (DFG), project TR512/1-2.





# HIGH-RESOLUTION GPR DATA ANALYSIS USING EXTENDED TREE-BASED PURSUIT

**Böniger U., Tronicke, J.**

modified after expanded abstract from 12<sup>th</sup> *International Conference on Ground Penetrating Radar, Birmingham 2008*; submitted to *Journal of Applied Geophysics* (2010)

---

## 6.1 Abstract

Decomposition of geophysical signals (e.g., seismic and ground-penetrating radar data) into the time-frequency domain has shown to provide valuable information for advanced interpretation (e.g., tuning effects) and processing (e.g., inverse Q-filtering). The quality of these subsequent processing steps is strongly related to the resolution of the selected time-frequency representation (TFR). In this study, we introduce a high-resolution spectral decomposition approach representing an extension of the recently proposed Tree-Based Pursuit (TBP) method. Our spectral decomposition method significantly reduces the computational cost compared to the well known Matching Pursuit (MP) technique by introducing a tree structure prior to the actual matching procedure. Following the original implementation of TBP, we additionally incorporate waveforms commonly used in geophysical data processing and present an alternative approach to take phase shifts into account. Application of the proposed method to synthetic data and comparison of the results with other typically used decomposition approaches, illustrates the ability of our approach to provide decomposition results highly localized in both time and frequency. Applying our procedure to field GPR data illustrates its applicability to real data and provides examples for potential applications such as analyzing thin-bed responses and modulating the data frequency content.

## 6.2 Introduction

Driven by the ongoing developments in multiresolution analysis (e.g., Mallat, 2001), time-frequency analysis has become increasingly popular within various scientific disciplines (e.g., biology, economics, engineering, and geophysics). Spectral decomposition, that is, separating the data into its individual frequency components, has proven to be a valuable tool for advanced interpretation and processing of nonstationary geophysical data. Today, spectral decomposition is successfully applied to common problems in exploration seismics, such as subtuning thickness estimation, bright spot delineation, as well as channel detection, enhancement, and characterization (e.g., see Chopra and Marfurt, 2007).

Similar to the success in seismic data processing, several interesting applications for time-frequency analysis of ground penetrating radar (GPR) data have emerged. For data interpretation, spectral decomposition of GPR data offers the possibility to characterize the subsurface architecture (Bradford and Wu, 2007; Geerdes and Young, 2007) based on analyzing the frequency evolution with time and depth, respectively. Additionally, time-frequency analysis allows for advanced data processing, e.g., time-varying frequency filtering or inverse Q-filtering (Irving and Knight, 2003). The quality and reliability of such analyses and processing steps depend strongly on the resolution of the selected time-frequency representation.

In this study, we will first give a brief overview on common methods used for spectral decomposition and, second, introduce a new method based on Tree-Based Pursuit (TBP) (Jost et al., 2006). Our novel variant of the TBP approach is computationally efficient and provides detailed representations in both time and frequency. In order to assess the potential of our method, we compare it with other commonly used time-frequency representations by analyzing a synthetic GPR trace composed of modulated Ricker wavelets. Finally, we apply our technique to real GPR data to study thin-bed responses and present an efficient scheme to correct for potential frequency attenuation and thus to increase the average frequency content.

## 6.3 Spectral decomposition methods

Given the ongoing strong interest in time-frequency analysis, today's scientists are faced with numerous techniques in order to assess the time-frequency distribution of a given signal. The best known and probably most commonly used method is the Short-Time Fourier Transform (STFT), although its problems for joint time-frequency resolution are well documented (Mallat and Zhang, 1993). Additionally, wavelet based methods like the Continuous Wavelet Transform (CWT) or energy based time-frequency methods such as the Wigner-Ville (WVD) or Choi-Williams

decomposition can be used (for details see Chakraborty and Okaya, 1995; Chopra and Marfurt, 2007; Mallat, 2001). While each method might work with varying success for different types of signals, it has been shown that Matching Pursuit (MP) based approaches provide the best time-frequency resolution for seismic signals (e.g., Castagna and Sun, 2006; Chakraborty and Okaya, 1995; Chopra and Marfurt, 2007).

Emerging from the work on adaptive signal representation, Mallat and Zhang (1993) introduced Matching Pursuit (MP), a greedy algorithm iteratively decomposing a given signal  $f$  into a linear expansion of atoms  $g_\gamma$  (basic waveforms) selected from a redundant set (a so-called dictionary  $\mathcal{D}$ ). In a matching pursuit algorithm, one iteratively subtracts the waveform  $\langle R^{(n-1)}f, g_{\gamma_n} \rangle g_{\gamma_n}$  from the residual  $(R^{(n-1)}f)$ , with  $R^{(0)}f \leftarrow f$  at iteration  $n$  with

$$g_{\gamma_n} = \arg \max_{\mathcal{D}} \langle R^{(n-1)}f, g_\gamma \rangle. \quad (6.1)$$

The approximated signal  $\hat{f}_N$  ( $N$ : maximum number of iterations/matched atoms) can then be written as

$$\hat{f}_N = \sum_{n=1}^N a_n g_{\gamma_n}, \quad (6.2)$$

where  $a_n$  is the coefficient and  $g_{\gamma_n}$  the best matched atom from iteration  $n$ . The size or completeness of  $\mathcal{D}$  affects the quality and resolution of the signal decomposition. The dictionary is usually highly redundant, resulting in low computational efficiency. The high computational cost mainly limits practical application of MP to large geophysical data sets. In our opinion, this is the main reason why modified approaches have been introduced. For example, in order to reduce the computational cost and optimize the localization Liu and Marfurt (2005) introduced a matching-pursuit based algorithm, which iteratively subtracts Ricker or Morlet wavelets, which are matched in a least-squares sense and are located at the envelope peaks of the residuals.

In the following, we present a new variant of MP for the analysis of geophysical data, which is called Tree-Based Pursuit (TBP) and has been originally introduced by Jost et al. (2006). We modify the TBP approach of Jost et al. (2006) by including common geophysical waveforms (e.g., Ricker wavelets) into  $\mathcal{D}$  and, furthermore, provide an alternative approach to incorporate phase information.

## 6.4 Modified tree-based pursuit

Matching Pursuit and its variants have proven to provide high resolution spectral decompositions of geophysical signals (e.g., Castagna and Sun, 2006; Chopra and Marfurt, 2007), mostly at the expense of high computational cost. TBP significantly

---

**Algorithm 1:** Modified Tree-Based Pursuit algorithm based on the original approach proposed by Jost et al. (2006).

---

**Input:**  $\mathcal{T} = \{c_i, m_i\}$ : tree for dictionary  $\mathcal{D}$   
 $\sigma$ : local search window  
 $k$ : number of phase shifts  
 $f$ : signal to decompose

**Output:**  $\{g_n\}$ : set of atoms used for approximation  
 $\{a_n\}$ : set of projections

- 1  $n \leftarrow 0; R^{(0)} f \leftarrow f$
- 2  $\forall j = 1, \dots, k : \theta_j \leftarrow \frac{j-1}{k-1} \pi$
- 3 **repeat**
- 4     **foreach**  $j$  **do**
- 5          $R_{\theta_j}^{(n)} f \leftarrow \mathcal{F}(R^{(n)} f, \theta_j)$
- 6          $[p_{opt_j}, c_{opt_j}] \leftarrow \arg \max_{p, c \in c_0} \left| \left\langle R_{\theta_j}^{(n)} f, T_p m_c \right\rangle \right|$
- 7         **end**
- 8          $\nu \leftarrow \arg \max_j \left| \left\langle R_{\theta_j}^{(n)} f, T_{p_{opt_j}} m_{c_{opt_j}} \right\rangle \right|$
- 9          $[p_{opt}, c_{opt}, \theta_{opt}] \leftarrow [p_{opt_\nu}, c_{opt_\nu}, \theta_\nu]$
- 10         **while**  $|c_{opt}| > 1$  **do**
- 11              $[p_{opt}, c_{opt}] = \arg \max_{p, c \in c_{opt}} \left| \left\langle R_{\theta_{opt}}^{(n)} f, T_p m_c \right\rangle \right|, \quad \text{s.t.} \quad |p - p_{opt}| \leq \sigma$
- 12         **end**
- 13          $n \leftarrow n + 1$
- 14          $g_n \leftarrow T_{p_{opt}} g_{c_{opt}}$
- 15          $a_n \leftarrow \left\langle R_{\theta_{opt}}^{(n-1)} f, g_n \right\rangle$
- 16          $w_{opt} \leftarrow \mathcal{F}(a_n g_n, -\theta_{opt})$
- 17          $R^{(n)} f \leftarrow R^{(n-1)} f - w_{opt}$
- 18 **until** *stopping criterion is reached*

---

reduces the computational cost of MP by creating a tree structure using the atoms of  $\mathcal{D}$  prior to the actual matching procedure (Jost et al., 2006). Thereby, the atoms of  $\mathcal{D}$  are clustered into maximally incoherent waveforms (so-called molecules  $m$ ). By successive clustering of the molecules, a tree structure ( $\mathcal{T}$ ) with maximally dissimilar molecules at each level is obtained. Hence, each molecule within the tree represents a group of child molecules ( $c_i$ ) subsequently leading to a distinct atom at the bottom of the tree. Following this tree structure from top to bottom results in a fast and robust atom selection approach. For a more detailed description of the actual tree generation

process see Jost et al. (2006).

Algorithm 1 shows our modified TBP approach in pseudocode. While keeping the tree generation algorithm in its original form, we modify and extend the actual matching procedure. To represent GPR data, we incorporate Ricker and Morlet atoms (aside from the original Gabor atoms) into  $\mathcal{D}$ . To further account for phase variations, we make use of the tree structure at the top level. Rather than adding phase variant atoms to  $\mathcal{D}$ , we create a set of phase-shifted signals using

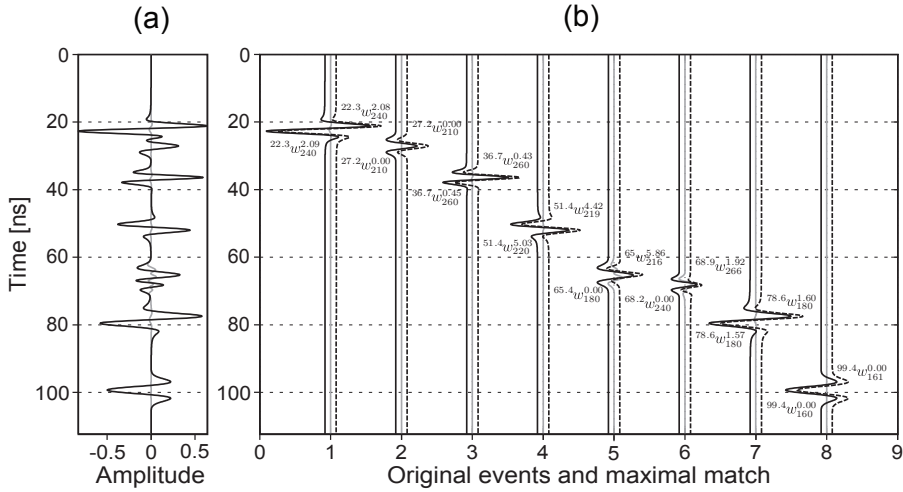
$$\mathcal{F}(f, \theta) = |f_a| \cdot \cos \left[ \arctan \left( \frac{\Im[f_a]}{\Re[f_a]} + \theta \right) \right], \quad (6.3)$$

where  $\theta \in [0, \pi]$  is the phase and  $f_a$  the analytic signal of  $f$ , with its real  $\Re[f_a]$  and imaginary  $\Im[f_a]$  part. At the top tree level, we then select the phase-shifted residual ( $R_{\theta_{opt}}^{(n)} f$ ) with maximum match from the zero-phase dictionary (see Algorithm 1, step 8). For all subsequent matching steps following the tree, we keep the phase-shifted residual selected at the top tree matching step. Iterative calculation of the inner product between the residual ( $R_{\theta_j}^{(n)} f$ ) and translated (translation operator  $T_p$ ) versions of molecules over all positions  $p$  results in a best matching molecule at each level and subsequently in the best matching atom once the bottom of the tree is reached. Finally, we compute the inner product between the phase-shifted residual and the best matching atom (step 15), shift the phase of the scaled atom ( $a_n g_n$ ) by  $-\theta_{opt}$  (step 16), and subtract it from the current residual. We continuously repeat the above steps until we reach our stopping criterion, which is usually a pre-defined energy level of the residual.

## 6.5 Synthetic example

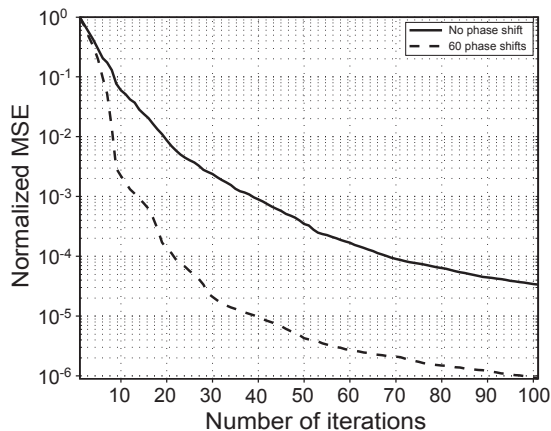
In order to demonstrate the performance of TBP, we generate a synthetic GPR trace composed of eight time shifted, as well as amplitude, frequency, and phase modulated Ricker wavelets. Figure 6.1(a) shows this synthetic trace and the residual after eight iterations ( $R^{(8)} f$ ) using a dictionary of various Ricker atoms and 60 phase shifts between 0 and  $\pi$ . In Figure 6.1(b), we show the individual Ricker wavelets used to generate the synthetic trace and the corresponding matched waveforms. Comparing the characteristic parameters (position, phase, and frequency) of the original and matched waveforms, we observe a high similarity. Only the two events interfering around 65-70 ns show slightly differing values in phase and frequency.

Figure 6.2 illustrates the effect of including phase shifts in the decomposition procedure. For the synthetic GPR trace (Figure 6.1(a)), we compare the normalized Mean Squared Error (MSE) for approximations  $\hat{f}_N$  with and without phase variations included. By including phase information we achieve a faster and better approximation



**FIGURE 6.1.** Decomposition results of a synthetic GPR trace composed of amplitude, frequency, and phase modified Ricker wavelets. (a) Synthetic trace (black) and residual after first eight iterations (gray). (b) Original events (black), first eight waveforms (dotted), and residuals (gray) (time sorted). For each event  $w$  the true and the matched position, its phase, and its frequency ( $Position, w_{Frequency}^{Phase}$ ) are given.

of the synthetic trace. To assess the potential of TBP for spectral decomposition of GPR data, we take a similar approach as Castagna and Sun (2006). We use the synthetic trace shown in Figure 6.1(a) and compare its known true time-frequency plane



**FIGURE 6.2.** Influence of phase variation inclusion on the decomposition results. Solid line (no phase variation included) and dashed line (60 phase shifts between 0 and  $\pi$ ) depict the Mean Squared Error (MSE) of the residual  $R^{(n-1)}f$  at each iteration  $n$ .

(Figure 6.3(b)) with the results of other commonly used methods. As the dominant frequency (peak frequency per time) obtained from the time-frequency representation is a common data attribute, we calculate this attribute for each method. Figure 6.3 shows the results of this comparison. Figures 6.3(c)-6.3(h) illustrate the results obtained using TBP without and with phase information included, STFT with a window length of 25.7 ns, STFT with a window length of 3.7 ns, CWT with a Morlet wavelet, and smoothed WVD. Figures 6.3(e) and 6.3(f) illustrate the common problem of joint time and frequency resolution using STFT. While Figure 6.3(e) closely follows the true frequency behavior, it provides low time localization. For a short

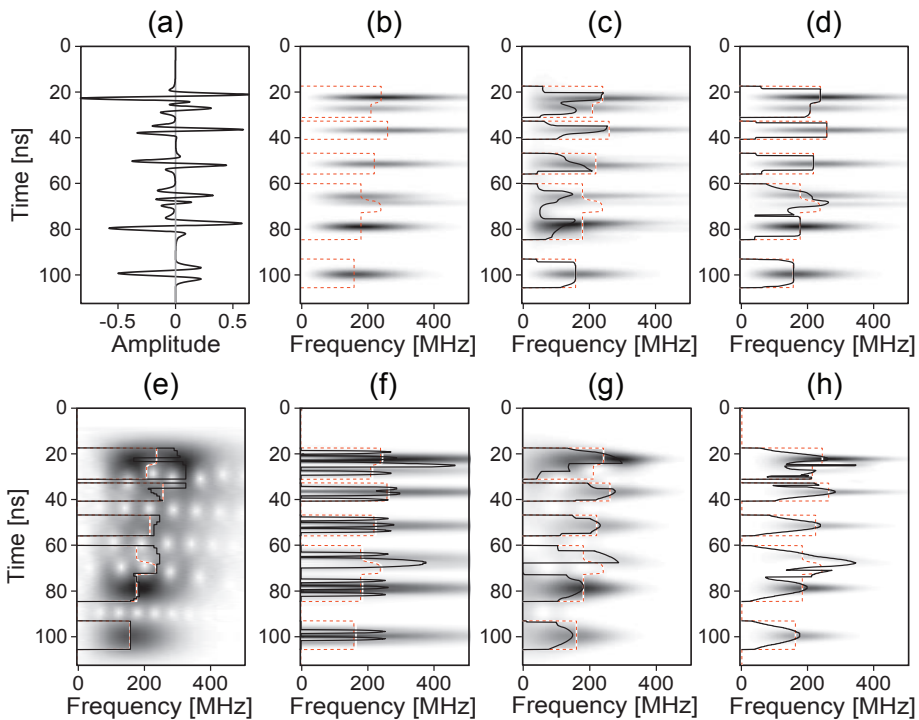


**FIGURE 6.3.** Comparison of selected time-frequency representations. (a) Synthetic trace (black) and residual (gray) from the Tree-Based Pursuit including phase information after 100 iterations. (b) True spectral decomposition. Tree-based pursuit results after 100 iterations (c) without and (d) with phase information included. (e) STFT with a window length of 25.7 ns and (f) a window length of 3.7 ns. (g) CWT using a Morlet wavelet with a scale-frequency relation defined by the wavelet center frequency. (h) Smoothed WVD. In (b)-(h), dotted and black lines illustrate the true and reconstructed dominant frequency behavior with time.

time window (Figure 6.3(f)), there is a high temporal localization but a reduced frequency localization. For the CWT results (Figure 6.3(g)), we converted the scales to pseudo-frequencies using the center frequency of the mother wavelet. The results obtained by the CWT already show an improvement compared to STFT. However, the CWT result lacks an overall high resolution. The smoothed WVD representation in Figure 6.3(h) is characterized by a high variability, probably due to remaining cross terms, which are a well known problem of such energy based methods (e.g., Mallat, 2001).

Comparing the two TBP time-frequency planes (Figures 6.3(c) and 6.3(d)) to the other panels of Figure 6.3, illustrates that both results are characterized by an improved resolution in time and frequency and closely follow the true dominant frequency behavior. Additionally, we notice that neglecting phase variations leads to reduced dominant frequencies compared to the results obtained when including phases. We conclude that phase incorporating TBP provides the highest time-frequency resolution, paired with high computational efficiency.

## 6.6 Field example I: Thin-bed responses

We apply our modified TBP algorithm to real GPR data recorded using 100 MHz antennae in a sand and gravel pit close to Potsdam, Germany. The local geological setting is characterized by a distinct clay layer embedded in sand lithologies. Data processing includes wow and dc removal, amplitude scaling, and migration. Figure 6.4 (top) shows the processed data. The section contains a number of continuous reflections outlining different sedimentary units. The target clay layer is visible between  $\sim 80$  and  $\sim 120$  ns over the entire section. Here, we focus on the end of the section (around inline 20 m) and the interfering events of a potential wedge structure between  $\sim 100$  and  $\sim 150$  ns.

In Figure 6.4, the three lower panels show the time-frequency planes calculated at selected positions A, B, and C between 60 and 180 ns. When comparing the time-frequency planes in Figure 6.4, we observe a significant frequency downshift from trace A to B between  $\sim 100$  and  $\sim 120$  ns. In trace A, two individual events (at  $\sim 100$  and  $\sim 140$  ns) with frequencies of  $\sim 50$  MHz are visible. In trace B, the events cannot be clearly separated from each other due to interference phenomena, and we observe a downshift to  $\sim 40$  MHz at 120 ns. Progressing to trace C, we find no evidence for two individual events and an upshift to  $\sim 60$  MHz. Such frequency effects are typical for thin-bed responses in exploration seismics, and, as illustrated by this example, may help to interpret GPR reflections and thin-bed responses in more detail.



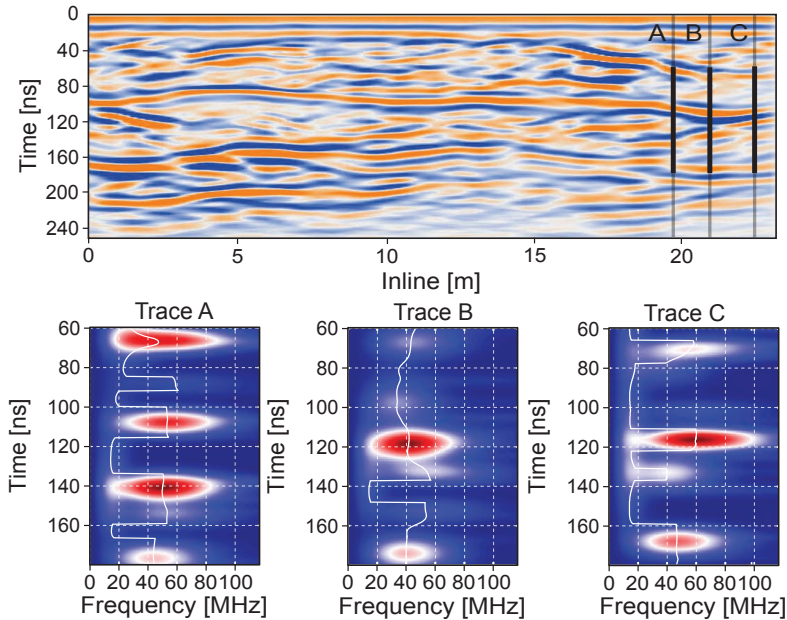


**FIGURE 6.4.** Real GPR data example (top panel). Time-frequency planes (bottom panels) for three selected traces (A, B, and C) calculated from 60-180 ns. The selected traces highlight frequency effects associated with potential thin-bed GPR responses between  $\sim 100$  and  $\sim 150$  ns. The time-frequency planes were normalized to the maximum amplitude within each plane.

## 6.7 Field example II: Enhancing the resolution by atomic frequency modulation

In this section we demonstrate the potential of sparse atomic decompositions for GPR signal processing beyond conventional time-frequency analysis. As demonstrated by Irving and Knight (2003), wavelet dispersion effects caused by frequency-dependent attenuation may decrease resolution with increasing depth. Irving and Knight (2003) address this problem by assuming a linear-downshift model of the dominant frequency variation with increasing depth or traveltime followed by inverse Q-filtering. Aside from the potential removal of constant Q attenuation effects, enhancing the resolution of GPR and seismic data is a topic of general interest. For example, Zhou et al. (2007) presented seismic heterodyning adapted from radio engineering in order to increase resolution of seismic data. Heterodyning relies on the frequency shift theorem of the Fourier transform allowing for shifting the center frequency of signals while preserving the initial bandwidth. Zhou et al. (2007) showed how this property can be used in order to enhance the seismic resolution and to complement deconv-

lution, inverse Q-filtering, or spectral decomposition. Based on the atomic decomposition resulting from tree-based matching pursuit, we demonstrate how atom-based processing prior to reconstruction allows to improve data quality towards higher frequencies.

For this study, we acquired a 200 MHz GPR profile with a length of 98 m at the Horstwalde test site, Germany (see Chapter 5). Processing of the data set consisted of gridding the data onto a 0.15 m inline trace spacing, followed by low frequency wow and dc removal, and simple power law amplitude scaling using an exponent of 2.1. This processing flow efficiently attenuated the airwave which therefore is not visible in the subsequent analyses. Figure 6.5(a) shows the profile and in red its amplitude spectrum after processing. This data set was then decomposed using 90 atoms per trace, 60 different phases between 0 and  $\pi$ , and 350 frequencies ranging between 12.5 and 500 MHz. Wavelet selection was based on a preliminary sparsity study using a test trace, where we found that an optimized Morlet wavelet provided the best approximation rate. In Figure 6.5(b) the reconstruction result is shown. Visually, no obvious difference between the original and the reconstructed data set can be found. Figure 6.5(c) shows the residual between the input and reconstructed data. All data sets are plotted at an equal scale but the residual was amplified by a factor of ten in order to highlight minor differences. Some individual traces (e.g., around 70 m inline coordinate) show a distinct amount of high-frequency which is related to a larger amount of noise at these locations. Here, the matching process was less efficient and more atoms would have been required to further reduce the remaining energy. Furthermore, the residual section (Figure 6.5(c)) shows a remaining low frequency component as evident in the corresponding noise spectrum. This is related to the fact that the dictionary was limited to reasonable frequencies ranging from 12.5 to 500 MHz. Thus, the visible low frequency effect cannot be reconstructed and thus is effectively filtered out. We see that we achieve an excellent reconstruction of the subsurface reflected GPR signals is achieved by using 90 atoms per trace.

Given the sparse decomposition and the capability to access individual waveform properties such as frequency and phase, this allows for modulation of the waveforms prior to the reconstruction process. Figure 6.6(a) and 6.6(b) show the reconstructed data set and its average time-frequency distribution calculated from the first (dominant) five atoms of each trace. Here, the red line indicates the mean frequency over discrete bins interpolated over all time samples. Aside from a high frequency peak around 40 ns, a clear high-frequency attenuation below 120 ns is observed. We now seek to flatten the average time-frequency behavior and improve the resolution of late arrivals by modulating the frequencies before reconstruction. To achieve this goal, we flatten the time-frequency distribution to a desired frequency level  $f_m$ . The corresponding frequency correction function  $f_c(p)$ , which is used to modulate the

frequency content at each position is calculated by

$$f_c(p) = f_m - \bar{f}^*(p). \quad (6.4)$$

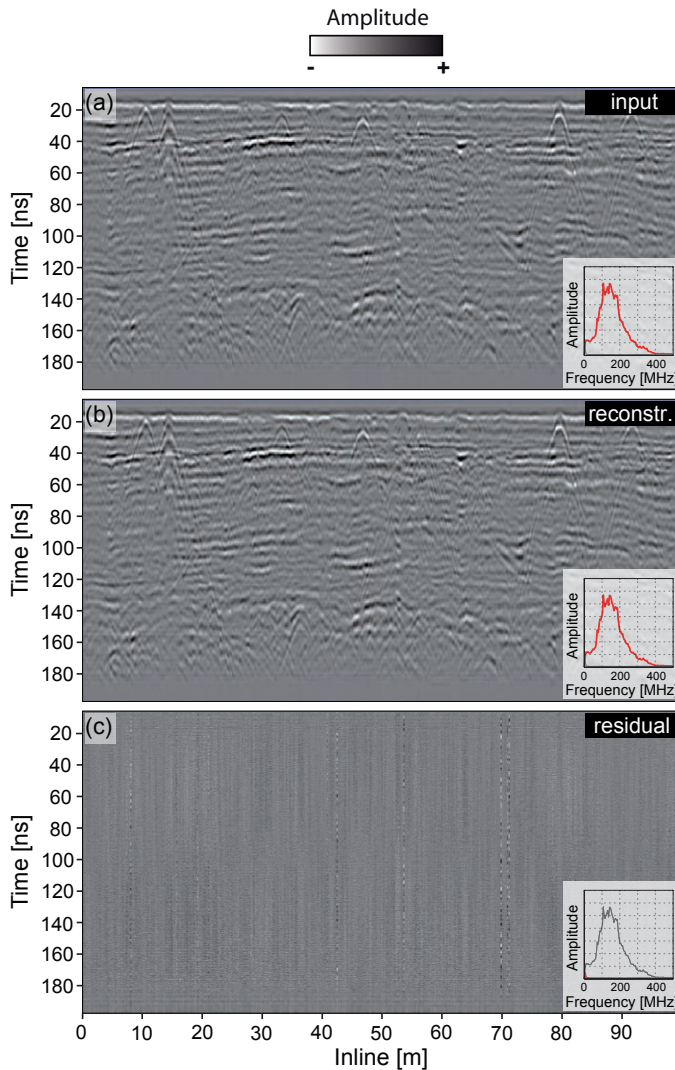


**FIGURE 6.5.** Decomposition of a 200 MHz GPR profile. (a) original input data set. (b) reconstruction using 90 atoms (9% of the data) including 60 phases. (c) residual (input minus reconstruction) 10 times amplified to highlight minor variations. Input and reconstructed data were plotted on an equal scale. The average trace spectrum for each section is shown as red lines. The spectrum of (c) only shows very small amplitudes at low frequencies.

$\bar{f}^*(p)$  is obtained by running average filtering (window of 8 ns) of the dominant frequency over depth ( $\bar{f}(p)$ ), shown in red in Figure 6.6(b)), which is calculated from the first five atoms of each trace. In Figure 6.6, the averaged dominant frequency can be further evaluated by the variation of peak energy in the time-frequency density plot shown in gray scale. Based on the frequency modulation defined in Equation 6.4, we modify the frequency content of the individual atoms at each position (time) to enhance the resolution of the resulting reconstruction. The frequency modulated

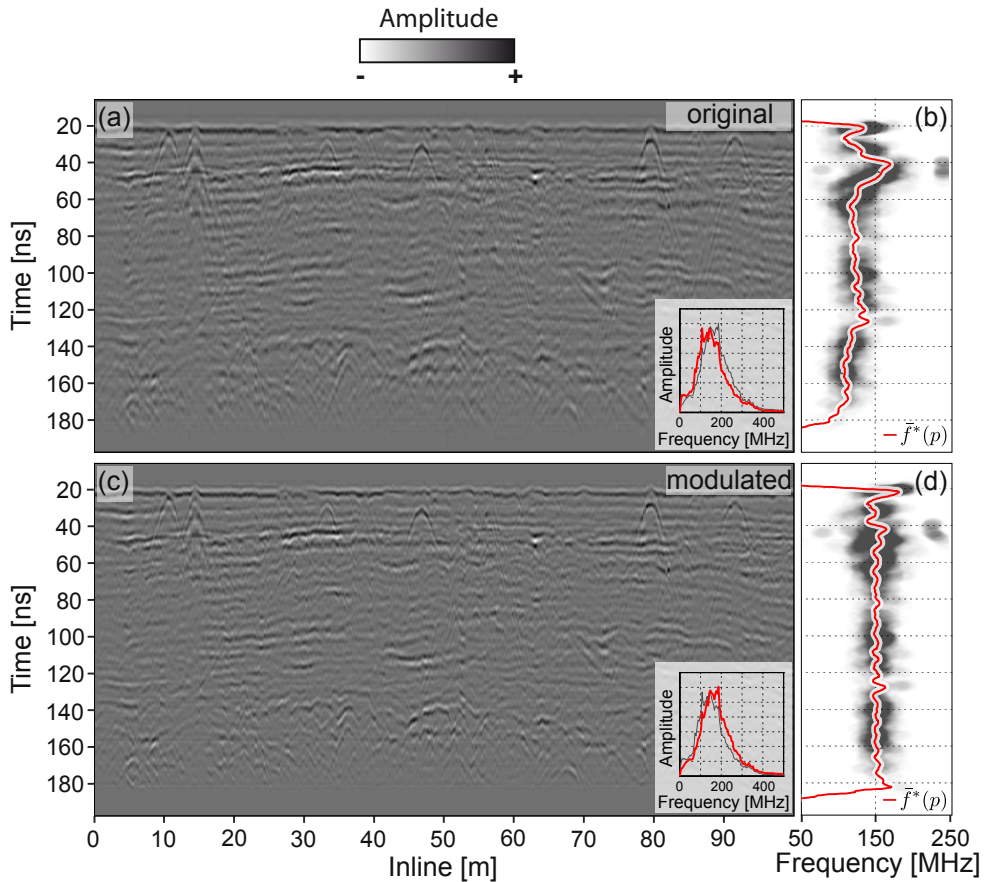


**FIGURE 6.6.** Enhancing the resolution by atomic frequency modulation. (a) original data set with its amplitude spectrum given in red. (b) time-frequency distribution of the five dominant atoms over all traces. In red, the average frequency per time instance is shown. (c) data set after frequency modulation with its amplitude spectrum shown in red. (d) time-frequency distribution after atomic frequency modulation has been performed. The procedure successfully flattens the average time-frequency distribution and results in a clear enhancement of late arrivals.

atom at position  $p$  is thus defined by

$$w(p, \theta, f_m) = w(a, p, \theta, f + f_c(p)). \quad (6.5)$$

Keeping the amplitude  $a$ , the position  $p$ , and the phase  $\theta$  fixed, this allows to efficiently modulate the frequency content of our reconstruction. Figure 6.6(c) shows our result, i.e., our data set after frequency modulation. Inspection of the time-frequency distribution in Figure 6.6(d) illustrates the success of our modulation. The frequencies are flattened around 150 MHz corresponding to the maximum desired frequency. The spectra in Figure 6.6 show the frequency shift obtained by the proposed procedure. In red the spectrum of the shown data set is given, while in light gray the one of the other data set is given for reference. Comparing the original and modulated data set, we clearly see how resolution is improved, especially beyond  $\sim 100$  ns. Reflections interfering within the original data set can be clearly separated in the modulated reconstruction. Thus, our procedure provides an efficient and flexible way to enhance GPR data considering a successful sparse decomposition of the recorded data set.

## 6.8 Conclusions

We presented a novel approach to spectral decomposition based on Tree-Based Pursuit (TBP). Our method provides high-resolution time-frequency representations of GPR data. In addition, we included phase variations into the decomposition procedure, which resulted in more confident time-frequency analyses compared to zero-phase decomposition approaches. The proposed phase incorporation makes use of the tree structure and allows to include a high number of phase shifts in the actual matching algorithm at a minor increase in computational cost. Apart from the application to spectral decomposition our modified TBP also allows for nonlinear filtering (such as denoising) based on its ability to efficiently represent the underlying signal characteristics. We have demonstrated the applicability and potential of the Tree-Based Pursuit method in GPR studies based on synthetic and real data examples. We successfully demonstrated how modulation of the atoms allows to effectively improve the resolution or compensate for potential frequency attenuation effects found at late arrivals. Since the decomposition result can be regarded as a result of a deconvolution routine, we could use our procedure to improve or even replace other deconvolution schemes. Future research will also study the possibility to decompose multiple signals at once. This would be an interesting new approach considering the amount of information that could be obtained by analyzing multiple data sets, such as multi-component or multi-frequency, simultaneously. Additionally, the possibility to formulate matching pursuit in a parallel fashion, which would allow for real-time sparse decompositions, has just recently been presented. From our point of view, this

would be another factor making sparsity promoting greedy algorithms more interesting also to the GPR community.

## **6.9 Acknowledgments**

We gratefully acknowledge financial support by the German Research Foundation (DFG, grant TR512/2-1). Especially we would like to thank P. Jost, EPFL Lausanne, for making his Tree-Based Pursuit algorithm available to the scientific community.

# GENERAL CONCLUSIONS AND PERSPECTIVES

---

In this thesis, I studied two topics dealing with high-precision kinematic data acquisition and attribute-based data analyses applied to GPR. Modern GPR provide the technical mean in order to acquire high-resolution subsurface images. In the following, I will summarize the results of the underlying thesis and the potential for prospective work.

The first objective of this thesis was the implementation and evaluation of a flexible and accurate surveying setup allowing for real-time kinematic GPR data acquisition. Considering the practical limitations inherent to real-time kinematic surveying approaches, namely the positioning precision and/or the technical implementation, I have evaluated the potential of modern tracking total stations (TTS) for high-precision, real-time kinematic GPR surveying.

- Based on the availability of Pseudo-NMEA, GPS-like, coordinate output provided by modern TTS systems, the wide-spread possibility to attach GPS systems to geophysical instruments, and radio-based wireless data transmission, I have introduced a flexible real-time kinematic GPR surveying setup. In order to evaluate the potential of TTS-based kinematic data acquisition, the major influences on data quality were investigated; i.e., system cross-talk and systematic latency. Experimental studies on the signal-to-noise ratio variation at increasing TTS-GPR offsets, with and without radio communication (using different modem gains), showed that by respecting a minimum distance of  $\sim 5$  m to the TTS, the signal-to-noise ratio is equal to the one without using radio communication. To assess the accuracy of the system for real-time kinematic data acquisition, latency (i.e., the temporal delay between a signal being acquired and its availability to the data logger) have been studied. Repetitive acquisition of a profile in forward- and reverse-manner highlights the influence of latency on the actual positioning accuracy and the importance of its correction. Successful estimation of the setup-dependent gross latency subsequently allows for correction of the acquired positional data to obtain high-precision

GPR data. I have presented an estimation procedure based on iterative coordinate correction based on interpolation of the positional data using steadily increasing latency times, followed by assessing profile alikeness using a recently introduced image quality measure, namely the MSSIM index. The shown latency estimation and correction strategy thereby provides a successful mean to correct geophysical data fused in real-time. Taking the aforementioned issues into account, TTS-based surveying allows for geophysical data acquisition at a high positional accuracy, at a minimal financial and methodological cost. The presented surveying solution has been successfully applied to other geophysical surveying methods conducted within the Applied Geophysics group at the University of Potsdam. Numerous case studies affirmed the flexibility and practicability of this setup for near-surface geophysical data acquisition.

Traditionally, 3D GPR data interpretation is limited to the visual inspection of migrated data sets (such as time slice displays). Nevertheless, similar to industry quality seismic data sets, 3D GPR data offer significant room for attribute-based analyses, enhancing specific information and thereby reducing the interpretational complexity. Compared to seismic data sets mostly sampling the undisturbed subsurface, GPR data are often characterized by a significant degree of complexity introduced through anthropogenic disturbances.

- On the basis of two archaeological studies, I have demonstrated the feasibility of attribute-based processing to problems differing from the geological ones faced by the seismic community. As demonstrated, the application of similarity and coherency to archaeological data sets allows for a significantly improved interpretation of 3D GPR data sets to, first, isolate the features of interest and, second, enhance relevant features hidden in the complexity of migrated data sets. I have further shown how combination of GPR, magnetic, and topographic data into composite images, where each data set is assigned to an individual color channel, allows for highlighting the complementary nature of multi-method data sets. Consequently, composite images of multiple near-surface data sets results in more comprehensive interpretations of the underlying database including all aspects of the data at hand.

Site characterization based on 3D single- and multi-component GPR data has become increasingly important, especially in the context of subsurface utility detection. Subsurface electromagnetic scattering at man-made utilities often exhibits characteristic polarization effects. Governed by the geometrical and physical properties of the target features and the host material differing degrees of polarization might occur. In this thesis, I have presented a novel processing approach focusing on the extraction and characterization of subsurface utility pipes.



- Based on the common symmetric nature of installed subsurface utilities, I introduced a novel feature extraction algorithm based on feature symmetry, originally developed within the image processing community. Attenuating the geological GPR response using Laplacian highboosting significantly enhances the response of utilities embedded in 3D data sets. Subsequent application of the phase symmetry algorithm has shown to allow for efficient extraction of the target features from large 3D data volumes. In addition to the geometrical properties, I extracted the physical polarization characteristics using a windowed principle component analysis (PCA) and the associated attributes linearity and polarization angle. Combining polarization and feature angle, leads to a novel attribute called depolarization. Depolarization allows for efficient characterization of subsurface utilities based on their joint geometrical and physical (polarization) characteristics. Evaluating the proposed attributes on synthetic data has illustrated the potential of such an approach to significantly enhance utilities found in 3D GPR data also from heterogeneous sites. Based on a dual-component 3D field data set and ground-truth data I have successfully shown how depolarization allows for polarization-based distinction between clay and metallic utility pipes extracted by the improved symmetry algorithm. Given the continuously growing development of multi-component GPR systems, I believe that efficient strategies making use of the polarization phenomenon are becoming more and more important. The attractiveness of the proposed polarization attribute is certainly based on its efficiency and the potential for automatic analyses. The next logical step would be the inclusion of cross-polarized antennae configurations in order to complement the information of the vectorial electromagnetic wavefield.

High-resolution time-frequency analyses of reflection seismic data have proven to pose a significant interpretational potential, especially, considering thin-bed tuning effects. So far, high-resolution time-frequency analysis applied to GPR studies has predominantly been limited to the detection of dense non aqueous phase liquids (DNAPLs) or thin-bed tuning studies. Nevertheless, especially high-resolution sparse decompositions, such as provided by matching pursuit methods, offer manifold alternative applications. In the following, I will highlight my current and prospective work in this field.

- Within the course of this thesis, I have introduced a modified tree based matching pursuit approach. Matching pursuit is well known to provide the highest time-frequency resolution of all currently available methods. Given its high computational cost, traditional matching pursuit methods are often impracticable for the analysis of large-scale 3D data volumes. Based on a pre-calculated tree structure, I generalized the decomposition step in such a way that phase

variation is not embedded into the waveform dictionary itself, but rather imposed on the residual waveform through Hilbert-based phase rotations. Iterative selection of the best matching atom from a suite of phase-shifted residual waveforms therefore allows for introduction of various waveforms also ones for which phase shifts are mathematically not clearly defined. Application of the algorithm to a data set composed of thin-bed tuning effects has demonstrated to provide a time-frequency resolution beyond the one obtained by conventional time-frequency decomposition algorithms. Apart from time-frequency analysis, sparse decomposition of the data allows for advanced processing and analysis of the decomposed signal. I have shown how modulation of the wavelet properties at an atomic level can be used to efficiently enhance the resolution or compensate for potential frequency attenuation effects before data reconstruction. Future work will focus on the extension of the algorithm to allow for decomposition of multiple data sets (e.g., multi-component or multi-frequency GPR data) in a sequential manner based on a priori signal fusion. The individually decomposed signals might then allow for novel processing approaches through the combination of multi-frequency data sets, i.e., their decompositions.

This thesis has been focusing on the evaluation and development of attribute processing strategies tailored to GPR data sets and problems. I have shown how attributes significantly improve the interpretability of GPR data, considering typical applications, such as archaeology and utility detection. Considering the success of attribute-driven parameter estimation in the field of reservoir characterization, I believe that similarly GPR holds a lot of potential for assessing relationships between for example hydrological and engineering parameter variations (for example known from borehole or direct-push testing) and GPR attributes. This would be a major step towards quantitative high-resolution 3D characterization of near-surface environments, required in various fields of application.

# REFERENCES

---

- Aaltonen, J., and J. Nissen, 2002, Geological mapping using GPR and differential GPS positioning - a case study: , International Society for Optical Engineering, 207–210.
- Al-Nuaimy, W., Y. Huang, M. Nakhkash, M. T. C. Fang, V. T. Nguyen, and A. Eriksen, 2000, Automatic detection of buried utilities and solid objects with GPR using neural networks and pattern recognition: *Journal of Applied Geophysics*, **43**, 157–165.
- Annan, A. P., 2005, GPR methods for Hydrogeological Studies, *in* *Hydrogeophysics*: Springer, volume **50** of *Water Science and Technology Library*, 185–213.
- Annan, A. P., and J. L. Davis, 1997, Ground Penetrating Radar Coming of Age at Last !!: *Proceeding of Exploration 97: Fourth Decennial International Conference on Mineral Exploration*, 515–522.
- Bahorich, M. S., and S. L. Farmer, 1995, 3-D Seismic discontinuity for faults and stratigraphic features: The coherence cube: *The Leading Edge*, **14**, 1053–1058.
- Balch, A. H., 1971, Color sonograms: a new dimension in seismic data interpretation: *Geophysics*, **36**, 1074–1098.
- Barratt, G., V. Gaffney, H. Goodchild, and S. Wilkes, 2000, Survey at Wroxeter using carrier phase, differential GPS surveying techniques: *Archaeological Prospection*, **7**, 133–143.
- Beres, M., P. Huggenberger, A. G. Green, and H. Horstmeyer, 1999, Using two- and three-dimensional georadar methods to characterize glaciofluvial architecture: *Sedimentary Geology*, **129**, 1–24.
- Bergmann, T., J. O. Blanch, J. O. A. Robertsson, and K. Holliger, 1999, A simplified Lax-Wendroff correction for staggered grid FDTD modeling of electromagnetic wave propagation in frequency-dependent media: *Geophysics*, **64**, 1369–1377.
- Bergstedt, C., H.-D. Heimann, and H. Krohm, 2009, *Bischofsresidenz Burg Ziesar und ihre Kapelle*: Bebra.
- Böniger, U., and J. Tronicke, 2010a, Improving the interpretability of 3D GPR data using target-specific attributes: Application to tomb detection: *Journal of Archaeological Science*, **37**, 672–679.

- , 2010b, On the potential of kinematic GPR surveying using a self-tracking total station: Evaluating system cross-talk and latency: *IEEE Transactions on Geoscience and Remote Sensing*, **48**, 3792–3798.
- Bouvet, D., and G. Garcia, 2000, Improving the accuracy of dynamic localization systems using RTK GPS by identifying the GPS latency: Presented at the Proceedings of the 2000 IEEE.
- Bradford, J. H., and Y. Wu, 2007, Instantaneous spectral analysis: Time-frequency mapping via wavelet matching with application to contaminated-site characterization by 3D GPR: *The Leading Edge*, **26**, 1018–1023.
- Bristow, C. S., and H. M. Jol, 2003, Ground penetrating radar in sediments: Special Publication: No. 211: Geological Society, London.
- Brown, A. R., 2004, Interpretation of Three-Dimensional Seismic Data, 6 ed.: American Association of Petroleum Geologists.
- Burrough, A. P., and R. A. McDonnell, 1998, Principle of Geographical Information Systems: Oxford University Press.
- Butler, D. K., 2005, Near-Surface Geophysics: Investigations in Geophysics No. 13: Society of Exploration Geophysicists.
- Büyüksarac, A., M. O. Arisoy, O. Bektascedil, O. Kocak, and T. Cay, 2008, Determination of grave locations in Dedemezari Necropolis (Western Turkey) using magnetic field derivatives: *Archaeol. Prosp.*, **15**, 267–283.
- Castagna, J. P., and S. Sun, 2006, Comparison of spectral decomposition methods: *First Break*, **24**.
- Chakraborty, A., and D. Okaya, 1995, Frequency-time decomposition of seismic data using wavelet-based methods: *Geophysics*, **60**, 1906–1916.
- Chopra, S., and K. J. Marfurt, 2007, Seismic attributes for prospect identification and reservoir characterization: *Geophysical Developments No. 11*: Society of Exploration Geophysicists.
- Chopra, S., and S. Pickford, 2001, Integrating coherence cube imaging and seismic inversion: *The Leading Edge*, **20**, 354–362.
- Conyers, L. B., 2004, Ground-penetrating radar for archaeology: Rowman & Littlefield.
- Cooper, G. R. J., and D. R. Cowan, 2006, Enhancing potential field data using filters based on the local phase: *Computer & Geosciences*, **32**, 1585–1591.
- Czarnowski, J., S. Geibler, and A. Kathage, 1996, Combined Investigation of GPR and High Precision Real-Time Differential GPS: Proceedings of the Sixth International Conference on Ground Penetrating Radar, 207–209.
- Dabas, M., C. Camerlynck, and P. F. I. Camps, 2000, Simultaneous use of electrostatic quadrupole and GPR in urban context: Investigation of the basement of the Cathedral of Girona (Catalunya, Spain): *Geophysics*, **65**, 526–532.
- Daniels, D., 2004, Ground penetrating radar, 2 ed.: The Institution of Engineering

- and Technology, London. IET Radar, Sonar, Navigation and Avionics Series 15.
- de Rooij, M., and K. Tingdahl, 2002, Meta-attributes—The key to multivolume, multiattribute interpretation: *The Leading Edge*, **21**, 1050–1053.
- Dimc, F., B. Music, and R. Osredkar, 2006, Attaining Required Positioning Accuracy in Archeo-Geophysical Surveying by GPS: 12th International Power Electronics and Motion Control Conference, 2037–2040.
- Drahor, M. G., 2006, Integrated geophysical studies in the upper part of Sardis archaeological site, Turkey: *Journal of Applied Geophysics*, **59**, 205–223.
- Farzadi, P., and J. Hestharnmer, 2007, Diagnosis of the Upper Cretaceous palaeokarst and turbidite systems from the Iranian Persian Gulf using volume-based multiple seismic attribute analysis and pattern recognition: *Petroleum Geoscience*, **13**, 227–240.
- Field, D. J., 1987, Relations between the statistics of natural images and the response properties of cortical cells: *Journal of the Optical Society of America A: Optics, Image Science, and Vision*, **4**, 2379–2394.
- Flinn, E. A., 1965, Signal analysis using rectilinearity and direction of particle motion: *Proceedings of the IEEE*, **53**, 1874–1876.
- Francese, R. G., E. Finzi, and G. Morelli, 2009, 3-D high-resolution multi-channel radar investigation of a Roman village in Northern Italy: *Journal of Applied Geophysics*, **67**, 41–51.
- Francke, J., and V. Utsi, 2009, Advances in long-range GPR systems and their applications to mineral exploration, geotechnical and static correction problems: *First Break*, **27**, 85–93.
- Gaffney, C., V. Gaffney, R. Cuttler, and R. Yorston, 2008, Initial results using GPS navigation with the Foerster magnetometer system at the World Heritage site of Cyrene, Libya: *Archaeological Prospection*, **15**, 151–156.
- Gámez, A. J., C. S. Zhou, A. Timmermann, and J. Kurths, 2004, Nonlinear dimensionality reduction in climate data: *Nonlinear Processes in Geophysics*, **11**, 393–398.
- Geerdes, I. C., and R. A. Young, 2007, Spectral decomposition of 3D ground-penetrating radar data from an alluvial environment: *The Leading Edge*, **26**, 1024–1030.
- Gersztenkorn, A., and K. J. Marfurt, 1999, Eigenstructure-based coherence computations as an aid to 3-D structural and stratigraphic mapping: *Geophysics*, **64**, 1468–1479.
- Gestel, J. P. V., and P. L. Stoffa, 2001, Application of Alford rotation to ground-penetrating radar data: *Geophysics*, **66**, 1781–1792.
- Giannopoulos, A., 2005, Modeling of ground penetrating radar by GprMax: *Construction and Building Materials*, **19**, 755–762.
- Gonzalez, R. C., and R. E. Woods, 2002, *Digital Image Processing (2nd Edition)*:

- Prentice Hall.
- Goodman, D., and Y. Nishimura, 1993, Ground radar view of Japanese burial mounds: *Antiquity*, **67**, 349–354.
- Gracia, V. P., J. A. Canas, L. G. Pujades, J. Clapes, O. Caselles, F. Garcia, and R. Osorio, 2000, GPR survey to confirm the location of ancient structures under the Valencian Cathedral (Spain): *Journal of Applied Geophysics*, **43**, 167–174.
- Grandjean, G., J. Gourry, and A. Bitri, 2000, Evaluation of GPR techniques for civil-engineering applications: study on a test site: *Journal of Applied Geophysics*, **45**, 141–156.
- Grasmueck, M., and D. A. Viggiano, 2007, Integration of Ground-Penetrating Radar and Laser Position Sensors for Real-Time 3-D Data Fusion: *IEEE Transactions on Geoscience and Remote Sensing*, **45**, 130–137.
- Grasmueck, M., R. Weger, and H. Horstmeyer, 2005, Full-resolution 3D GPR imaging: *Geophysics*, **70**, K12–K19.
- Gross, R., A. G. Green, H. Horstmeyer, and J. H. Begg, 2004, Location and geometry of the Wellington Fault (New Zealand) defined by detailed three-dimensional georadar data: *Journal of Geophysical Research*, **109**, 1–14.
- Guo, H., S. Lewis, and K. J. Marfurt, 2008, Mapping multiple attributes to three- and four-component color models – A tutorial: *Geophysics*, **73**, W7–W19.
- Hampson, D. P., J. S. Schuelke, and J. A. Quirein, 2001, Use of multiattribute transforms to predict log properties from seismic data: *Geophysics*, **66**, 220–236.
- Hart, B. S., and R. S. Balch, 2000, Approaches to defining reservoir physical properties from 3-D seismic attributes with limited well control: An example from the Jurassic Smackover Formation, Alabama: *Geophysics*, **65**, 368–376.
- Heincke, B., A. G. Green, J. van der Kruk, and H. Horstmeyer, 2005, Acquisition and processing strategies for 3D georadar surveying a region characterized by rugged topography: *Geophysics*, **70**, K53–K61.
- Henderson, J., S. Purves, G. Fisher, and C. Leppard, 2008, Delineation of geological elements from RGB color blending of seismic attribute volumes: *The Leading Edge*, **27**, 342–350.
- Hill, I., T. Grossey, and C. Leech, 2004, High-resolution multisensory geophysical surveys for near-surface applications can be rapid and cost-effective: *The Leading Edge*, **23**, 684–688.
- Holliger, K., B. Lampe, U. Meier, M. Lambert, and A. G. Green, 2003, Realistic modeling of surface ground-penetrating radar antenna systems: where do we stand?: *Proceedings of the 2nd International Workshop on Ground Penetrating radar*, 45–50.
- Huang, T. S., J. W. Burnett, and A. G. Deczky, 1975, The importance of phase in image processing filters: *IEEE Transactions on Acoustics, Speech, and Signal Processing*, **23**, 529–542.

- Hugenschmidt, J., and A. Kalogeropoulos, 2009, The inspection of retaining walls using GPR: *Journal of Applied Geophysics*, **67**, 335–344.
- Hyndmann, D., and J. Tronicke, 2005, Hydrogeophysical case studies in the saturated zone, *in* *Hydrogeophysics: Springer, volume 50 of Water Science and Technology Library*, 391–412.
- Ingensand, H., and W. Stempfhuber, eds., 2008, *The Kinematic Potential of Modern Tracking Total Stations - A state of the Art Report on the Leica TPS1200+*: Proceedings of the 1st International Conference on Machine Control & Guidance.
- Irving, J. D., and R. J. Knight, 2003, Removal of wavelet dispersion from ground-penetrating radar data: *Geophysics*, **68**, 960–970.
- Jol, H. M., 2009, *Ground Penetrating Radar: Theory and Applications*: Elsevier.
- Jolliffe, I. T., 2002, *Principal Component Analysis*, 2 ed.: Springer.
- Jones, D. M., 2008, *Geophysical Survey in Archaeological Field Evaluation*.
- Jost, P., P. Vandergheynst, and P. Frossard, 2006, Tree-based pursuit: Algorithm and Properties: *IEEE Transactions on Signal Processing*, **54**, 4685–4697.
- Kadkhodaie-Ilkhchi, A., M. R. Rezaee, and H. Rahimpour-Bonab, 2009, Petrophysical data prediction from seismic attributes using committee fuzzy inference system: *Computers & Geosciences*, **35**, 2314–2330.
- Kaplan, E. D., 1996, *Understanding GPS Principles and Applications*: Artech House Publishers.
- Karlsen, B., J. Larsen, H. B. D. Sorensen, and K. B. Jakobsen, 2001, Comparison of PCA and ICA based clutter reduction in GPR systems for anti-personal landmine detection: *Proc. 11th IEEE Workshop Stat. Signal Process.*, 146–149.
- Kashihara, K., and T. Tsuji, 2010, Improvement in facies discrimination using multiple seismic attributes for permeability modelling of the Athabasca Oil Sands, Canada: *Exploration Geophysics*, **41**, 80–87.
- Keay, S., G. Earl, S. Hay, S. Kay, J. Ogden, and K. D. Strutt, 2009, The role of integrated geophysical survey methods in the assessment of archaeological landscapes: the case of Portus: *Archaeological Prospection*, **16**, 154–166.
- Knight, R. J., 2001, *Ground Penetrating Radar for Environmental Applications: Annual Review of Earth and Planetary Sciences*, **29**, 229–255.
- Koppenjan, S., 2009, *Ground Penetrating Radar Systems and Design*, *in* *Ground Penetrating Radar: Theory and Applications*: Elsevier, 73–97.
- Kovesi, P. D., 1996, *Invariant Measures of Image Features From Phase Information*: PhD thesis, University of Western Australia.
- , 1997, Symmetry and asymmetry from local phase: Tenth Australian Joint Conference on Artificial Intelligence, 185–190.
- , 1999, Image Features From Phase Congruency: *Videre: A Journal of Computer Vision Research*, **1**, 1–26.
- Kvamme, K. L., E. G. Ernenwein, and C. J. Markussen, 2006, *Robotic Total Sta-*

- tion for Microtopographic Mapping: an Example from the Northern Great Plains: Archaeological Prospection, **13**, 91–102.
- Lambot, S., A. Binley, E. Slob, and S. Hubbard, 2008, Ground Penetrating Radar in Hydrogeophysics: Vadose Zone Journal, **7**, 137–139.
- Lehmann, F., D. Boerner, K. Holliger, and A. Green, 2000, Multicomponent georadar data: Some important implications for data acquisition and processing: Geophysics, **65**, 1542–1552.
- Lehmann, F., and A. G. Green, 1999, Semiautomated georadar data acquisition in three dimensions: Geophysics, **64**, 719–731.
- , 2000, Topographic migration of georadar data: Implications for acquisition and processing: Geophysics, **65**, 836–848.
- Lemmon, T. R., and G. P. Gerdan, 1999, The Influence of the Number of Satellites on the Accuracy of RTK GPS Positions: Australian surveyor, **44**.
- Leucci, G., and S. Negri, 2006, Use of ground penetrating radar to map subsurface archaeological features in urban area: Journal of Archaeological Science, **33**, 502–512.
- Liu, J., and K. J. Marfurt, 2005, Matching pursuit decomposition using Morlet wavelets: 75th International Meeting, SEG, Expanded Abstracts, 786–789.
- , 2007, Instantaneous spectral attributes to detect channels: Geophysics, **72**, P23–P31.
- Loughridge, J. R., 1998, Application of Seismic Tools and Techniques to Ground-Penetrating Radar (GPR) Studies: Thesis, Rice University.
- Luo, Y., S. Al-Dossary, M. Marhoon, and M. Alfaraj, 2003, Generalized Hilbert transform and its applications in geophysics: The Leading Edge, **22**, 198–202.
- Mahob, P. N., and J. P. Castagna, 2002, AVO hodograms and polarization attributes: The Leading Edge, **21**, 18–27.
- Maisano, D. A., J. Jamshidi, F. Franceschini, P. G. Maropoulos, L. Mastrogiacomo, A. R. Mileham, and G. W. Owen, 2008, Indoor GPS : system functionality and initial performance evaluation: International Journal of Manufacturing Research, **3**, 335–349.
- Mallat, S. G., 2001, A wavelet tour of signal processing: Academic Press.
- Mallat, S. G., and Z. Zhang, 1993, Matching pursuits with time-frequency dictionaries: Signal Processing, IEEE Transactions, **41**, 3397–3415.
- Marfurt, K. J., R. L. Kirlin, S. L. Farmer, and M. S. Bahorich, 1998, 3-D seismic attributes using a semblance-based coherency algorithm: Geophysics, **63**, 1150–1165.
- Mari, J.-L., and D. Chapellier, 1999, Reservoir And Civil Engineering Geophysics: Technip Editions.
- McClymont, A. F., A. G. Green, R. Streich, H. Horstmeyer, J. Tronicke, D. C. Nobes, J. Pettinga, J. Campbell, and R. Langridge, 2008, Visualization of active faults



- using geometric attributes of 3D GPR data: An example from the Alpine Fault Zone, New Zealand: *Geophysics*, **73**, B11–B23.
- McMahon, W., M. H. Burtwell, and M. Evans, 2005, Minimising street work disruption: the real costs of street works to the utility industry and society: Presented at the UKWIR report 05 / WM / 12 / 8, UK Water Industry Research.
- Mellett, J. S., 1995, Ground penetrating radar applications in engineering, environmental management, and geology: *Journal of Applied Geophysics*, **33**, 157–166.
- Miller, H. G., and V. Singh, 1994, A new concept for location of potential field sources: *Journal of Applied Geophysics*, **32**, 213–217.
- Moran, M. L., R. J. Greenfield, S. A. Arcone, and A. J. Delaney, 2000, Delineation of a complexly dipping temperate glacier bed using short-pulse radar arrays: *Journal of Glaciology*, **46**, 274–286.
- Morrone, M. C., and R. A. Owens, 1987, Feature detection from local energy: *Pattern Recognition Letters*, **6**, 303–313.
- Neal, A., 2004, Ground-penetrating radar and its use in sedimentology: principles, problems and progress: *Earth-Science Reviews*, **66**, 261–330.
- Ng, W., T. C. T. Chan, H. C. So, and K. C. Ho, 2008, Particle Filtering Based Approach for Landmine Detection Using Ground Penetrating Radar: *IEEE Transactions on Geoscience and Remote Sensing*, **46**, 3739–3755.
- Nuzzo, L., G. Leucci, S. Negri, M. T. Carozzo, and T. Quarta, 2002, Application of 3D visualization techniques in the analysis of GPR data for archaeology: *Annals of Geophysics*, **45**, 321–337.
- Onishi, K., T. Yokota, S. Maekawa, T. Toshioka, and S. Rokugawa, 2005, Highly efficient CMP surveying with ground-penetrating radar utilising real-time kinematic GPS: *Expl. Geophys.*, **36**, 59–66.
- Orlando, L., and E. Slob, 2009, Using multicomponent GPR to monitor cracks in a historical building: *Journal of Applied Geophysics*, **67**, 327–334.
- Paoletti, V., M. Secomandi, M. Piromallo, F. Giordano, M. Fedi, and A. Rapolla, 2005, Magnetic Survey at the Submerged Archaeological Site of Baia, Naples, Southern Italy: *Archaeological Prospection*, **12**, 51–59.
- Pereira, J. E. D., A. J. Strieder, J. P. Amador, J. L. S. da Silva, and L. L. V. Volcato, 2010, A heuristic algorithm for pattern identification in large multivariate analysis of geophysical data sets: *Computers & Geosciences*, **36**, 83–90.
- Piro, S., P. Mauriello, and F. Cammarano, 2000, Quantitative integration of geophysical methods for archaeological prospection: *Archaeol. Prosp.*, **7**, 203–213.
- Piro, S., D. Peloso, and R. Gabrielli, 2007, Integrated Geophysical and Topographic Investigation in the Territory of Ancient Tarquinia (Viterbo, Central Italy): *Archaeological Prospection*, **14**, 191–201.
- Pohl, C., and J. L. van Genderen, 1998, Multisensor image fusion in remote sensing: concepts, methods and applications: *International Journal of Remote Sensing*, **19**,

- 823–854.
- Porsani, J. L., E. Slob, R. S. Lima, and D. N. Leite, 2010, Comparing detection and location performance of perpendicular and parallel broadside GPR antenna orientations: *Journal of Applied Geophysics*, **70**, 1–8.
- Qu, S. L., Y. X. Ji, X. Wang, C. Xinrong, and S. Guoqiang, 2008, Fracture detection by using full azimuth P wave attributes: *Applied Geophysics*, **4**, 238–243.
- Rabe, M. F., 1811, Anlagen am Grottenberg im Garten, *in* Paretzer Skizzenbuch: Stiftung Preussischer Schlösser und Gärten (SPSG), plan collection 16076.
- Radzevicius, S. J., and J. J. Daniels, 2000, Ground penetrating radar polarization and scattering from cylinders: *Journal of Applied Geophysics*, **45**, 111–125.
- Roberts, R. L., and J. J. Daniels, 1996, Analysis of GPR Polarization Phenomena: *Journal of Environmental and Engineering Geophysics*, **1**, 139–157.
- Roest, W., J. Verhoef, and M. Pilkington, 1992, Magnetic interpretation using the 3-D analytic signal: *Geophysics*, **57**, 116–125.
- Russell, B., D. Hampson, and J. Logel, 2009, Applying the Phase Congruency Algorithm to Seismic Data Slices – A Carbonate Case Study: *Frontiers and Innovation - 2009 CSPG CSEG CWLS Convention*, 677–680.
- Sassen, D. S., and M. E. Everett, 2009, 3D polarimetric GPR coherency attributes and full-waveform inversion of transmission data for characterizing fractured rock: *Geophysics*, **74**, J23–J34.
- Scheevel, J. R., and K. Payrazyan, 2001, Principal component analysis applied to 3D Seismic data for reservoir property estimation: *SPE Reservoir Evaluation & Engineering*, **4**, 64–72.
- Schofield, W., and M. Breach, 2007, *Engineering Surveying*, 6 ed.: Butterworth Heinemann.
- Scollar, I., A. Tabbagh, A. Hesse, and I. Herzog, 1990, Archaeological prospecting and remote sensing: Presented at the Topics in Remote Sensing 2.
- Sénéchal, P., H. Perroud, and G. Sénéchal, 2000, Interpretation of reflection attributes in a 3-D GPR survey at Vallée d’Ossau, western Pyrenees, France: *Geophysics*, **65**, 1435–1445.
- Seol, S. J., J.-H. Kim, Y. Song, and S.-H. Chung, 2001, Finding the strike direction of fractures using GPR: *Geophysical Prospecting*, **49**, 300–308.
- Sigurdsson, T., and T. Overgaard, 1998, Application of GPR for 3-D visualization of geological and structural variation in a limestone formation: *Journal of Applied Geophysics*, **40**, 29–36.
- Solheim, F. S., J. Vivekanandan, R. H. Ware, and C. Rocken, 1999, Propagation delays induced in GPS signals by dry air, water vapor, hydrometeors, and other particulates: *Journal of Geophysical Research*, **104**, 9663–9670.
- Sternberg, B. K., and J. W. McGill, 1995, Archaeology studies in southern Arizona using ground penetrating radar: *Journal of Applied Geophysics*, **33**, 209–225.

- Stoica, P., and R. L. Moses, 1997, Introduction to Spectral Analysis: Prentice Hall.
- Streich, R., and J. van der Kruk, 2007, Accurate Imaging of Multicomponent GPR Data Based on Exact Radiation Patterns: IEEE Transactions on Geoscience and Remote Sensing, **45**, 93–103.
- Streich, R., J. van der Kruk, and A. G. Green, 2006, Three dimensional multicomponent georadar imaging of sedimentary structures: Geophysics, **4**, 39–48.
- Tabbagh, A., G. Desvignes, and M. Dabas, 1997, Processing Z gradiometer magnetic data using linear transforms and analytical signal: Archaeol. Prosp., **4**, 1–13.
- Taner, M. T., 1997, Seismic trace attributes and their projected use in prediction of rock properties and seismic facies.
- Taner, M. T., F. Koehler, and R. E. Sheriff, 1979, Complex seismic trace analysis: Geophysics, **44**, 1041–1063.
- Taner, M. T., and R. E. Sheriff, 1977, Application of amplitude, frequency, and other attributes to stratigraphic and hydrocarbon determination: AAPG Memoire, **26**, 301–327.
- Theophanis, S., and J. Queen, 2000, Color display of the localized spectrum: Geophysics, **65**, 1330–1340.
- Thomas, A. M., C. D. F. Rogers, D. N. Chapman, N. Metje, and J. Castle, 2009, Stakeholder needs for ground penetrating radar utility location: Journal of Applied Geophysics, **67**, 345–351.
- Thorseth, J., G. Riley, E. Atalik, and E. Us, 1997, 3-D seismic interpretation using the coherency cube: An example from the South Embra Precaspian Basin, Kazakhstan: The Leading Edge, **16**, 907–909.
- Tronicke, J., J. P. Villamor, and A. G. Green, 2006, Detailed shallow geometry and vertical displacement estimates of the Maleme fault zone, New Zealand, using 2D and 3D georadar: Near Surface Geophysics, **4**, 155–161.
- Tsoflias, G. P., J. P. van Gestel, P. L. Stoffa, D. D. Blankenship, and M. Sen, 2004, Vertical fracture detection by exploiting the polarization properties of ground-penetrating radar signals: Geophysics, **69**, 803–810.
- Tyler, C. W., 2002, Human symmetry perception and its computational analysis: Lawrence Erlbaum Associates Publishers.
- van der Kruk, J., C. P. A. Wapenaar, J. T. Fokkema, and P. M. van Den Berg, 2003, Three-dimensional imaging of multicomponent ground-penetrating radar data: Geophysics, **68**, 1241–1254.
- Von Der Osten–Wohlenberg, H., 2005, Applicatio, in Near-Surface Geophysics: Society of Exploration Geophysicists, 621–626.
- Wagemans, J., 1995, Detection of visual symmetries: Spatial Vision, **9**, 9–32.
- Wagner, G. S., and T. J. Owens, 1996, Signal detection using multi-channel seismic data: Bulletin of the Seismological Society of America, **86**, 221 – 231.
- Wang, Z., and A. C. Bovik, 2009, Mean Squared Error : Love It or Leave It?: IEEE

- Signal Processing Magazine, **26**, 98–117.
- Wang, Z., A. C. Bovik, H. R. Sheikh, and E. P. Simoncelli, 2004, Image quality assessment: from error visibility to structural similarity: IEEE Transactions on Image Processing, **13**, 600–612.
- Watson, D., 1992, Contouring: A Guide to the Analysis and Display of Spatial Data: Pergamon.
- Wijns, C., C. Perez, and P. Kowalczyk, 2005, Theta map: Edge detection in magnetic data: Geophysics, **70**, L39–L43.
- Wilson, J. P., and J. C. Gallant, 2000, Terrain Analysis: Principles and Applications: John Wiley and Sons.
- Wynn, J. C., 1986, Archaeological prospection: An introduction to the Special Issue: Geophysics, **52**, 533–537.
- Yilmaz, O., 2001, Seismic Data Analysis, 2 ed.: Society of Exploration Geophysicists.
- Young, R. A., Z. Deng, K. J. Marfurt, and S. E. Nissen, 1997, 3-D dip filtering and coherency applied to GPR data; a study: The Leading Edge, **16**, 921–928.
- Young, R. A., and N. Lord, 2002, A hybrid laser-tracking GPS location method allowing GPR acquisition in rugged terrain: The Leading Edge, **21**, 486–490.
- Zeng, Z., F. Wu, L. Huang, F. Liu, and J. Sun, 2009, The adaptive chirplet transform and its application in GPR target detection: Applied Geophysics, **6**, 192–200.
- Zhou, B., I. M. Mason, and P. J. Hatherly, 2007, Tuning seismic resolution by heterodyning: Journal of Geophysics and Engineering, **4**, 214–223.

# SUMMARY

---

Based on technological advances made within the past decades, ground-penetrating radar (GPR) has become a well-established, non-destructive subsurface imaging technique. Catalyzed by recent demands for high-resolution, near-surface imaging (e.g., the detection of unexploded ordnances and subsurface utilities, or hydrological investigations), the quality of today's GPR-based, near-surface images has significantly matured. At the same time, the analysis of oil and gas related reflection seismic data sets has experienced significant advances. The requirement for improved reservoir assessment and optimized use of existing fields has, for example, driven the progress of attribute-based processing and interpretation flows. These developments have significantly impacted the quality of current seismic data analyses and interpretations. Attribute-based GPR analyses hold the potential to have a similar profound impact on near-surface related problems considering the possibility to acquire GPR data sets with high spatial density and precision in a cost-efficient manner combined with a broad spectrum of potential applications. However, until recently, attribute analyses were still rarely used in GPR processing and analysis flows.

Considering the sensitivity of attribute analysis with respect to data positioning in general, and multi-trace attributes in particular, trace positioning accuracy is of major importance for the success of attribute-based analysis flows. Therefore, to study the feasibility of GPR-based attribute analyses, I first developed and evaluated a real-time GPR surveying setup based on a modern tracking total station (TTS). The combination of current GPR systems capability of fusing global positioning system (GPS) and geophysical data in real-time, the ability of modern TTS systems to generate a GPS-like positional output and wireless data transmission using radio modems results in a flexible and robust surveying setup. To elaborate the feasibility of this setup, I studied the major limitations of such an approach: system cross-talk and data delays known as latencies. Experimental studies have shown that when a minimal distance of  $\sim 5$  m between the GPR and the TTS system is considered, the signal-to-noise ratio of the acquired GPR data using radio communication equals the one without radio communication. To address the limitations imposed by system latencies, inherent

to all real-time data fusion approaches, I developed a novel correction (calibration) strategy to assess the gross system latency and to correct for it. This resulted in the centimeter trace accuracy required by high-frequency and/or three-dimensional (3D) GPR surveys.

Having introduced this flexible high-precision surveying setup, I successfully demonstrated the application of attribute-based processing to GPR specific problems, which may differ significantly from the geological ones typically addressed by the oil and gas industry using seismic data. In this thesis, I concentrated on archaeological and subsurface utility problems, as they represent typical near-surface geophysical targets. Enhancing 3D archaeological GPR data sets using a dip-steered filtering approach, followed by calculation of coherency and similarity, allowed me to conduct subsurface interpretations far beyond those obtained by classical time-slice analyses. Compared to energy-based approaches, which have been applied to archaeological targets before, these recently developed attributes enable interpretation of features hidden by the complexity of the 3D archaeological data volumes. Furthermore, I could show that the incorporation of additional data sets (magnetic and topographic) and attributes derived from these data sets can further improve the interpretation. In a case study, such an approach revealed the complementary nature of the individual data sets and, for example, allowed conclusions about the source location of magnetic anomalies by concurrently analyzing GPR time/depth slices to be made.

In addition to archaeological targets, subsurface utility detection and characterization is a steadily growing field of application for GPR. Subsurface utilities often cause polarization effects, well-known to be of significant importance to successful feature detection (e.g., buried pipes). To facilitate the interpretation of dual-component GPR data sets (recorded using two perpendicular co-polarized antennae configurations) and to make conclusions about the constituent materials, I developed a novel attribute called depolarization. Incorporation of geometrical and physical feature characteristics into the depolarization attribute allowed me to display the observed polarization phenomena efficiently. Geometrical enhancement makes use of an improved symmetry extraction algorithm based on Laplacian high-boosting, followed by a phase-based symmetry calculation using a two-dimensional (2D) log-Gabor filterbank decomposition of the data volume. To extract the physical information from the dual-component data set, I employed a sliding-window principle component analysis. The combination of the geometrically derived feature angle and the physically derived polarization angle allowed me to enhance the polarization characteristics of subsurface features. In addition, exploiting the actual structural symmetry, often characteristic for man-made utilities, allowed for efficient feature isolation using hard thresholding. Based on a field study conducted at a site characterized by a network of different utility pipes, I demonstrated the applicability of the depolarization attribute, which allowed the distinction between metallic and clay pipes to be made.

Ground-truth information obtained by excavations confirmed this interpretation. In the future, inclusion of cross-polarized antennae configurations into the processing scheme may further improve the quality of the depolarization attribute. Thereby, potential ambiguities introduced by using two co-polarized antennae configurations could be avoided.

In addition to polarization phenomena, the time-dependent frequency evolution of GPR signals might hold further information on the subsurface architecture and/or material properties. High-resolution, sparsity promoting decomposition approaches have recently had a significant impact on the image and signal processing community. In this thesis, I introduced a modified tree-based matching pursuit approach. The lack of properly defined phase shifts for certain widely used wavelets led to a novel approach imposing Hilbert-based phase shifts on the residual waveform to be matched. Based on different synthetic examples, I showed that the modified tree-based pursuit approach clearly outperforms other commonly used time-frequency decomposition approaches with respect to both time and frequency resolutions. Apart from the investigation of tuning effects in GPR data, I also demonstrated the potential of high-resolution sparse decompositions for advanced data processing. Frequency modulation of individual atoms themselves allows to efficiently correct frequency attenuation effects and improve resolution based on shifting the average frequency level.

GPR-based attribute analysis is still in its infancy. Considering the growing widespread realization of 3D GPR studies there will certainly be an increasing demand towards improved subsurface interpretations in the future. Similar to the assessment of quantitative reservoir properties through the combination of 3D seismic attribute volumes with sparse well-log information, parameter estimation in a combined manner represents another step in emphasizing the potential of attribute-driven GPR data analyses.





# ALLGEMEINVERSTÄNDLICHE ZUSAMMENFASSUNG

---

Geophysikalische Erkundungsmethoden haben in den vergangenen Jahrzehnten eine weite Verbreitung bei der zerstörungsfreien beziehungsweise zerstörungsarmen Erkundung des oberflächennahen Untergrundes gefunden. Im Vergleich zur Vielzahl anderer existierender Verfahrenstypen ermöglicht das Georadar (auch als ground-penetrating radar bezeichnet) unter günstigen Standortbedingungen Untersuchungen mit der höchsten räumlichen Auflösung. Georadar zählt zu den elektromagnetischen (EM) Verfahren und beruht als Wellenverfahren auf der Ausbreitung von hochfrequenten EM-Wellen, das heisst deren Reflektion, Refraktion und Transmission im Untergrund. Während zweidimensionale Messstrategien bereits weit verbreitet sind, steigt gegenwärtig das Interesse an hochauflösenden, flächenhaften Messstrategien, die es erlauben, Untergrundstrukturen dreidimensional abzubilden.

Ein dem Georadar prinzipiell ähnliches Verfahren ist die Reflexionsseismik, deren Hauptanwendung in der Lagerstätten erkundung liegt. Im Laufe des letzten Jahrzehnts führte der zunehmende Bedarf an neuen Öl- und Gaslagerstätten sowie die Notwendigkeit zur optimalen Nutzung existierender Reservoirs zu einer verstärkten Anwendung und Entwicklung sogenannter seismischer Attribute. Attribute repräsentieren ein Datenmaß, welches zu einer verbesserten visuellen Darstellung oder Quantifizierung von Dateneigenschaften führt die von Relevanz für die jeweilige Fragestellung sind. Trotz des Erfolgs von Attributanalysen bei reservoirbezogenen Anwendungen und der grundlegenden Ähnlichkeit von reflexionsseismischen und durch Georadar erhobenen Datensätzen haben attributbasierte Ansätze bisher nur eine geringe Verbreitung in der Georadargemeinschaft gefunden. Das Ziel dieser Arbeit ist es, das Potential von Attributanalysen zur verbesserten Interpretation von Georadardaten zu untersuchen. Dabei liegt der Schwerpunkt auf Anwendungen aus der Archäologie und dem Ingenieurwesen.

Der Erfolg von Attributen im Allgemeinen und von solchen mit Berücksichtigung von Nachbarschaftsbeziehungen im Speziellen steht in engem Zusammenhang mit der Genauigkeit, mit welcher die gemessenen Daten räumlich lokalisiert werden

können. Vor der eigentlichen Attributuntersuchung wurden deshalb die Möglichkeiten zur kinematischen Positionierung in Echtzeit beim Georadarverfahren untersucht. Ich konnte zeigen, dass die Kombination von modernen selbstverfolgenden Totalstationen mit Georadarinstrumenten unter Verwendung von leistungsfähigen Funkmodems eine zentimetergenaue Positionierung ermöglicht. Experimentelle Studien haben gezeigt, dass die beiden potentiell limitierenden Faktoren - systeminduzierte Signalstöreffekte und Datenverzögerung (sogenannte Latenzzeiten) - vernachlässigt beziehungsweise korrigiert werden können.

In der Archäologie ist die Untersuchung oberflächennaher Strukturen und deren räumlicher Gestalt wichtig zur Optimierung geplanter Grabungen. Das Georadar hat sich hierbei zu einem der wohl am meisten genutzten zerstörungsfreien geophysikalischen Verfahren entwickelt. Archäologische Georadardatensätze zeichnen sich jedoch oft durch eine hohe Komplexität aus, was mit der wiederholten anthropogenen Nutzung des oberflächennahen Untergrundes in Verbindung gebracht werden kann. In dieser Arbeit konnte gezeigt werden, dass die Verwendung zweier unterschiedlicher Attribute zur Beschreibung der Variabilität zwischen benachbarten Datenspuren eine deutlich verbesserte Interpretation in Bezug auf die Fragestellung ermöglicht. Des Weiteren konnte ich zeigen, dass eine integrative Auswertung von mehreren Datensätzen (methodisch sowie bearbeitungstechnisch) zu einer fundierteren Interpretation führen kann, zum Beispiel bei komplementären Informationen der Datensätze.

Im Ingenieurwesen stellen Beschädigungen oder Zerstörungen von Versorgungsleitungen im Untergrund eine große finanzielle Schadensquelle dar. Polarisations-effekte, das heisst Änderungen der Signalamplitude in Abhängigkeit von Akquisitionssowie physikalischen Parametern stellen ein bekanntes Phänomen dar, welches in der Anwendung bisher jedoch kaum genutzt wird. In dieser Arbeit wurde gezeigt, wie Polarisations-effekte zu einer verbesserten Interpretation verwendet werden können. Die Überführung von geometrischen und physikalischen Attributen in ein neues, so genanntes Depolarisationsattribut hat gezeigt, wie unterschiedliche Leitungstypen extrahiert und anhand ihrer Polarisationscharakteristika klassifiziert werden können.

Weitere wichtige physikalische Charakteristika des Georadarwellenfeldes können mit dem Matching Pursuit-Verfahren untersucht werden. Dieses Verfahren hatte in den letzten Jahren einen großen Einfluss auf moderne Signal- und Bildverarbeitungsansätze. Matching Pursuit wurde in der Geophysik bis jetzt hauptsächlich zur hochauflösenden Zeit-Frequenzanalyse verwendet. Anhand eines modifizierten Tree-based Matching Pursuit Algorithmus habe ich demonstriert, welche weiterführenden Möglichkeiten solche Datenzerlegungen für die Bearbeitung und Interpretation von Georadardaten eröffnen. Insgesamt zeigt diese Arbeit, wie moderne Vermessungstechniken und attributbasierte Analysestrategien genutzt werden können um dreidimensionale Daten effektiv und genau zu akquirieren beziehungsweise die resultierenden Datensätze effizient und verlässlich zu interpretieren.

# CURRICULUM VITAE

---

Urs Böniger was born on the 26th of July 1977 in Baden, Switzerland. He attended public primary and secondary school in Erlenbach, Switzerland, and in 1998 he got his upper secondary school degree from Kantonsschule Küsnacht, Switzerland. After one year of military service in the Swiss army he started studying Geology at the University of Zurich, Switzerland. During his studies he transferred to the Swiss Federal Institute of Technology (ETH) Zurich, where in 2004 he obtained his diploma degree in Earth Sciences with major in Geophysics. He performed his diploma thesis under the supervision of Prof. Dr. Klaus Holliger and Prof. Dr. Jens Tronicke, entitled “Vertical Radar Profiling for Subsurface Imaging”. Afterwards, he spent one year as a postgraduate student at the University of British Columbia, Canada, working on Curvelet based multiple removal in the group of Prof. Dr. Felix Herrmann. In 2006 he started as a Ph.D. student in the group of Applied Geophysics at the University of Potsdam, Germany, under the supervision of Prof. Dr. Jens Tronicke, working on 3D GPR surveying and the potential of attribute-based processing flows. In 2010 he completed his Ph.D. thesis.

This thesis focuses on the potential of improved 3D ground-penetrating radar (GPR) imaging and interpretation through kinematic data acquisition and attribute-based analyses. A surveying approach using a modern self-tracking total station (TTS) is presented. Taking the potential limitations of such a TTS-based surveying setup into account allows for efficient and high-quality data acquisition, which is a prerequisite for attribute-based analyses and interpretations. The benefit of such attribute analyses is evaluated by typical GPR applications from archaeology and engineering. It is shown that established and novel attributes clearly improve the interpretability of a data set and thus our understanding of subsurface structures and properties. This work demonstrates the prospective potential of attributes within the field of GPR towards high-resolution site characterization.

